INTEGRATION OF MEASUREMENTS AND MODELS FOR WIND CHARACTERIZATION

A Dissertation

Presented to the Faculty of the Graduate School

of Cornell University

in Partial Fulfillment of the Requirements for the Degree of

Doctor of Philosophy

by

Paula Doubrawa Moreira

May 2017

INTEGRATION OF MEASUREMENTS AND MODELS FOR WIND CHARACTERIZATION

Paula Doubrawa Moreira, Ph.D.

Cornell University 2017

Atmospheric phenomena across a wide range of scales impact wind power plant aerodynamics. For this reason, problems in wind engineering are best solved using an integration of measurements and models. This approach is used herein to answer a series of distinct research questions. The overarching objective of this work is to improve the quantification of flow parameters of relevance to the wind energy industry in heterogeneous landscapes. These landscapes include complex terrain and land-sea boundaries, turbulent flow within wind farms, and the numerical space referred to as gray zone in atmospheric modeling.

Focusing on the Great Lakes region, a new methodology for offshore wind resource assessment is presented, which is primarily based on in situ and remote sensing observations. It is demonstrated that a combination of distinct data sets yields a robust wind atlas and reduces the error in the final resource.

Seeking to better characterize wind farm aerodynamics, a new approach is proposed to increase the level of detail in low-fidelity wind turbine wake modeling. It consists of a stochastic model which moves away from the commonly used steady, axisymmetric wake modeling framework. When combined with a description for the velocity deficit distribution and used as input to a structural dynamics model, the proposed wake shape model is found to improve predictions of fluctuating loads and power.

Still aiming to characterize wakes, a different study is performed to quantify the level of uncertainty in wind speed retrievals when sampling a large atmospheric volume with a scanning lidar in a wind turbine wake. A high-fidelity simulation is conducted and resampled to match the field measurements, enabling for a comparison between spatially and temporally disjunct points, and what would be seen by the lidar if it could either obtain a snapshot or a true temporal mean of the same volume of air.

Finally, when running full physics atmospheric simulations that are nested down from the meso to the micro scale it is important to consider the treatment of the gray zone in which half the turbulence is naturally resolved by the model while the other half needs to be parameterized. Cutting edge simulation techniques are employed to investigate three different ways of approaching this problem. In one such simulation we further determine how much of the discrepancy between measured and modeled flow parameters can be attributed to wake effects.

BIOGRAPHICAL SKETCH

Paula Doubrawa was born in 31.7654° S, 52.3376° W. She graduated from Universidade Federal de Pelotas with a B.Sc. in Meteorology. After that, she obtained a M.Sc. in Atmosheric Science from University of Alaska Fairbanks, and a M.Sc. in Mechanical Engineering from Cornell University. She joined the Barthelmie Lab in August 2013.

This dissertation is dedicated to Alicia Patterson, Meghan Witherow, Meghnaa Tallapragada, and Stephanie Firehammer.

ACKNOWLEDGEMENTS

I am extremely fortunate to have four incredible role models in my PhD advisory committee. First and foremost, I would like to express my immense gratitude towards Dr. Rebecca J. Barthelmie, the best PhD supervisor I could have asked for. Thank you for inviting me to your lab and teaching me so much while I had no experience in wind energy. Thank you for believing in me, letting me pursue my own research interests, supporting me financially, introducing me to an amazing network of people, and encouraging me to maintain a work-life balance. Secondly, I sincerely thank my other committee members who were happy to advise me and who offered me their unflinching support whenever I needed it. Dr. Sara C. Pryor, thank you for the time and effort you put into revising my papers and into thinking about the research questions I proposed. Your guidance improved the quality and breadth of my work, and helped shape the way I approach problems as a scientist and engineer. Dr. Matt J. Churchfield, thank you for welcoming me at NREL when you didn't even know me, and for being so approachable and willing to advise me in both academic and non-academic issues. Dr. Perrine Pepiot, thank you for bringing another dimension of expertise to my committee which drove me to see wind energy problems through another lens. Thank you for keeping your door open, and for helping me navigate my academic and professional choices.

I would further like acknowledge the importance of those peers who became friends and thereby pillars of my academic achievements. While our scientific passions brought us together initially, your openness to share your personal experiences with me, listen to mine, and spend time together in and outside of the work environment embellished my days. Thank you Alex Ivanov, Hui Wang, Pieter Gebraad, Ryan Snodgrass, Ryan Sullivan, and Tony Martinez. Finally, my

heartfelt gratitude to all other friends I made in Ithaca and who brought beauty in the form of science, poetry, movement, and nature into my life.

The work presented in this dissertation was partly funded by Department of Energy DE-EE0005379, National Science Foundation CBET-1464383, National Renewable Energy Laboratory XFC-5-42084-01, and Cooperative Research and Development Agreement CRD-15-590. I acknowledge the use of computational resources provided by Indiana University High Performance Computing. Some of the data used for this work was provided by the National Renewable Energy Laboratory, the Wind Energy Institute of Canada, and Vortex FCD.

TABLE OF CONTENTS

LIST OF TABLES

LIST OF FIGURES

CHAPTER 1

MOTIVATION AND INTRODUCTION

Global electricity generation has drastically increased in the last decades (Fig. 1.1) mostly due to population growth and the transition towards more technological lifestyles in developing countries which do not form part of the Organization for Economic Cooperation and Development [4]. In order to satisfy these market demands without adding to fossil fuel depletion and pollution problems, governments and developers worldwide have been increasingly investing in renewable energy. In the United States, net annual electricity generation from wind increased by more than 600 % between 2006 and 2015 [5]. As a result of the investment in wind energy research and development, the levelized cost of electricity from wind has become competitive when compared to several other established energy sources (Fig. 1.2, [1]).

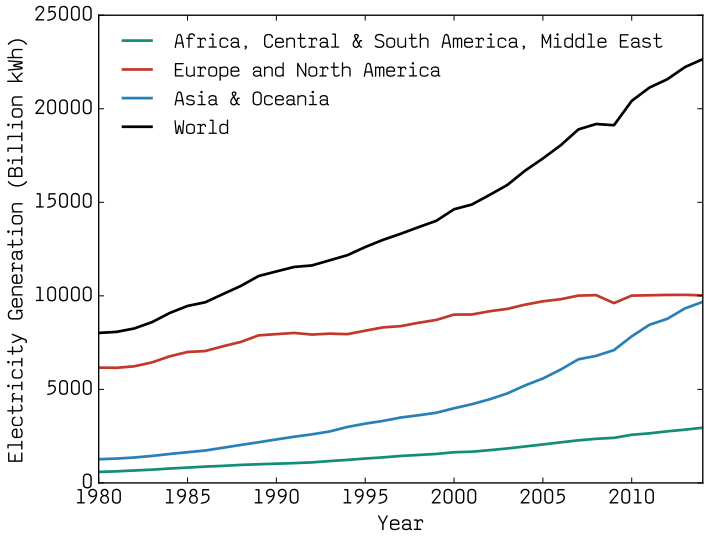

Figure 1.1: Yearly electricity generation [$\times$ 10^9 kWh] for the world (black) and other regions. Data source: International Energy Statistics.

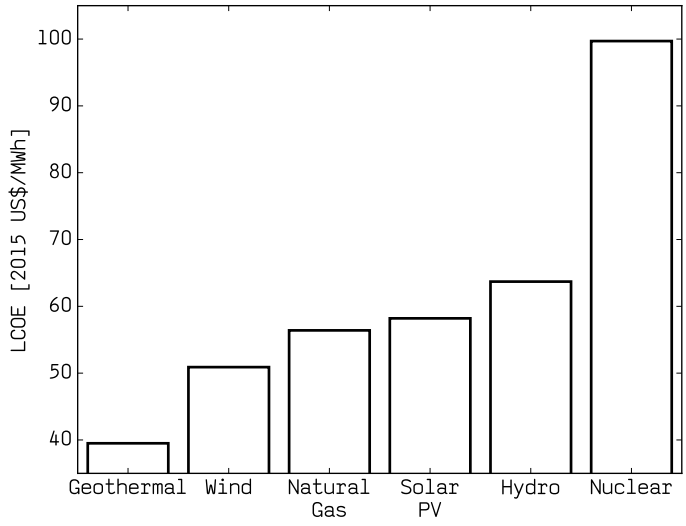

Figure 1.2: Projected levelized electricity costs [2015 US$/MWh] including tax credits for power plants entering service in 2022. Values are weighted average of regional values based on projected capacity additions. For more details, see [1].

The ultimate objective in wind energy research is to deliver safer and more efficient generators and power plants. Efficiency can be improved at any stage in the development of a wind farm: early on, by improving wind turbine (WT) design [6], resource assessment [7] and turbine siting, which includes optimization based on characterization of WT wakes [8]; after commissioning, accurate and timely wind power forecasting can be crucial for effective grid integration and maintenance scheduling [9], and rigorous control strategies are extremely important to maximizing power output and minimizing generator loading [10].

These are all fluid-structure interaction problems, in which the atmospheric boundary layer (ABL) interacts with the planetary surface characteristics (i.e., terrain and roughness), and with the tower and rotor of each WT. As a result, the turbulent flow within and around wind farms is often inhomogeneous, anisotropic, and unsteady [11] and is therefore difficult to measure and model

with sufficient accuracy and detail. For this reason, state-of-the-art wind energy research seeks to combine measurements and models to advance our knowledge across a wide range of disciplines within wind science.

This dissertation combines cutting edge measurement and modeling techniques to develop tools for wind characterization. The following sections provide a brief description of the current state of measurements (Section 1.1) and modeling (Section 1.2) in wind energy, and review some of the recent work done to integrate them (Section 1.3). The objective is to contextualize the work to be presented in the following chapters, which is briefly summarized in Sections 1.4 and 1.5.

1.1 Measurement Techniques

Traditionally, wind speed and direction measurements have been made with cup, propeller, or ultrasonic anemometers and wind vanes [12]. They constitute the conventional instrumentation found on meteorological masts used to assess the wind resource during the planning stage of a wind power plant, and to determine WT power performance following the International Electrotechnical Comission (IEC) standard guidelines [13]. Despite their widespread use, these instruments have some limitations when seeking to characterize the flow within a wind farm. For example, the cup anemometer measurement uncertainty is too large to accurately estimate WT power performance [14], and may additionally lead to power reduction when used to drive the WT control mechanisms [15] while mounted in the back of upstream rotors. Another disadvantage of traditional anemometers relevant to the present work is their inability to sam-

ple large volumes of the atmosphere, which is necessary when focusing on WT wake characterization, or when assessing the wind resource over a large area. As a response to these shortcomings, remote sensing technology for wind energy applications has developed considerably in the last decade. The two types of technology discussed in this work are wind lidar (light detection and ranging instruments) which can measure from the ground or be mounted on the WT nacelle, and satellite-based radar.

Wind lidars employ one of two main techniques to reconstruct the wind field. While some use the intensity of the returned backscattered signal directly, the majority of instruments used for wind research record the frequency shift in the returned signal [12]. The wind velocity along the beam line of sight u_{LOS}

$$u_{LOS} = \frac{\Delta f \lambda}{2} \tag{1.1}$$

is directly proportional to the laser pulse wavelength λ and the Doppler shift Δf, which is a result of the aerosol-induced backscattering in the original laser beam. Throughout this dissertation, the term "lidar" is used to refer to Doppler wind lidar instruments. Due to the extensive validation efforts led primarily by academia, lidars are expected to be incorporated into the IEC standards in the near future. The main advantages of lidar over conventional anemometry are (i) its ability to probe a large volume of air, and to measure at higher vertical levels; (ii) the absence of mast and boom shadow effects [12]; (iii) its mobility; and in some cases, (iv) a flexible scanning geometry that can be easily and quickly modified by the user [16]. However, it is important to keep in mind that lidars also have limitations. For example, the atmospheric conditions and measuring environment affect the level of uncertainty when retrieving horizontal wind speed estimates from these radial velocity u_{LOS} measurements [17, 18].

Both vertically-pointing and scanning lidars can measure from the ground or from the wind turbine nacelle. When ground-based, vertically-pointing lidars can be used to obtain vertical profiles of horizontal wind (Fig. 1.3, left). They serve as an alternative to meteorological masts [19] when high frequency measurements are not necessary, and can thus be used for wind resource assessment as a stand-alone instrument or as a complement to other instrumentation [20]. Scanning lidars (Fig. 1.3, right) also generally measure from the ground [21, 22] and are able to probe large three-dimensional (3-D) volumes of the atmosphere based on user-specified azimuth and elevation angles for each laser beam. The lidar measurements considered in this dissertation (in Chapters 5 and 7) were obtained with ground-based instruments. When nacelle-mounted, measurements can be made upstream for power performance and to drive the torque, pitch, and yaw control mechanisms [23], and downstream when focusing on wakes [24].

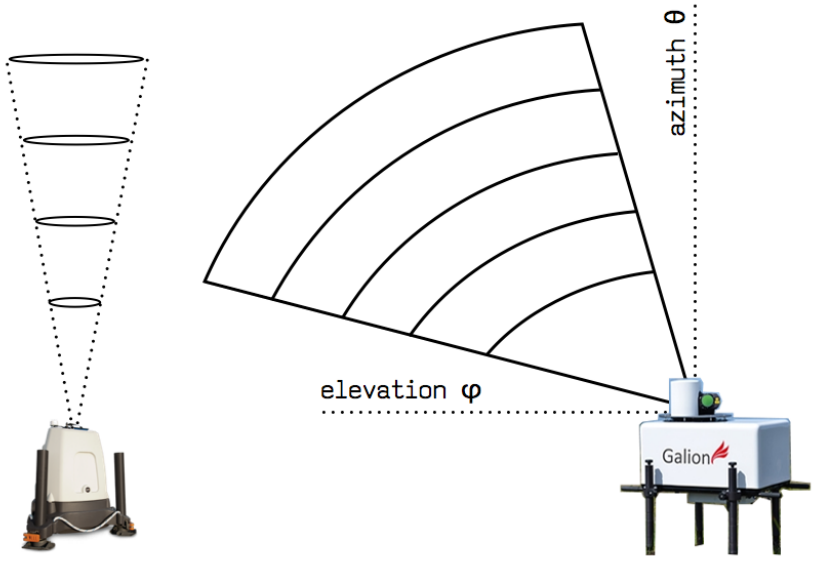

Figure 1.3: Schematic of vertically-pointing (left) and scanning (right) lidar.

Satellite-based remote sensing for wind energy applications is less versatile,

but nonetheless a valuable tool for resource assessment since it provides information over a large area [25, 26]. Recently, its applicability for wind turbine wake research is also being investigated [27]. Satellite-derived wind speeds offshore are retrieved from geophysical model functions which were originally derived empirically and relate the radar backscatter to the equivalent-neutral wind speed u_n [28]

$$u_n = \frac{u_*}{k} \ln\left(\frac{z}{z_0}\right) \tag{1.2}$$

where u_* is the friction velocity, $k = 0.4$ the von Kármán constant, z the height above a water surface (typically 10 m), and z_0 the surface roughness length which offshore can be estimated by

$$z_0 = \alpha_c \frac{u_*^2}{g} \tag{1.3}$$

where α_c is the Charnock [29] constant, and g the acceleration due to gravity. Equivalent neutral winds refer to the magnitude of the wind speed for a neutral atmosphere, and are the only unique solution when seeking to derive a relationship between the momentum flux at the ocean surface and the wind speed at a given height [30]. Means of accounting for stability and of extrapolating to WT hub heights are a subject of ongoing research [31]. The temporal and spatial resolution of the final satellite-derived wind product, as well as its accuracy and detection range depend on the particular instrument being used [26].

This method can only be used offshore because it relies on a relationship between the wind stress and the Earth's surface roughness in the form of capillary waves. Satellite-derived wind estimates over land are instead based on water vapor measurements and cloud movements, and are therefore limited to heights above the ABL [32] and often used as a supplementary tool in weather forecasting [33]. In this dissertation, winds from two different types of satellite-based

radar are used for wind resource assessment offshore as discussed in Chapter 2.

It is important to keep in mind that no instrumentation technique is objectively superior. The instrument choice should be based on the length scales of interest and on the problem at hand. Ideally, more than one instruments should be used allowing for cross-validation [34, 21] and resulting in a more comprehensive data set. Robust measurements can then be integrated with computational fluid dynamics (CFD) techniques to develop [35], drive [36] and validate models [37, 38], to constrain and extend observational data sets [16, 18], and to assist in planning for future measurement campaigns [39].

1.2 Modeling Techniques

In wind plant aerodynamics, it is often necessary to model not only atmospheric conditions but also the structural response of the WT to the environment. There exist a variety of fluid and structural dynamics modeling techniques covering a wide spectrum of resolution, fidelity, and computational cost. Throughout this dissertation, several of these are used depending on the application. This section provides a broad overview of the most commonly used modeling approaches. Specific details can be found in the individual chapters in which each technique is discussed.

Atmospheric phenomena have traditionally been divided into categories regarding their spatial (Δx) and temporal (Δt) scales. A well-established classification [40] distinguishes between macro ($\Delta x >$ 2000 km, $\Delta t >$ week), meso (2000 km $> \Delta x >$ 2 km, week $> \Delta t >$ hour), and micro ($\Delta x <$ 2 km, $\Delta t <$ hour) scales. A schematic of the kinetic energy content in atmospheric phenomena as

a function of these scales is given in Fig. 1.4. Macro scale phenomena include planetary waves and weather systems. In the meso scale, we can list convective systems, and mountain and lake breezes. The micro scale encompasses all smaller phenomena such as tornados, and ABL processes across the inertial subrange of the spectrum and down to the dissipation range. In the macro (meso) scale, the energy transfer typically follows a κ^{-3} ($\kappa^{-5/3}$) rate where κ is the wave number of the flow. While phenomena across all these scales are relevant to wind engineering, CFD for wind focuses primarily on meso and micro scales.

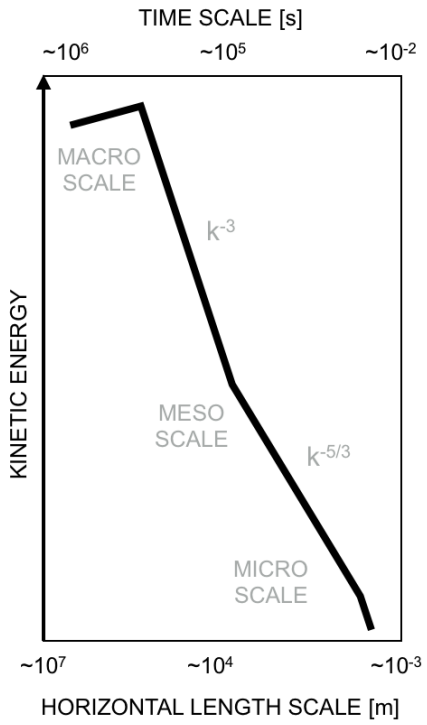

Figure 1.4: Schematic of atmospheric kinetic energy spectrum as a function of horizontal length scale and time scale. Macro, meso, and micro scales are indicated. Energy cascade slopes ($\propto \kappa^{-3}$ and $\propto \kappa^{-5/3}$) are given as proportional to a wave number κ. Schematic is based on [2].

The Weather Research and Forecasting (WRF) model is commonly used for meso scale simulations. It includes a broad range of processes such as radiation,

cloud physics, and surface-atmosphere interactions. Initial (IC) and boundary conditions (BC) to this model are prescribed by global or regional reanalysis data sets, which are obtained from forecast models run in hindcast mode while assimilating a large number of measurements. Because of this thorough data assimilation, reanalyses are often thought of as gridded observational data sets. Besides serving as input to other models, reanalyses are also sometimes used in preliminary wind resource assessment studies wherever direct measurements are not readily available or complete. In this work, they are used in conjunction with a variety of observational data sets to develop an offshore wind atlas (Chapter 2) and as IC/BC to the WRF model (Chapter 6).

In the micro scale CFD is generally divided into three categories, which vary in their level of fidelity. Hereinafter, the term fidelity describes how faithful a simulation is to the physics of interest. The highest fidelity is therefore achieved by solving the Navier Stokes (NS) equations

$$\frac{\partial \vec{u}}{\partial t} + (\vec{u} \cdot \nabla)\,\vec{u} = -\frac{1}{\rho}\nabla P + \nu \nabla^2 \vec{u} + \frac{1}{\rho}\vec{F} \tag{1.4}$$

at a high resolution mesh without the use of a turbulence model, in what is called a direct numerical simulation (DNS). In Eq. (1.4), $\vec{u} = (u, v, w)$ is the three-dimensional wind vector, ρ air density, P air pressure, ν kinematic viscosity ($\nu = \mu/\rho$ where μ is the dynamic viscosity), and $\vec{F}$ represents other forces (e.g., acceleration due to gravity and due to Coriolis). This method is prohibitively expensive for wind energy applications, where a fine and large mesh would be required to resolve all flow structures across an entire wind farm. Additionally to computational shortcomings, the limited availability of high resolution measurements for IC/BC is a significant obstacle to performing DNS for wind engineering.

In large-eddy simulations (LES) only the large, energy-containing eddy sizes (L) are resolved and the mesh resolution determines the filter size applied to the NS equations

$$\frac{\partial \tilde{\vec{u}}}{\partial t} + \left(\tilde{\vec{u}} \cdot \nabla\right) \tilde{\vec{u}} = -\frac{1}{\rho} \nabla \tilde{P} + \nabla \cdot \left[\left(\nu + \nu_{sgs}\right) \nabla \tilde{\vec{u}}\right] + \frac{1}{\rho} \vec{F} \tag{1.5}$$

which now are written in terms of filtered quantities ($\tilde{\vec{u}}$,$\tilde{P}$) and where the total viscosity is divided into the kinematic viscosity ν and the sub-grid scale (SGS) eddy viscosity ν_{sgs} which accounts for the turbulence that the simulation fails to resolve due to the filter size [41]. The eddy sizes L scale with the flow dimensions, and include motions that contain most of the kinetic energy in the flow excluding only the dissipation range of the kinetic energy spectrum [42]. A variety of turbulence models exist to close the system of equations, parameterizing this small-scale turbulence which is often homogeneous and isotropic [43]. LES is recommended when L is in the inertial subrange of the energy spectrum [44], $O(10^2 - 10^1)$ m for the ABL as shown in Fig. 1.4. Despite being more conservative than DNS, LES still requires high performance computing resources and is not yet widely used for long-term, full-physics scenarios. It is therefore primarily used for wind turbine wake studies and controls research, where unsteady small-scale fluid-structure interactions are important [45], and for flow in complex terrain. LES results are present in this dissertation in Chapters 3 to 7. In Chapters 6 and 7 the previously mentioned WRF model is used. In Chapters 3 to 5 the National Renewable Energy Laboratory (NREL) Simulator for Wind Farm Applications (SOWFA, [46]) is employed.

The third category consists of solving the Reynolds-Averaged NS (RANS), a method in which each velocity component u_i is decomposed into time averages $\overline{u}_i$ and fluctuations u_i'. The momentum balance is solved in terms of the mean flow and therefore this technique is primarily used when a statistical rep-

resentation of the flow is sufficient. The only fluctuation term that remains in the momentum equations is the Reynolds stress (e.g., $\overline{u'v'}$ for a two-dimensional system) which is modeled in terms of mean flow quantities to close the system of equations [47]. This method is employed in mid-fidelity models, especially those focused on wind turbine wakes [48, 49]. In this dissertation, a steady RANS model is used for the work presented in Chapter 4. It is based on the thin shear layer approximation to NS

$$\overline{u}\frac{\partial \overline{u}}{\partial x} + \overline{v}\frac{\partial \overline{u}}{\partial r} = \frac{1}{r}\frac{\partial}{\partial r}\left(\nu_T r \frac{\partial \overline{u}}{\partial r}\right) \tag{1.6}$$

solved in downstream (x) and radial (r) coordinates, where the eddy viscosity ν_T is introduced to parameterize the Reynolds stresses $\overline{u'v'}$. The aforementioned WRF model is a RANS solver which includes a variety of atmospheric physical processes in addition to the fluid dynamics component.

In wind engineering, a fourth CFD category can be identified. The term "engineering models" [45] refers to lower-fidelity solutions that provide inexpensive simulations of mean flow features based on analytical expressions which are derived empirically or by simplifying theoretical formulations with a set of assumptions. These models can be used for wind resource assessment and annual energy production calculations, which include mean wake losses. One such example is the traditional Wind Atlas Analysis and Application Program (WAsP) model [50] which is used to obtain the results presented in Chapter 2.

Since WTs are affected by a range of atmospheric phenomena and it is computationally impossible to run DNS incorporating all of these scales, recent research efforts have focused on downscaling coarse simulations towards the micro scale. While downscaling has been a topic of research for decades in the global to meso scale context [51], only in the last decade this technique started

being widely employed in wind engineering. Some downscaling methods are statistical and be can empirically [52] or physically derived [53]. Other methods consist in offline or online coupling between models [45] with or without communication between nested domains. This technique is more computationally demanding and has only recently started to receive attention due to advances in computational power. The meso-micro coupling effort is an ongoing topic of research of broad and current interest, and some of the work presented in this dissertation (Chapter 6) investigates different methods of treating this transition. The challenge lies in modeling the intermediate scale at which some significant fraction of the kinetic energy in a grid cell is resolved for that grid size, while the remaining part still needs to be parameterized. This happens at a spatial scale $O(10^2)$ m, which has become known as the "gray zone" or "terra-incognita" [54]. In the work presented here, we investigate different ways of treating these scales and quantify the impact on simulations of flow parameters of relevance to wind energy.

In addition to CFD, wind turbine and structural dynamics models are often used for research in wind turbine wakes, control systems, and wind turbine design. While some of the work presented in this dissertation (Chapter 4, [55]) uses one such model to estimate loading on the turbine rotor and tower, this dissertation focuses primarily on the fluid dynamics aspect of wind engineering, and these models will not be discussed in detail.

1.3 Integration of Measurements and Models

After recognizing the strengths and limitations of current measurement and modeling techniques, it follows that an integration of both is the ultimate approach to solving complex problems in wind engineering. As briefly mentioned in Section 1.1, measurements can assist in developing, driving, and validating models while models can in turn serve to constrain and extend observational data sets, and to assist in planning measurement campaigns.

In terms of model development, even models that are based almost entirely on a theoretical framework (e.g. mass, momentum and energy conservation in the case of atmospheric simulations) rely on turbulence closure parameterizations that are often derived from full-size measurements or scaled experiments [56]. Simpler, analytical models can be entirely empirical [57] or semi-empirical [58]. Models and measurements also appear together when non-idealized simulations are conducted, and observational data are used as IC/BC to drive atmospheric or structural models (as in Chapters 2, 6 and 7), to nudge the solution during integration [59], or as a post-processor to derive diagnostics from a limited simulation output (as in Chapter 7). Finally, observational data sets are also extensively used for model validation [38, 37].

In the other direction, models can be combined with observations so that the latter can be constrained or expanded. In the first case, uncertainty in observations can be reduced by using a physical rather than a purely mathematical approach to constrain the data. An example would be to use the law of the wall to obtain wind speed values at several heights from a limited set of observations, instead of using a linear interpolation approach. In the second case, a set of

measurements done at one point can be translated to a different location using physical principles as is the approach of the well established engineering model WAsP [3]. Both of these techniques appear in Chapter 2. Finally, a more recent application of model-measurement integration is to perform numerical simulations of future measurement campaigns so that the choice of instruments, their location, and configuration is efficient and well suited to the objectives of the experiment [39, 16].

The overarching objective of this dissertation is to contribute to an improved quantification of flow parameters of relevance to the wind energy industry in heterogeneous landscapes. These landscapes include complex terrain and land-sea boundaries, turbulent flow within wind farms, and the numerical space referred to as gray zone in atmospheric modeling. To achieve this goal, an integration of models and measurements is used in the following chapters, which present a set of fairly independent scientific papers in the fields of wind resource assessment (Chapter 2), wind turbine wake modeling (Chapters 4, 5 and 7) and characterization (Chapter 5), and mesoscale-microscale coupling within atmospheric models (Chapter 6). The published chapters (Chapters 2 to 5) can be accessed with the following references:

Doubrawa P, Barthelmie RJ, Pryor SC, Hasager CB, Badger M, Karagali I. Satellite winds as a tool for offshore wind resource assessment: The Great Lakes Wind Atlas. *Remote Sensing of Environment* Oct 2015; **168**:349– 359, doi:10.1016/j.rse.2015.07.008. URL http://www.sciencedirect.com/science/article/pii/S0034425715300651.

Doubrawa P, Barthelmie RJ, Wang H, Churchfield MJ. A stochastic wind turbine wake model based on new metrics for wake characterization. *Wind Energy* Mar 2017; **20**(3):449–463, doi:10.1002/we.2015. URL http://onlinelibrary.wiley.com/doi/10.1002/we.2015/abstract.

Doubrawa P, Barthelmie RJ, Wang H, Churchfield MJ. Contributions of the Stochastic Shape Wake Model to Predictions of Aerodynamic Loads and Power under Single Wake Conditions. *Journal of Physics: Conference Series* 2016; **753**(8):082006, doi:10.1088/1742-6596/753/8/082006. URL http://stacks.iop.org/1742-6596/753/i=8/a=082006.

Doubrawa P, Barthelmie RJ, Wang H, Pryor SC, Churchfield MJ. Wind Turbine Wake Characterization from Temporally Disjunct 3-D Measurements. *Remote Sensing* Nov 2016; **8**(11):939, doi:10.3390/rs8110939. URL http://www.mdpi.com/2072-4292/8/11/939.

1.4 Research Questions

The main objective of all research efforts in wind engineering is to enable more efficient energy generation. To achieve this goal, it is crucial to reduce uncertainty in energy production estimates. The science of uncertainty quantification consists in assessing the likelihood of an outcome when some aspects of a system are unknown [45]. In the context of this dissertation, uncertainty in wind characterization arises from limitations in measurements, modeling, and data processing techniques as shown by the schematic in Fig. 1.5. It is estimated that in North America approximately 4.0 % of this uncertainty comes from models, and 2.4 % from measurements [60]. These uncertainties affect power output estimates before and after wind farm commissioning via several pathways, e.g. resource assessment, wind farm layout design, and wind farm control strate-

gies. While keeping this objective in mind, the work presented in this dissertation seeks to characterize the level of uncertainty in wind characterization and is based on two general postulates:

(i) The integration of multiple data sets allows for a quantification or a reduction in overall uncertainty levels for wind characterization;

(ii) The integration of measurements and models gives access to insights into dynamical processes that are not achievable using one type of approach.

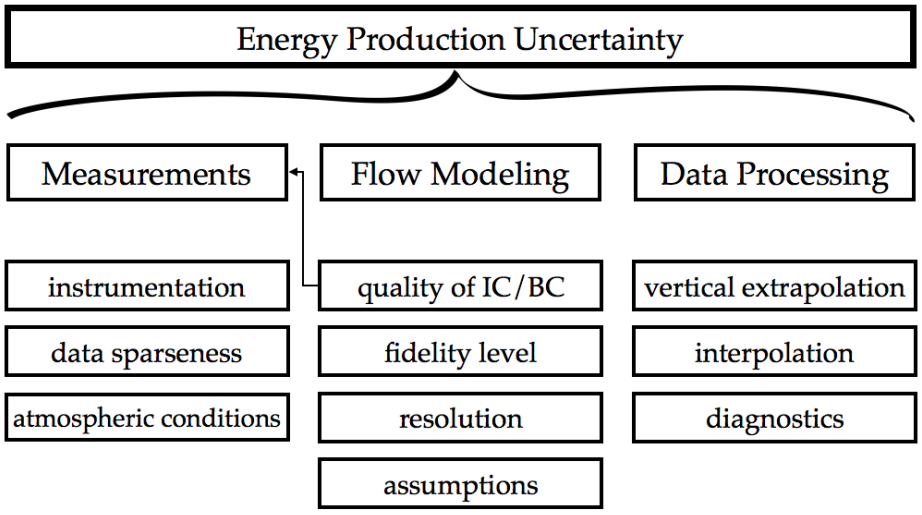

Figure 1.5: Schematic showing main sources of wind energy production uncertainty in the context of this dissertation.

Postulate (i) refers not only to the integration of measurements and models, but also to the integration of observational data sets with different characteristics, and of models with varying levels of fidelity. The term wind characterization is used herein to refer to resource assessment and wind turbine wake analyses. Postulate (ii) acknowledges that measurements and models are inherently limited and that combining them results in data sets that span a wider range of scales and that allow for the study of more complex systems. These

postulates run through the entirety of the work presented hereinafter as briefly summarized in the following paragraphs.

In Chapter 2 several observational data sets and a model data set are used to quantify the uncertainty in wind resource assessment offshore that arises from measurement limitations that are inherent in the instruments, that come from spatial and temporal sparseness of the observations, and that are brought on by adverse atmospheric conditions. The consistency of a model data set leverages the sparseness and inconsistencies in observational data sets, allowing for a reduction in the error of the final wind resource estimates that would not be possible without the model-measurement integration. Moreover, this integration allows for an estimation of the uncertainties derived from specific dynamical processes such as a varying atmospheric stability.

In Chapters 3 and 4 modeling techniques are considered under idealized conditions, and therefore uncertainties are exclusively related to the model fidelity level, resolution, and assumptions (Fig. 1.5). In this context the level of uncertainty in mid- and low-fidelity models can be reduced by producing simulation results that approach those obtained with higher fidelity models. This is achieved by the wake modeling technique proposed and tested in these chapters. The integration of different models (i.e., LES, the proposed stochastic model, and an axisymmetric wake shape model) is crucial to isolating the relative contributions of various dynamical processes (e.g., wake meandering, the role of turbulence in shaping the wake) to the magnitude of loads experienced by a wind turbine subjected to the simulated wakes.

In Chapter 5 the measurement uncertainty due to instrument limitations and to calculation of diagnostic variables from the direct measurements is quanti-

fied by integrating observations and models. The use of a model allows for a comparison between the temporally disjunct measurements obtained with the instrument to the actual mean and instantaneous fields. This comparison would not be possible if considering only the observational data set, from which a true mean and instantaneous estimate cannot be obtained for the large volume being sampled. This model-measurement integration further allows for an estimation of the uncertainty when a single ground-based lidar is used to quantify dynamical processes such as the recovery and trajectory of the wake with downstream distance.

In Chapter 6 model uncertainties due to shortcomings in ABL parameterizations and due to limitations in resolution are estimated. By analyzing the modeled flow fields relative to measurements, the model deficiency in terms of resolving the kinetic energy content and vertical fluxes of heat and momentum at different grid resolutions and with different ABL parameterizations is estimated. Finally, in Chapter 7 model and measurements are combined to estimate how much of the uncertainty in simulated fields can be attributed to the lack of a wind turbine wake representation in the atmospheric model.

1.5 Dissertation Outline

Chapter 2 presents a new methodology for wind resource assessment offshore. It is based on a comprehensive and varied array of in situ and remote sensing observational data sets, a hybrid model-measurement gridded data set (the North American Regional Reanalysis or NARR) and a wind atlas model (WAsP). We elaborate on previously proposed techniques and document meth-

ods that can be used to process each data set individually, addressing their specific shortcomings and capitalizing on their strengths. The main challenge lies in finding methods to overcome the inconsistency in the measurement heights, sampled points, and resolution. The proposed methodology combines distinct data sets to produce a single wind speed estimate for the Great Lakes at a typical wind turbine hub height. The mean spatial bias of the final map when compared to buoy time series is 0.1 m s^{-1} and the RMSE 0.3 m s^{-1}, which represents an uncertainty reduction of 50 % relative to using only Synthetic Aperture Radar (SAR), and of 40 % to using only SAR and QuikSCAT without in situ observations. This methodology is computationally inexpensive, innovative in that the resource assessment is based mainly on observations rather than models, and can be applied to other offshore regions.

Chapter 3 describes the development of a stochastic wind turbine wake model that addresses the gap between low-fidelity inexpensive models that are only valid beyond the near wake, and LES which provide higher-fidelity results at a much higher computational cost. We focus on transverse-vertical planes of flow velocities at discrete distances downstream of the turbine, and propose a method that moves away from steady solutions and assumptions of axial symmetry and seeks to account for the effects of wake-induced turbulence in the simulated fields. Because there are several ways of characterizing wakes, the first part of Chapter 3 explores different approaches to defining global wake characteristics. From these, a model is developed that captures essential features of a LES-generated wake at a small fraction of the cost. The synthetic wake successfully reproduces the mean characteristics of the original LES wake, including its area and stretching patterns, and statistics of the mean azimuthal radius. The mean and standard deviation of the wake width and height are also

reproduced. This is the first step in the model development and further work should generalize the model by considering a wide range of atmospheric stability conditions. The concepts are thoroughly described and the proposed method can be easily incorporated into a pre-existing model framework to improve the level of detail in wind turbine wake simulations.

Chapter 4 determines whether the stochastic wake shape model proposed results in an improvement relative to axisymmetric wake descriptions in terms of loads and power predictions. This is done by comparing aeroelastic simulations initialized with different inflow conditions: an axisymmetric base wake, an unsteady stochastic shape wake, and a LES with rotating actuator-line turbine representation. By turning meandering on or off, the contribution of meandering and wake shape asymmetry to the loads and power can be considered separately. We find that meandering is a large contributor to the load fluctuations and that our proposed model improves the simulations of the quantities considered which are blade root and tower base bending moments, as well as fatigue damage equivalent loads.

The ultimate objective of Chapter 5 is to characterize the wake behind a wind turbine using measurements obtained with a scanning lidar. The measurements are temporally disjunct due to the time that the instrument takes to probe a large volume of air. This leads to some uncertainty in the velocity estimates and wake characterization metrics, which are estimated by placing an imaginary lidar within LES fields and recreating the instrument scanning geometry. Based on LES output, we determine that wind speeds sampled with the synthetic lidar are within 10 % of the actual mean values and that the disjunct nature of the scan does not compromise the spatial variation of mean wind speeds within

the planes. We propose scanning geometry density and coverage indices, which quantify the spatial distribution of the sampled points in the area of interest and can be valuable to the design of lidar measurement campaigns for wake characterization. We find that scanning geometry coverage is important for estimates of the wake center, orientation and length scales, while density is more important when seeking to characterize the velocity deficit distribution. We suggest that future measurement efforts consider these findings and compute expected data density and coverage prior to determining the scanning geometry to be used.

Chapter 6 investigates three different ways of treating the gray zone resolution when running full physics simulations of the atmosphere using WRF. The model domains are initialized with a reanalysis data set and nested down from the meso scale to the micro scale. The finest domain is always run in LES mode (i.e., no ABL parameterization is used) and the gray zone domain is either (i) run in LES mode, (ii) with a typical ABL parameterization, or (iii) with a scale-aware version of this parameterization that limits its effect on the simulated fields under certain conditions. The objectives are to determine the magnitude of the differences across simulations at the gray zone, and how much these differences affect the simulated fields at the innermost domain. We find that over multi-day averages, differences between the two parameterized simulations are negligible but that these differences can be large for short intervals. The parameterized simulations produce slightly better results in terms of horizontal wind speed and vertical wind shear, but the run without a parameterization performs best in terms of spectral energy content and kinematic heat flux.

In Chapter 7 we seek to determine how much of the discrepancy between

measured and modeled flow parameters can be attributed to wake effects. We consider a full physics, non-idealized LES of the atmosphere and divide the simulation into free stream and wake conditions based on wind direction. The wake of a turbine on two downstream locations is considered. The simulation errors are then quantified for each scenario relative to measurements obtained at two turbines and at a meteorological mast equipped with ultrasonic anemometers. As an attempt to reduce the wake-induced wind speed model errors, we test a post-processing wake correction method. This method assumes a constant expansion of the wake with distance downstream, and a sensitivity experiment testing a range of expansion coefficients in the wake model indicates that a value of 0.02 produces the best results for this data set.

Chapter 8 summarizes the research findings, provides an outlook for future work, and concludes this dissertation.

CHAPTER 2

SATELLITE WINDS AS A TOOL FOR OFFSHORE WIND RESOURCE ASSESSMENT: THE GREAT LAKES WIND ATLAS

2.1 Introduction

The Great Lakes extend over 240,000 km^2, accounting for 21% of the total surface freshwater of the planet and 84% of North American resources [61], with maximum depths varying from 19 m in Lake Erie to 406 m in Lake Superior (Fig. 2.1). The population in the area that spans across 8 U.S. states and 2 Canadian provinces is over 33 million [62]. Because of their large expanse, highly available wind resource, and the proximity to large electricity demand centers, the Great Lakes have been considered a potential location for wind energy development for many decades (e.g., [63]). However, over water the wind climate and thus the wind resource is difficult to accurately quantify. The formation of surface ice during winter months [64] precludes retrieval of wind speeds from satellites and necessitates removal of buoys. Additionally, offshore observations are spatially sparse, and availability of satellite imagery for wind retrieval is limited relative to the data requirements necessary to derive a stable estimate of the wind resource [65]. The first attempt to estimate the wind resource in the Great Lakes region was conducted in 1981 [66]. It was based on sparse land-based observations and therefore only estimated the resource over land and along the coast. In 1986, the Canadian government compiled a climatological wind atlas of the region [67]. It was based on data visually recorded on ships, along with meteorological records from the United States and Canada. Later, Environment Canada produced a Canadian Wind Energy Atlas that was based on statistical-

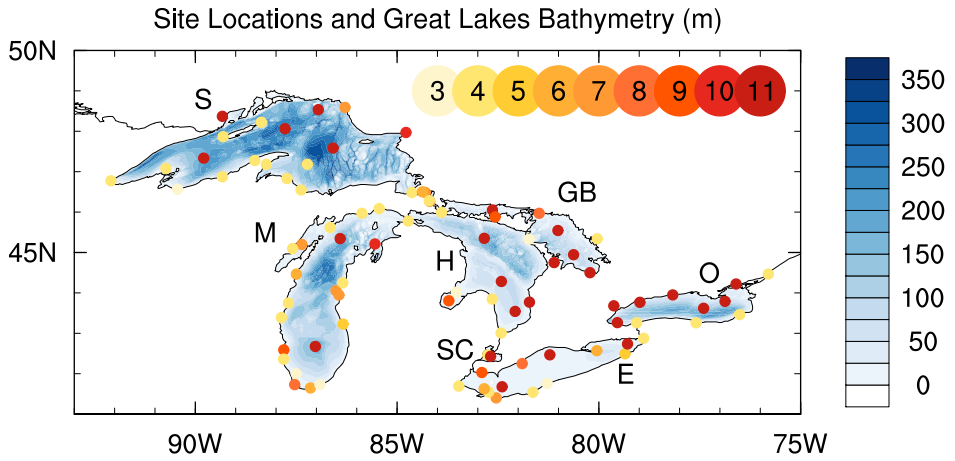

Figure 2.1: Great Lakes bathymetry shown as the shading (m), and location of the coastal stations and buoys used in the analysis. The color coding of the sites indicates the number of years of data considered in this work after quality control. The letters represent the initials of each Lake: Superior (S), Michigan (M), Huron (H), Georgian Bay (GB), Erie (E), Saint Clair (SC) and Ontario (O).

dynamical downscaling of mesoscale model simulation outputs and included most of the Great Lakes [68]. More recently, two additional model-based efforts were undertaken. [69] analyzed the wind resource at 80 m and the wind variability of the Great Lakes based on North American Regional Reanalysis (NARR) data. AWS Truepower and the National Renewable Energy Laboratory [70] produced a wind resource map of the United States that includes the U.S. section of the Great Lakes and was derived from wind flow model simulations and corrected based on observations. However, detailed descriptions of the methodology and data used in that effort are not publicly available.

The objective of this study is to explore the strengths of different observational data sets for winds over the Great Lakes, and to produce an observationally-based wind atlas while providing detailed documentation regarding the methods used. In situ observations from coastal stations and buoys are used, as well as satellite winds from the European Space Agency (ESA) En-

visat Synthetic Aperture Radar (SAR) and from the National Aeronautics and Space Administration (NASA) QuikSCAT scatterometer.

So far, offshore wind resource studies based on SAR and QuikSCAT have mostly focused on the European Seas (e.g., [71, 72, 73, 26]) and very little attention has been given to North American offshore waters, where studies have used short time series and focused on data validation (e.g., [74, 75]) rather than developing methods for accurate wind resource estimation. In this work, we present a method to combine wind measurements from satellite platforms, coastal stations, and buoys that bridges the spatial and temporal limitations inherent in each data set and seeks to characterize the long-term variability of the wind resource. The methods herein presented could be successfully applied to other offshore regions to produce a low-bias wind resource assessment. Section 2.2 describes the data and the methods applied to each data set, and presents the results obtained when using a single data set to obtain a prediction of the Great Lakes mean wind climate. The final results are presented in Section 2.3, followed by a summary and final discussion in Section 2.4.

2.2 Data and Methods

In order to estimate the wind resource of the Great Lakes, this study incorporates both remote sensing and in situ wind observations. This section provides a thorough description of these different measurements, and of the methods applied to each one in order to obtain the Great Lakes observational wind atlas. Although the observations are generally representative of lower heights, this work focuses at the height of 90 m to reflect typical turbine hub-height and to

facilitate comparison with an existing wind resource map for this region [70]. The vertical extrapolation is performed differently for the remote sensing and the in situ data and is described throughout this section. The wind atlas is a large-scale, long-term statistical description of the wind climate, and therefore the complex dynamics of local and diurnal effects such as low-level jets are beyond the scope of the methodology employed. Each available data set has both advantages and disadvantages and different characteristics and error statistics. For example, the in situ measurements are disjunct time series of temporal averages taken at a point, while the satellite-based remote sensing values are pseudo instantaneous, spatial averages with varying disjunct sampling frequency. The method of data integration employed herein seeks to capitalize on the strengths of each data set, and to address their respective weaknesses by applying data set-specific pre-processing and processing steps, which are summarized by the schematic in Fig. 2.2.

2.2.1 In Situ

The in situ measurements used in this study come from 70 meteorological stations at coastal sites and from 20 buoys (Fig. 2.1) and are obtained from 2002 to 2012. The data for U.S. sites were obtained from the National Data Buoy Center (`http://www.ndbc.noaa.gov/`) and depending on the location they were maintained by the Coastal-Marine Automated Network (C-MAN), the National Oceanic and Atmospheric Administration (NOAA) National Ocean Service (NOS), the National Weather Service (NWS), or the Great Lakes Environmental Research Laboratory (GLERL). The data for Canadian sites were obtained from the Ontario Climate Center (`http://climate.weather.gc.ca/`). All

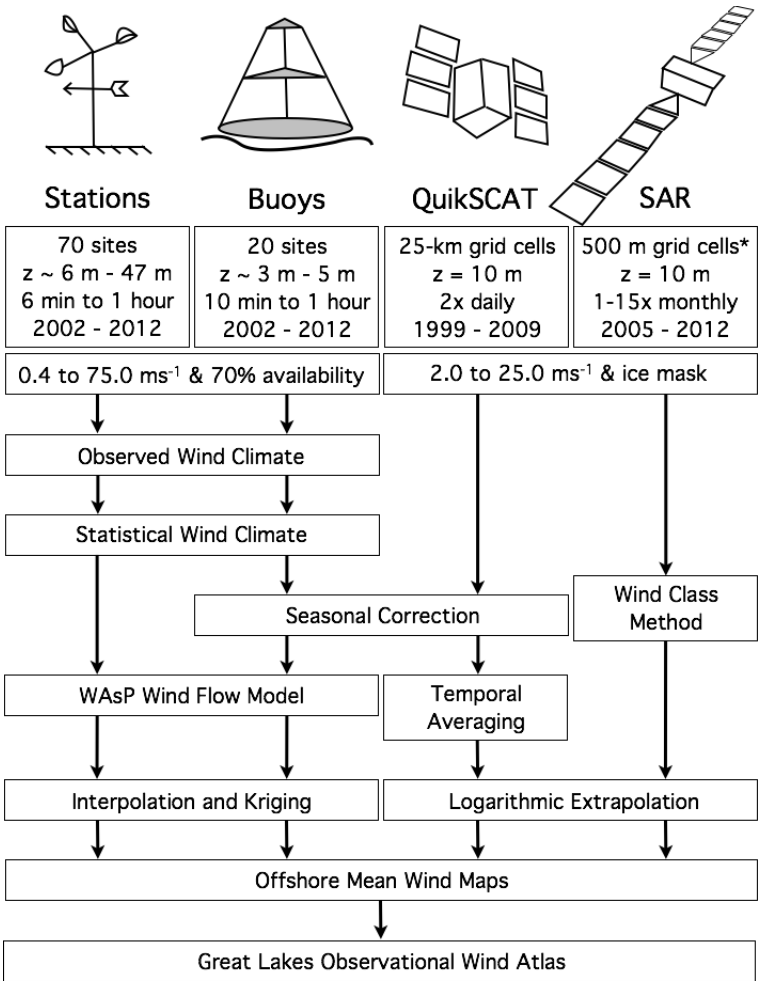

Figure 2.2: Schematic of the different data sources and the methodology applied to each one to generate wind speed maps and finally an observational wind atlas. For each data stream, the first line describes the number of sites (for coastal stations and buoys) or resolution (for satellites), the second line shows the temporal averaging period of the measurements (for coastal stations and buoys) or overpass frequency (for satellites). *For SAR, resolution of the derived wind maps is 500 m while original resolution of Envisat SAR Wide Swath Mode is 150 m. The following lines represent the period of data availability, the data filtering criteria, and the processing steps.

sites are equipped with propeller anemometers. Data are reported every 6 minutes to 1 hour, with sporadic periods of higher frequency. Because of the high frequency and long record, we assume that diurnal, seasonal, and interannual variability are captured in the mean wind climates derived from these data. The coastal stations have long-term records but represent coastal conditions. The buoys capture offshore conditions but are less numerous and unavailable during the cold season, when they are removed from the Lakes due to ice formation. Both provide measurements at relatively low heights, with anemometer heights ranging from 6.4 to 46.9 m for the coastal stations and from 3.2 to 5.0 m for the buoys.

Quality Control

Quality control was performed on data from coastal sites and buoys to reduce uncertainties and to prevent seasonal biases from affecting the wind atlas calculations. Inaccurate and unrealistic values were identified using the following criteria (Eqs. (2.1a) to (2.1d)) and removed from the time series.

$$\left|\vec{u}\right| < 0.4\ ms^{-1} \tag{2.1a}$$

$$\left|\vec{u}\right| > 75\ ms^{-1} \tag{2.1b}$$

$$\left|\vec{u_i}\right| > \left|\vec{u}_{i-1}\right| * 1.5 \text{ and } \left|\vec{u_i}\right| > \left|\vec{u}_{i+1}\right| * 1.5 \text{ if } \left|\vec{u_i}\right| > 15\ ms^{-1} \tag{2.1c}$$

$$0^\circ > \theta > 360^\circ \tag{2.1d}$$

The anemometer response can be slow near its cut-in value since it needs to overcome mechanical friction and inertia to start spinning. As a consequence, the observations in the first bin of the observational histogram ($0 - 1\ ms^{-1}$) in-

clude erroneous values as well as wind speeds below 1 ms^{-1}. To prevent this excessive number of calm recordings from skewing the Weibull distribution fit, Eq. (2.1a) is applied to remove a portion of these erroneous values, while still allowing a sufficient number of low but legitimate wind speed values to remain for the proper fitting of the distribution. Eq. (2.1b) removes possibly erroneous high values [76] that are sometimes present in the original data due to formatting or recording issues. Instead of defining the maximum allowed variability as a fixed value, Eq. (2.1c) was used to remove any isolated high entries by filtering out values that are more than 150% of both the previous and the following entries. This criterion was applied only to very high wind speeds ($u > 15\ ms^{-1}$ at anemometer height) and filtered out a negligible portion of the data ($\sim 0.002\%$).

To avoid seasonal biases, each coastal site was conditioned to keep only sampled years of data for which each month had an availability $\geq 70\%$ (e.g. for hourly observations in January the total possible is 24*31 so a minimum of 521 entries was required). Moreover, only sites with at least three years of complete data were kept in the analysis, in order to minimize the impact of interannual variability biases on the wind climate. For the 11-year period considered, the annual mean wind speeds averaged across sites were $\sim 5.0\ ms^{-1}$ for buoys and $\sim 4.8\ ms^{-1}$ for coastal stations, with an interannual variability of $\pm 0.6\ ms^{-1}$ and $\pm 0.5\ ms^{-1}$ respectively. The number of years of data used for each site after quality control varies from 3 to 11 years (Fig. 2.1). Note that Fig. 2.1 does not represent the number of years rejected during quality control, since very few sites were operational during the entire 11-year period. Each year has measurements from at least 3 sites (coastal or buoy) in each lake (Fig. 2.3). The lake with fewest sites is Lake Michigan from 2002 to 2005. In contrast, the most robust representation is for Lake Huron in 2011 and 2012, where 21 sites were available with

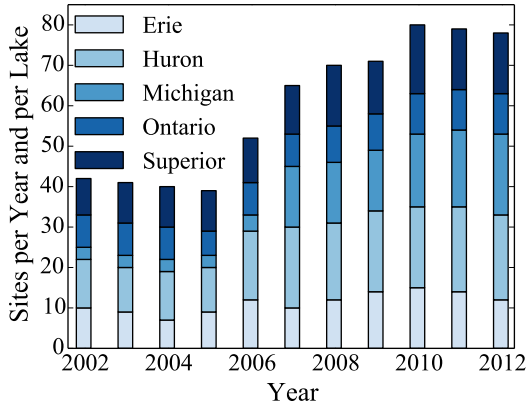

Figure 2.3: Number of coastal and buoy sites with complete data records, for each year from 2002 to 2012 for each of the Great Lakes.

complete data.

Wind Climates

To reconcile measurements taken at different heights (anemometer heights for the in situ measurements vary from 3.2 m to 46.9 m) and in different local wind regimes and thus develop an integrated wind resource estimate at a standard height (here of 90 m), the in situ time series of data from each site were used to develop generalizable wind climates (Fig. 2.2) using the Wind Atlas Analysis and Application Program (WAsP) [50]. WAsP is the most widely used model for wind resource assessment. It uses roughness, topography and internal boundary layer models, and the geostrophic drag law to extrapolate the observations from a mast (at anemometer height) to other points in space (often to hub height). The mean wind climates are statistical summaries of wind conditions at a given site and are produced as follows: the time series of wind speeds and directions are used to generate 30° wind direction sector-specific histograms of the wind speeds (i.e., the observed wind climate in Fig. 2.2) from which the

Weibull scale and shape parameters (A and k, respectively) are derived. Then these wind climates in each sector are generalized by removing the local effects of orography and roughness to obtain a value for the geostrophic wind that is independent of the surface conditions and assumed to be homogeneous within a given area [3]. This value can then be used to obtain the wind climate over an area of approximately a 50 km radius from the station, by reincorporating the orography and roughness characteristics of the target points. In this application the orography was described using NASA's Shuttle Radar Topography Mission data at a resolution of 30 arc-seconds (approximately 0.9 km in latitude and 0.6 to 0.7 km in longitude for the Great Lakes geographical location), the over-water roughness length was assumed to be 0.0002 m, and the roughness length over land was assumed to be 0.1 m. Obstacles were not taken into account since the focus of this work is offshore resource assessment. The standard WAsP parameters were used, which include a slightly unstable atmosphere offshore, with a heat flux of 15 Wm^{-2}. Using these assumptions, generalizable wind climates (i.e., the statistical wind climate in Fig. 2.2) were derived for heights (z) of 10, 25, 50, 90 and 150 m and roughness lengths (z_0) of 0.0002, 0.03, 0.1, and 0.4 m for all buoys and coastal stations following the well established wind atlas methodology [3].

Seasonal Correction

Because the Great Lakes system is a high latitude freshwater system, it is subject to extensive ice cover [77, 64]. This poses a challenge both for prospective wind deployment (though use of ice-cones can greatly reduce foundation loading from ice floes [78]) and for accurate quantification of the wind resource, be-

cause during the ice formation months the buoys are removed from the Lakes. During the 11-year period considered, the average length of cold-season data gaps varied from 3.1 to 5.5 months across the buoy locations, with a spatial average of 4.1 months of missing data per cold season per site. Thus a correction was applied to each buoy generalized wind climate to correct for the absence of cold-season data. A reference data set was used in this procedure, namely the National Center for Environmental Prediction (NCEP) North American Regional Reanalysis (NARR) [79]. These data are for a nominal height of 10 m, and are available at 3-hourly intervals at a spatial resolution of 32 km. The method applied to correct for the missing buoy observations is based on the measure-correlate-predict method of ratios [80]. For each standard roughness and height, the mean and the mean cubed of the Weibull distribution were calculated according to Eq. (2.2) [3], where m^n represents the first moment (i.e., the mean) to the n^{th} power $[ms^{-1}]^n$, A the scale parameter $[ms^{-1}]$ and k the shape parameter of the Weibull distribution, and Γ the gamma function.

$$m^n = A^n \Gamma\left(1 + \frac{n}{k}\right) \tag{2.2}$$

Concurrently, the mean and mean cubed were calculated for the reference time series considering two scenarios: a complete data record that includes the cold season, and a shorter record that includes only the time stamps that coincide with the buoy availability. For those coinciding time stamps, a ratio of the moments was obtained. This ratio and the moments for the complete-record reference series were then used to obtain corrected buoy moments, as given by Eq. (2.3) where the subscript o represents the original buoy series and r the reference series.

$$m^n_{o,corrected} = \frac{m^n_{o,short}}{m^n_{r,short}} m^n_{r,complete} \tag{2.3}$$

Once the moments have been corrected, Eq. (2.2) can be used again to recalculate the Weibull parameters A and k, which now describe the corrected generalized wind climate.

Validation of Seasonal Correction

The validity of this seasonal correction was tested on data from the coastal stations, for which complete time series are available. Thus, the method applied in Section 2.2.1 is evaluated here by deriving time series for the coastal stations that mimic the fractured buoy data sets and by comparing them against the complete time series. The all-sector percent errors between the generalizable wind climate derived from the original complete time series and the "corrected" complete series are shown in Fig. 2.4. These errors were calculated for the height of 90 m and four roughness classes for the mean and for wind power density P $[Wm^{-2}]$, which is given by Eq. (2.4), where the air density ρ was taken to be 1.225 kgm^{-3}. Errors were calculated as $(x_{true} - x_{estimate})/x_{true}$.

$$P = \frac{1}{2}\rho A^3 \Gamma\left(1 + \frac{3}{k}\right) \tag{2.4}$$

The approach is generally robust. For the first moment (i.e., the mean), all errors were within 10%. When averaged across roughness classes, the mean error was -0.8 %, the median -1.3%, and the standard deviation 4.1%. For the power density, the cube relation of the scale factor (A^3 in Eq. (2.4)) amplifies uncertainties and the errors are higher. They were within 25%, with a roughness-averaged mean of -1.8%, a median of -3.3%, and a standard deviation of -10.6%. As indicated, the mean error is generally negative which indicates that the moment-ratio correction method slightly under-corrects for the sampling bias introduced by the removal of buoys due to the presence of ice on the Lakes.

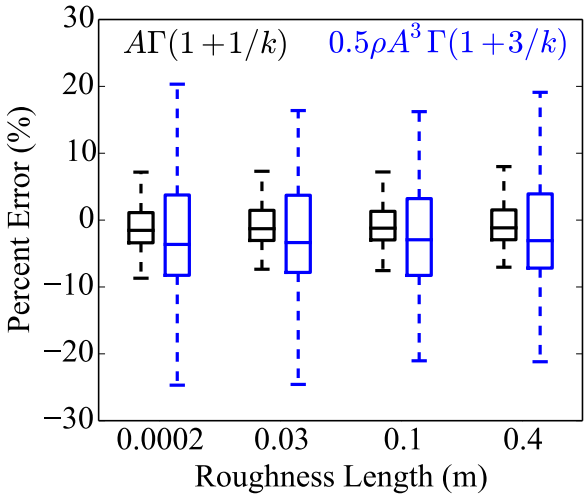

Figure 2.4: Percent errors for the first moment of the Weibull distribution and for power density at 90 m when using NARR as a reference series and the method of ratios to correct for the seasonal bias artificially introduced in the data from coastal stations. The box plots are spatial averages across the coastal stations. For each coastal station, the number of years of data considered differs and is given in Fig. 2.1.

Seasonal Correction Results

The differences between the predicted wind resource at 90 m before and after the buoy correction are shown in Table 2.1 for wind speed u and wind power density P as given by Eq. (2.4). They were highest for Lake Superior, where the predicted P was $\sim$ 34% higher after the correction for missing data due to ice cover, and lowest for Lake Erie, where it was $\sim$ 14% higher. The predicted resource at 90 m offshore was also calculated using the artificially incomplete May-Oct coastal time series and their complete Jan-Dec counterparts, for the 70 coastal stations. The results are shown in bold in Table 2.1. Consistent with prior modeling analysis that has indicated higher wind speeds during the cold season and the importance of ice cover to determining wind regimes over lakes [69],

application of the correction increases the wind resource and exhibits variation across the Lakes. In terms of power density, the highest difference for the coastal stations is seen for Lake Erie ($\Delta P \sim 57\%$) and the lowest for Lake Superior ($\Delta P \sim 28\%$).

Table 2.1: Difference ($x_{after} - x_{before}$) in wind resource at 90 m as predicted by WAsP (wind speed u and power density P) before and after the seasonal correction was applied to data from the buoys and to the artificially incomplete coastal sites (boldface), calculated at each site and spatially averaged over each Lake (number of sites per Lake is given).

	Δu $[ms^{-1}]$	Δu [%]	ΔP $[Wm^{-2}]$	ΔP [%]	Number of Sites
Superior	0.8, **0.6**	11.8, **10.2**	125, **74**	33.8, **28.1**	4, **14**
Michigan	0.7, **0.7**	10.2, **12.2**	116, **105**	26.1, **37.9**	2, **19**
Huron	0.4, **0.5**	6.5, **9.5**	58, **66**	15.3, **31.2**	6, **18**
Erie	0.3, **0.9**	5.3, **15.7**	44, **126**	13.8, **57.0**	4, **12**
Ontario	0.7, **0.8**	11.2, **13.5**	90, **107**	27.4, **49.6**	4, **7**

Predicted Wind Speeds

Once the correction was applied, the generalized wind climates for each buoy and coastal station were used in WAsP to produce 90 wind resource maps centered at each of the 90 sites. For the coastal stations, the resource maps extended over a radius of 25 km. Because the buoys are offshore where winds are likely to be more homogeneous, resource maps for the buoys extended out to 50 km from the center. The resource maps were discretized with 1 km resolution. The 90 individual maps were then merged using bilinear interpolation as the resampling method, considering a weighted average of the four closest pixel centers. Once combined, the map was gridded using a kriging method [81] to generate a homogenized wind resource at 90 m (Fig. 2.5). The spatial heterogeneity of the resource map (localized maxima and minima) are the result of the data

sparseness and the interpolation, and re-emphasizes the value of integration of over-lake remote sensing data. Since each site produced an individual resource map (25 km x 25 km for coastal stations and 50 km x 50 km for buoys), the proximity of sites seen at some locations led to the overlapping of individual resource maps. Upon interpolation and gridding, the overlapping areas introduce some uncertainty in the wind resource at the buoy locations, as is seen by the mean bias values in Fig. 2.5 for Lake Ontario and Lake Saint Clair. Hereafter, "bias" refers to a measure of the uncertainty in the method determined by the difference in an observed and interpolated value. The bias is given by Eq. (2.5), where u_{90_M} is the mean wind speed at 90 m as predicted by the method being presented, and u_{90_W} is the mean wind speed at 90 m as predicted by WAsP from ice season-corrected buoy data. Root-mean-square errors (RMSE) are calculated according to Eq. (2.6) where N_{buoys} is the number of buoy sites being used in the error calculation.

$$bias = u_{90_M} - u_{90_W} \tag{2.5}$$

$$RMSE = \sqrt{\frac{\sum_{buoys} \left(u_{90_M} - u_{90_W}\right)^2}{N_{buoys}}} \tag{2.6}$$

The bias values ranged from -0.4 to 0.8 ms^{-1} (Fig. 2.5), with a mean bias of $\sim$ 0.0 ms^{-1} when averaged over all buoy locations, and a RMSE of $\sim$ 0.2 ms^{-1}.

2.2.2 SAR

Because of its high resolution, SAR provides detailed information on the spatial variability of the wind offshore and near the coast. For that reason, it has been considered as a valuable tool for offshore wind resource assessment for over a decade (e.g. [65, 82]). Several methods have been proposed to obtain accurate

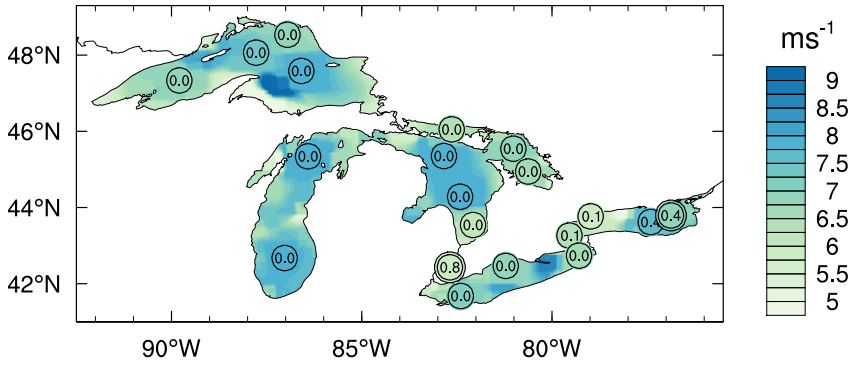

Figure 2.5: Mean wind speed at 90 m as obtained from time series of 90 coastal stations and buoys from 2002 to 2012 and after correcting for the lack of ice-season data in the buoy records, processing with WAsP, merging and kriging. Overlaid circles illustrate mean biases in the final resource map where single (double) line represents an under (over) estimation of the resource (in ms^{-1}), in comparison with the wind speed predicted by WAsP at the buoy locations after ice correction.

offshore wind resource estimates from SAR scenes that include information on the spatial and temporal variability of the local wind climate. [83] found that a minimum of 60 serially independent satellite scenes are necessary to obtain a statistical representation of the mean wind speed with an uncertainty below ± 10% for a confidence level of 90%. [71] showed that selecting SAR scenes according to wind classes that are representative of the local wind climate resulted in an improvement over randomly sampling the available scenes. Despite being temporally limited and sometimes spatially sparse, SAR data provide excellent spatial coverage and relatively high accuracy in some regions [65]. Because of their high resolution they are also available close to the coast [84], and add detail to the representation of spatial variability offshore [26]. Synthetic Aperture Radar (SAR) data used herein were obtained from the Envisat mission by the European Spage Agency (ESA). Level 1 data products acquired in Wide Swath Mode (WSM) with the swath width of 400 km and a spatial resolution of 150 m are used. These are available for a long period (2002 to 2012) and at a low

frequency (one to fifteen times per month in this region). Wind speed maps are retrieved from the SAR scenes using a Geophysical Model Function (GMF), which describes the empirical relationship between the wind speed, the radar backscatter from the water surface, and the radar viewing geometry (see [85] for an overview of SAR wind retrieval). Here the GMF called CMOD5.n [86] is applied with input wind directions from the U.S. Navy's Operational Global Atmospheric Prediction System Model (NOGAPS).

Quality Control

During the period from 2002-2012, a total of 764 SAR scenes are available from the ESA archive (`https://earth.esa.int/web/guest/missions/esa-operational-eo-missions/ers/instruments/sar`) for the Great Lakes region (Fig. 2.6). The presence of ice can lead the algorithm to return unrealistic high wind speed values. Therefore, areas covered by sea ice are masked out using the IMS Daily Northern Hemisphere Snow and Ice Analysis at 4 km resolution [87]. The output maps give the 10-m Equivalent Neutral Wind (ENW) in 500-m grid cells. Cells of the original SAR scenes were averaged to this size in order to reduce effects of random noise, long-period waves, and hard targets in the SAR data. Values smaller than 2 ms^{-1} or greater than 25 ms^{-1} at 10 m height were removed because they were expected to have a high level of uncertainty. No attempts were made to mask out rain effects as the rain sensitivity of C-band SAR is very limited. Inaccuracies due to these limitations in sensor recording ranges are expected to be smoothed out by the integration with the other data sets (Section 2.3).

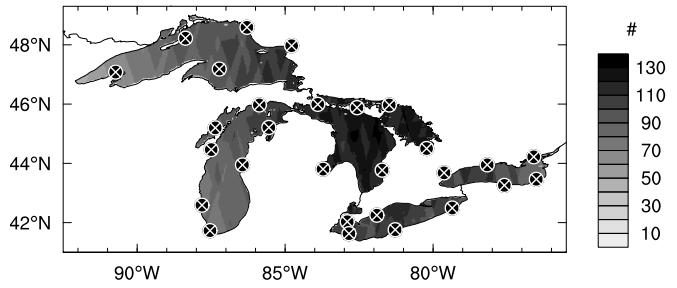

Figure 2.6: Spatial distribution of the availability of SAR wind speed estimates for each over water pixel (shading) from 2002 to 2012 and the location of the measurement sites used to generate the weights for the wind class method (markers).

Wind Class Method

Because of the temporal sparseness of the SAR observations, a statistical analysis of the wind resource, as was conducted for the in situ data, is not viable. Thus an alternative based on wind classes [71] is used here. This method integrates all available satellite scenes by assigning each pixel of each swath to a specific pre-defined wind class based on its wind speed and direction and then by combining the classes using a weighted average. The classes are representative of the regional wind climate (i.e., representative of a spatial distribution of wind speed for a given wind speed and direction) and the weights describe the frequency of occurrence for that particular wind class. Classes and their respective weights are obtained from a separate data set which includes information on diurnal, seasonal and interannual variability of the wind resource. In this study, the classes and weights were obtained separately for each Lake using observational data from a number of coastal stations. The choice of sites (Fig. 2.6) was based on their length of record and their position, in order to ensure a representation of the wind climate at several geographical locations around each of the Lakes. For each Lake, the data were divided into 12 directional sectors

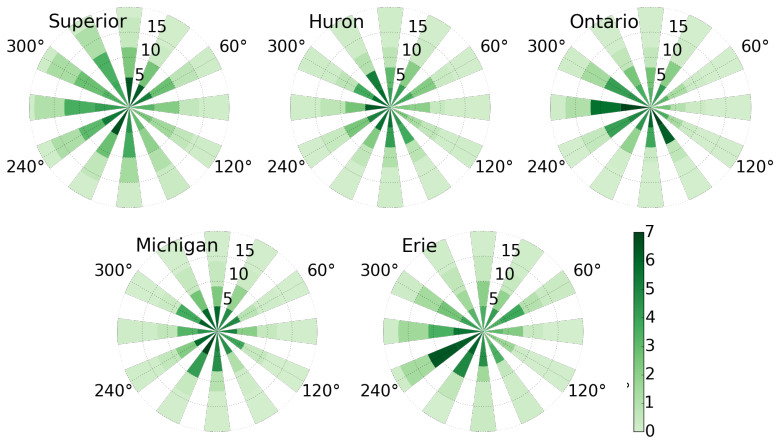

Figure 2.7: Wind class roses for the Great Lakes. Horizon is divided into 12 30° sectors, which are then divided into 4 wind speed classes given by the bar radii. Radii contours are at 5, 10, 15, and 20 ms^{-1}. Colors represent the weight (%) of each class.

and within each sector, into 4 wind speed classes (Fig. 2.7). The frequency of occurrence of measurements within each of the 48 classes was obtained and later used as weights to combine the several SAR scenes. Each pixel in each SAR scene was assigned to one of the classes according to its wind speed and direction. The arithmetic mean was used to obtain the pixel wind speed if more than one pixel was assigned to the same class and the same geographical location. The wind class method combines all available wind speed data from the SAR images into 48 maps (one for each class) for each Lake. This methodology seeks to overcome the spatiotemporal sparseness of the SAR scenes. Two examples of classes are shown for Lake Erie in Fig. 2.8, where (a) represents $\theta = 0° \pm 15°$ and $5 \leq \left|\vec{u}\right| < 10\ ms^{-1}$ with a weight of 2.06% (since 2.06% of all data for Lake Erie fall into this category), and (b) represents $\theta = 180° \pm 15°$ and $4 \leq \left|\vec{u}\right| < 7\ ms^{-1}$ with a weight of 4.73%. This means that the weights for the other 46 classes for the same lake add up to 93.21%. The white patches in Fig. 2.8 indicate that none of the 764 SAR scenes had observations within that class for that location.

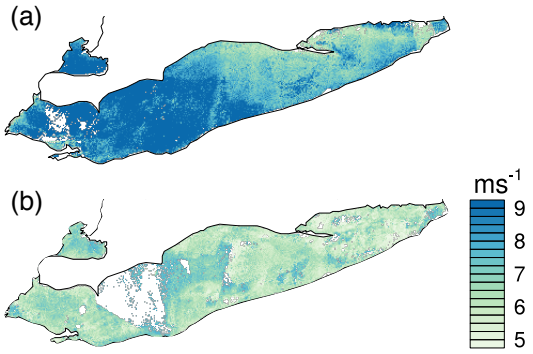

Figure 2.8: Example of two wind classes for Lake Erie: (a) $\theta = 0° \pm 15°$, $5 \leq \left|\vec{u}\right| < 10\ ms^{-1}$, weight=2.06% and (b) $175° \leq \theta < 195°$, $4 \leq \left|\vec{u}\right| < 7\ ms^{-1}$, weight=4.73%. Shading represents equivalent neutral wind speed at 10 m (ms^{-1}).

Predicted Wind Speed

A weighted average of the 48 individual maps (one for each wind class) yields a single resource map from the SAR satellite winds that accounts for the lack of seasonal and interannual representativeness inherent in the temporally sparse data. To allow integration with the in situ observations, the final winds were extrapolated from 10 m to the height of 90 m using the neutral logarithmic profile given by Eq. (2.7), where $z_0 = 0.0002$ m (Fig. 2.9).

$$u_{90} = u_{10}\left[\frac{ln(90/z_0)}{ln(10/z_0)}\right] \tag{2.7}$$

This vertical extrapolation was applied to the remote sensing ENW. [26] found the mean difference between SAR ENW and mast stability-dependent winds (SDW) to be $\sim 0.07\ ms^{-1}$ at 10 m height for offshore Denmark, with the neutral winds being higher. This difference can be used to approximate the uncertainty due to vertical extrapolation assuming a near-neutral stability. In order to obtain such an estimate for the Great Lakes, we used the air temperature, water temperature, and wind speed data from the 20 buoys to estimate the friction velocity u_* and roughness length z_0 using the bulk flux algorithm of [88]. These values

were then used to obtain time series of neutral winds for the buoys. Averaging over the entire time record and in space, we found the ENW to be higher than the SDW by $\sim 0.16\ ms^{-1}$, with differences ranging from $\sim 0.01\ ms^{-1}$ to $\sim 0.3\ ms^{-1}$ as a function of the measured SDW. This value indicates an uncertainty of on the order of $10^{-1}\ ms^{-1}$ in the mean wind map obtained from SAR.

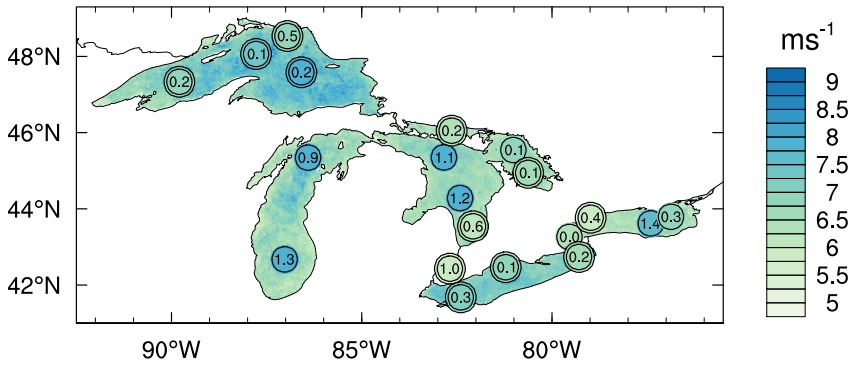

Figure 2.9: Mean wind speed at 90 m as obtained from SAR winds from 2002 to 2012 using the wind class method. Overlaid circles illustrate mean biases in the final resource map where single (double) line represents an under (over) estimation of the resource (in ms^{-1}), in comparison with the wind speed predicted by WAsP at the buoy locations after ice correction.

In contrast to the map from in situ observations, the SAR mean wind map is spatially smooth due to the ample spatial coverage of the SAR scenes. Point biases were calculated by using the SAR map pixel closest to the buoy coordinate locations. The bias calculated against the predicted mean wind speed at the buoy locations (Fig. 2.9) has a spatial maximum of $1.4\ ms^{-1}$, a mean of $\sim -0.1\ ms^{-1}$ and a RMSE of $\sim 0.6\ ms^{-1}$. At the majority of the sites the mean wind speed derived from SAR exhibits a positive bias relative to the buoy-derived estimate (Fig. 2.9).

2.2.3 QuikSCAT

The term QuikSCAT refers to NASA's SeaWinds Quick Ku-Band Scatterometer. The primary objective of the mission upon launching in 1999 was to measure near-surface ocean winds. Wind information used herein are the daily gridded maps from Remote Sensing Systems (RSS) QuikSCAT v4 ENW, which are retrieved based on the measured surface roughness using the Geophysical Model Function Ku-2011 [89]. The mission lasted until 2009 and its product is available at a much higher frequency (twice daily) than SAR, but at a much lower resolution (~25 km). Thus, wind fields are not directly available close to the coast, where specialized retrieval algorithms are necessary to resolve the wind vectors ([90, 91]). Quality control included rain-flagging and the use of a threshold in data availability, i.e. only grid cells with more than 720 observations were used (approximately the equivalent of 2 observations per day for a one year period). Stronger backscatter signal due to structures offshore could lead to a partial increase in wind speed [92]. However, no backscatter signal information was available from the used product and no screening for traffic could be performed. Data availability from QuikSCAT (Fig. 2.10) is consistently higher than from SAR but is limited to Lakes Superior, Michigan, Huron and Georgian Bay. The high data density from the scatterometer means application of the wind class method as applied to the SAR data is not necessary.

Seasonal Correction

No wind information can be derived from radar backscatter when there is ice formation, so there is a need to correct for the absence of scatterometer data during the ice season. This correction was done using observational data from

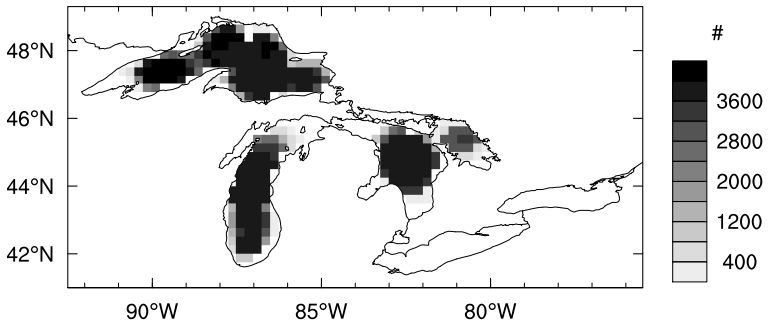

Figure 2.10: Spatial distribution of the availability of QuikSCAT wind speed estimates for each over water pixel (shading) from 1999 to 2009.

the sites that spatially overlap with the QuikSCAT coverage of the Lakes. This translates to 9, 6, and 7 sites for Lakes Superior, Michigan and Huron respectively. For each site, two temporal averages of the wind speeds were calculated: for January-December and for May-December. A ratio r of these means was obtained and averaged spatially for each Lake, and Lake Huron was further divided into main Lake Huron and its northern section, known as Georgian Bay. These mean r values (see Table 2.2) were then used as a scale factor to correct the mean wind speeds obtained from the QuikSCAT scenes. As for SAR, the point biases for the raw and the corrected QuikSCAT estimates were calculated by using the map pixel closest to the buoy coordinate locations. The correction had the largest impact on Georgian Bay, where the bias (relative to the buoy observed wind climates) was the largest and went from $\sim 0.95\ ms^{-1}$ to $\sim 0.60\ ms^{-1}$ after application of the seasonal correction. A slight positive (negative) difference was seen for Lake Superior (Michigan), and no difference for Lake Huron. At Georgian Bay, the number of QuikSCAT observations is significantly lower than for Lakes Superior, Michigan and Huron. Thus, the wind speed correction for missing observations due to ice cover appears to be most useful in regions where the number of satellite observations is lower.

Table 2.2: Temporal and spatial mean winds at 90m for the periods Jan-Dec and May-Dec based on in situ measurements from sites overlapping with the QSCAT coverage, and their ratios. The mean bias of the QuikSCAT resource map is based on buoy time series (Eq. (2.5)), and calculated before and after the seasonal correction was applied.

	Mean Wind Jan-Dec $[ms^{-1}]$	Mean Wind May-Dec $[ms^{-1}]$	Ratio r	Mean Bias Original $[ms^{-1}]$	Mean Bias Corrected $[ms^{-1}]$
Superior	5.9	5.8	1.02	−0.3	−0.2
Michigan	5.3	5.2	1.03	−0.1	+0.2
Huron	5.3	5.3	1.01	−0.2	−0.2
Georgian Bay	5.1	5.4	0.95	+1.0	+0.6

Predicted Wind Speed

Similarly to SAR, the QuikSCAT wind speeds were logarithmically extrapolated to 90 m according to Eq. (2.7). Since these are ENW, the same uncertainty estimate given in Section 2.2.2 applies here. The resource map obtained from QuikSCAT winds with time averaging, seasonal correction for the lack of data during the cold season, and extrapolation to 90 m is shown in Fig. 2.11. The bias values range from -0.3 to 1.6 ms^{-1} (Fig. 2.11). The mean bias is $\sim$ 0.2 ms^{-1}, and the RMSE $\sim$ 0.6 ms^{-1}. In contrast to SAR the positive biases at individual sites are generally of larger magnitude than the negative biases, but the mean bias (averaged across all sites) is of similar magnitude (i.e. -0.1 ms^{-1} for SAR versus 0.2 ms^{-1} for QuikSCAT).

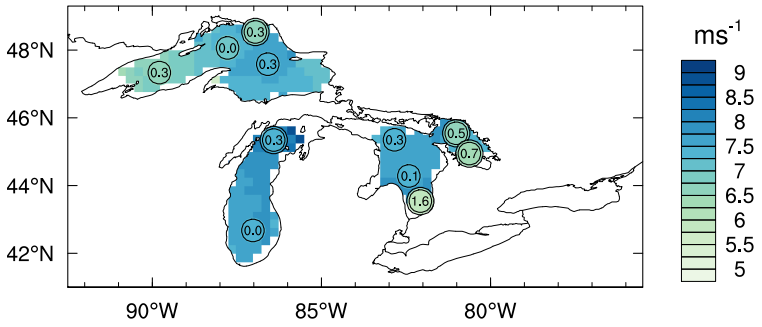

Figure 2.11: Mean wind speed at 90 m as obtained from QuikSCAT equivalent neutral winds from 1999 to 2009 and corrected for lack of ice-season data. Overlaid circles illustrate mean biases in the final resource map where single (double) line represents an under (over) estimation of the resource (in ms^{-1}), in comparison with the wind speed predicted by WAsP at the buoy locations after ice correction.

2.3 Integrated Wind Resource

2.3.1 Integration of Remote Sensing Predictions

The individual mean wind speed maps were regridded into a rectilinear grid of 900 points in latitude by 1800 points in longitude, from 41.0° N to 50.0° N and 93.0° W to 75.0° W. The SAR and QuikSCAT maps were regridded using bilinear interpolation, and the in situ map using a natural neighbor interpolation. These maps were then combined to generate a single integrated wind resource estimate.

The first step was to combine the remote sensing results. The radar and scatterometer winds are obtained with different geophysical model functions and therefore a discrepancy is to be expected between the two data sets. This discrepancy is higher closer to the coast and at low wind speeds [93]. [94] found

that using QuikSCAT wind directions to initialize the SAR wind speed retrievals reduced the inversion biases, and suggested that combining these two data sources provides better wind estimates, especially in coastal areas. This combination also addresses the well recognized issue of a limited number of scenes and irregular coverage of the Great Lakes [91]. In this work, we propose a way of combining these two data sources after individual wind speed maps were already obtained, instead of during the SAR wind speed retrieval. Due to its high spatial resolution, SAR provides high fidelity information on the spatial distribution of wind speeds. The method of classes described in Section 2.2.2 is applied to overcome the temporal sparseness of this data set and provide a more robust estimate of the mean wind. However, this method alone is not sufficient when few scenes are available, and results can be greatly improved when combined with a more reliable estimate of the mean wind. QuikSCAT offers a solution due to its frequent and consistent temporal record. Therefore, we used QuikSCAT to scale the results of the SAR map, thus leveraging the higher resolution of the SAR, while also benefiting from the high data density from scatterometers. First, the mean QuikSCAT coverage was calculated for each Lake as the mean number of pixels for each Lake, normalized against the maximum number of pixels for the entire data set (see Fig. 2.10). These values are shown in Table 2.3. Only lakes for which the mean coverage was greater than 70% were subject to the map-scaling procedure, which excluded Lakes Erie and Ontario and Georgian Bay. Then, a ratio was obtained between the QuikSCAT and the SAR mean wind speeds (spatially averaged over each Lake).

Assuming that the QuikSCAT winds are more representative of the wind resource in terms of magnitude, these ratios (Table 2.3) indicate that SAR underestimated the resource for Lakes Michigan and Huron and overestimated it

for Lake Superior, which is in agreement with the biases calculated against the buoy mean wind climates and shown in Fig. 2.9. Since a single SAR scene does not cover the entire area of interest, the representativeness over each lake is not uniform. To account for that, we allowed the scaling ratios to be different for each lake. The map-scaling procedure decreased the SAR biases by a factor of five, going from a spatial mean of ~ -0.5 to ~ -0.1 ms^{-1}. This method provided better results in comparison to the buoy data than performing a simple average of the two resource maps (see Table 2.3), especially for Lakes Michigan and Huron where the largest SAR biases are seen.

Table 2.3: Mean bias for QuikSCAT, SAR and simple average of both; ratio used for map-scaling; mean percent QuikSCAT data availability; and biases from map-scaled SAR results. Biases are calculated for each buoy site that overlaps with QuikSCAT spatial coverage, and spatially averaged over each lake. u_{qs} and u_{sar} represent mean wind speeds at 90 m from QuikSCAT and SAR respectively.

	Mean Bias SAR $[ms^{-1}]$	Mean Bias QuikSCAT $[ms^{-1}]$	Mean Bias Simple Avg $[ms^{-1}]$	Ratio u_{qs}/u_{sar}	Mean QuikSCAT coverage [%]	Mean Bias Map-Scaled SAR $[ms^{-1}]$
Superior	+0.2	−0.2	0.0	0.97	86	0.0
Michigan	−0.9	+0.2	−0.4	1.14	76	0.0
Huron	−1.2	−0.2	−0.7	1.14	80	−0.3
Georgian Bay	+0.1	+0.6	+0.3		53	+0.1
Spatial Average	−0.5	+0.1	−0.2			−0.1

2.3.2 Integration of In Situ and Remote Sensing Predictions

The next step was to incorporate the wind speed map obtained from coastal stations and buoys into the remote-sensing wind speed map, to ensure that the predicted resource will also be scaled in coastal regions and in the smaller lakes, where a combination of QuikSCAT and SAR is not possible due to the QuikSCAT low resolution. This was done by performing an arithmetic average of the remote-sensing and the in-situ maps. Map-scaling was not applied in this step in order to retain some of the spatial information contained in the stations and buoys map. A 3-by-3 low-pass filter was applied twice to the final map in order to remove artificial high-frequency spatial variability that is introduced when combining the SAR satellite scenes with the wind class method. The final result is shown in a wind atlas format in Fig. 2.12 and the associated mean biases are given in Table 2.4. Note that the "Map-Scaled SAR" biases are different from those in Table 2.3 because here all sites are considered and not only those that spatially overlap with QuikSCAT coverage. The improvement relative to the individual wind speed maps was most obvious for Lakes Michigan and Huron, where the SAR biases were largest.

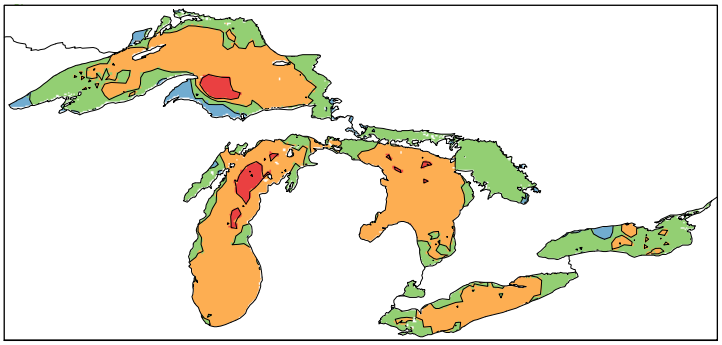

	10 m		25 m		50 m		90 m		150 m	
	ms^{-1}	Wm^{-2}	ms^{-1}	Wm^{-2}	ms^{-1}	Wm^{-2}	ms^{-1}	Wm^{-2}	ms^{-1}	Wm^{-2}
	< 7.5	< 258	< 8.1	< 326	< 8.6	< 390	< 9.0	< 447	< 9.4	< 509
	< 6.6	< 176	< 7.2	< 229	< 7.6	< 269	< 8.0	< 314	< 8.3	< 350
	< 5.8	< 120	< 6.3	< 153	< 6.7	< 184	< 7.0	< 210	< 7.3	< 238
	< 5.0	< 077	< 5.4	< 096	< 5.7	< 113	< 6.0	< 132	< 6.2	< 146

Figure 2.12: Observationally-derived wind atlas for the Great Lakes as obtained from QuikSCAT, SAR, coastal stations and buoys. Wind atlas is described both in terms of mean wind speed (ms^{-1}) and mean energy density ($0.5\rho u^3\ Wm^{-2}$) at five heights (10, 25, 50, 90, 150 m). The mean energy density was calculated assuming the given wind speed as constant. Note that nine-point local smoothing was applied to the plot. The classes and coloring conventions used are as in the European Wind Atlas [3].

Table 2.4: Mean bias and RMSE (boldface) for SAR, Remote Sensing map (Map-Scaled SAR), and Remote Sensing and In Situ map (RSIS) at 90 m. Biases and RMSEs are calculated for all buoy sites, and spatially averaged over each Lake. Differences between the model-based AWST and RSIS wind speed, calculated for the 9 United States buoy sites and spatially averaged over each lake.

	Mean Bias, **RMSE** $[ms^{-1}]$			Mean Difference (AWST - RSIS) $[ms^{-1}]$
	SAR	Remote Sensing (Map-Scaled SAR)	Remote Sensing & In Situ (RSIS)	
Superior	+0.3, **0.3**	+0.1, **0.2**	0.0, **0.1**	+1.2
Michigan	−0.9, **0.9**	0.0, **0.2**	0.0, **0.1**	+0.8
Huron	−0.6, **1.0**	+0.4, **0.9**	0.2, **0.5**	+0.9
Georgian Bay	+0.1, **0.1**	+0.1, **0.1**	0.0, **0.0**	
St. Clair	+0.9, **0.9**	+0.9, **0.9**	0.9, **0.9**	
Erie	+0.2, **0.2**	+0.2, **0.2**	0.1, **0.1**	+0.8
Ontario	−0.3, **0.7**	−0.3, **0.7**	-0.2, **0.4**	+1.5
Spatial Average	−0.1, **0.6**	+0.4, **0.5**	0.1, **0.3**	+1.0

In order to illustrate the uncertainties in both observational and modeling studies, it is relevant to compare the Remote Sensing and In Situ (RSIS) estimate of the wind resource over the Great Lakes (Fig. 2.12) with prior estimates, such as the one produced by AWS Truepower (AWST) from model data and calibrated with observations [70]. To do so, natural neighbor interpolation was used to regrid the AWST map. As shown in Table 2.4, the differences are positive for all Lakes, indicating that the AWST technique predicted higher wind speeds than the method presented in this paper, by a spatial average of $\sim$ 1.0 ms^{-1}. Detailed information about the methods employed to produce the AWST estimates is not publicly available. Thus, differences in the mean wind speeds at 90 m between these two analyses may reflect differences in (i) the time period considered (particularly given the high interannual variability driven by

large-scale climate modes and ice cover in the Great Lakes [69, 95]) (ii) the data sets employed; (iii) the vertical extrapolation and stability corrections; (iv) the treatment of missing observations; and (v) the estimation of roughness length offshore. Future work will focus on quantifying the impact of the study assumptions and climate non-stationarity on Great Lakes wind resources.

2.4 Discussion and Summary

The objective of this work was to produce an observationally-derived wind atlas for the Great Lakes, taking advantage of different data sources, and to provide a blueprint for future observation-based offshore wind resource assessment efforts. Coastal stations provided long (3 to 11 years) and complete records that captured the diurnal, seasonal and interannual variability of the wind resource close to the coast. Buoys provided a long dataset (~11 years) and accurate representation of offshore conditions and were corrected for the lack of data during the ice season using a measure-correlate-predict method of ratios on the mean and mean cubed of the Weibull distribution. A long record of high-resolution North American Regional Reanalysis time series was used as a reference for the buoy correction. Satellite-derived winds contributed with the spatial coverage that in situ measurements cannot provide. QuikSCAT winds offered a spatially and temporally consistent long record (10 years) of wind measurements offshore at a low resolution, and away from the coast. On the other hand, SAR winds provided higher resolution including proximity to the coast, but with an inconsistent and irregular space and time coverage.

A wind resource map was produced individually for each satellite data set

and for the in situ data. For the stations and buoys, small resource maps were generated with WAsP for each data point location and combined through bilinear interpolation and kriging. For QuikSCAT, an arithmetic average was used along with a correction for the lack of observations from January through April that was based on a linear relationship between the QuikSCAT time series and the buoys. This correction was especially valuable in regions where the satellite pixel density was lower. For SAR, the issue of disjunct sampling with varying time intervals and data scarceness was addressed with the wind class method. If the number of SAR scenes is limited, additionally to applying the method of classes the authors suggest scaling the resource based on a reliable wind speed estimate such as QuikSCAT winds. By using a robust wind speed estimate (QuikSCAT) to scale a robust wind speed spatial distribution estimate (SAR) we can obtain a resource map that contains dependable estimates of the magnitude of the wind speed and of its variation in space. This method addresses the issue of limited satellite coverage, and could be successfully employed in other regions beyond the Great Lakes. The scaled map was then averaged with the in situ map to obtain a final resource map that combined all of the observational data sets available for the Great Lakes region.

The uncertainty in the mean wind speeds at 90 m derived from the different data sources and in the combined spatial map are approximated by comparing the mean wind speed at 90 m with the value derived using observations at buoy sites. The atlas generated from all observational data sets presented the smallest biases, with a spatial mean of 0.1 ms^{-1} and a spatial RMSE of 0.3 ms^{-1}. Some of the biases include uncertainties introduced during data processing (i.e., interpolation and gridding routines). Other sources of uncertainty were the assumptions that were made in order to manage the large volume of data, due

to the long temporal record needed for a wind climate estimation and the large spatial coverage of the Great Lakes. The main assumptions were adopting a slightly unstable offshore profile during the generalized wind climate calculations for the in situ data in WAsP, using logarithmic vertical extrapolation, and keeping the satellite data as ENW. The first two assumptions are common in the wind atlas methodology [3]. For the latter, the uncertainty was estimated to be $\sim 0.16\ ms^{-1}$ on average for the Great Lakes, as calculated from the 20 buoy time series.

This work demonstrated that the combination of several observational data sets can yield a robust wind atlas offshore, and that processing each data set separately with subsequent integration is extremely valuable since the biases of the final result are significantly smaller than those obtained when only one data set is used, or when the weaknesses in the data sets are not addressed. The methods presented in this work can be employed to address consistent gaps in time series, and to combine satellite and in situ wind data sets.

CHAPTER 3

WIND TURBINE WAKE MODELING BASED ON NEW METRICS FOR WAKE CHARACTERIZATION

3.1 Introduction

The performance and efficiency of wind power plants are strongly impacted by atmospheric boundary layer conditions such as wind shear and veer, ambient turbulence, and turbine-generated turbulence [96]. A relevant consequence of energy capture by the turbine is that a wake develops as flow advects through the rotor disk, decreasing the wind speed and increasing the turbulence that meets the next generator downstream. Power production is then significantly reduced and fatigue loading is amplified especially during stable regimes [97, 98] when the turbulence intensity is typically low and wake recovery is slower. Ideally, wake effects can be minimized by choosing the optimal turbine placement and spacing within a farm and by developing and implementing robust control systems. Proposed approaches to reduce negative wake effects include curtailing the generator power to decrease the thrust, and yawing or tilting the rotor out of the wind [99]. Turbine siting and controls optimization rely on a thorough understanding of wake and boundary layer interactions [100, 10], for which high spatial and temporal resolution data are necessary. Because such measurements are difficult and expensive to obtain, research is often based on results from scaled experiments [101], numerical models [102, 103], or a combination of both [104].

The models used vary in fidelity and computational cost. The simplest models produce axisymmetric wakes. For example, the well-known Park model

[105, 106] estimates the velocity deficit in the far wake as a function of downstream and radial distance, and free stream wind speed, while considering a previously determined turbine induction factor. The Ainslie model [107] solves the axisymmetric thin-shear-layer approximation to the Reynolds-averaged Navier Stokes (RANS) equations, using an eddy viscosity model to compute the Reynolds stresses. Both models are only valid beyond the near wake (i.e., approximately 2 rotor diameters downstream). A moving quasi-steady wake can be simulated by adding a stochastic component to the Ainslie model in order to account for the wake meandering. This dynamic wake meandering (DWM) model [108] treats the wake as a passive tracer that is advected by the large scales in the ambient turbulent flow. Next in the range of fidelity is full three-dimensional computational fluid dynamics using RANS turbulence modeling, either in steady or unsteady form. In the steady form, used with an actuator disk representation of the turbine rotor, a steady wake is formed. This wake need not be axisymmetric and can be affected by shear, terrain, and stability. In unsteady form, RANS can be used with a rotating actuator line and the large-scale unsteady features of wakes can be resolved. Finally, higher fidelity results can be obtained by performing large-eddy simulations (LES), which entail solving the filtered Navier-Stokes equations at a spatial and temporal resolution that is high enough to resolve the relevant turbulence scales, typically $O(10^0)$ m near the rotor. Different LES codes vary in the treatment of the turbine (e.g., actuator disk versus actuator line [109]), the turbulence closure used (e.g., Smagorinsky versus mixed-scale models [110]), and the numerical schemes. Unlike the simpler models described above, LES provide high-resolution, time-varying solutions suitable for wake dynamics research [103].

The lateral and vertical movement (i.e., meandering) of the wake is an im-

portant component of wake dynamics research. These motions lead to unsteady waking of the downstream turbines and are critical in loads analyses and for obtaining accurate power estimates. A computationally affordable tool to simulate meandering wakes is the DWM model. Several studies have evaluated load estimates derived this from model, which gave good predictions of the mean, minimum, and maximum of the blade-flap, tower-yaw, and tower-tilt moments of a waked turbine in an offshore wind farm [111]. However, the model did not perform well at above-rated wind speeds when comparing the 1-Hz equivalent fatigue loads for these same moment signals. Another study [112] focused on the same wind farm and wind turbine as in [111]. However, in [112], the focus was on the root-mean-square blade-root out-of-plane bending moment, which is closely related to fatigue loading. It was found that the DWM overpredicted these moments substantially when compared to field measurements and LES, but the mean values were predicted well as also found in [111].

These results highlight the ongoing need for a compromise between the high-fidelity, computationally expensive models and the reduced-order, steady, axisymmetric ones. An alternative has been proposed for real-time data-driven applications [113] but an answer is still lacking for predictions under a variety of user-specified atmospheric scenarios. One solution is to develop improvements to the DWM model (e.g., [114]). Ideally, the DWM model should be extended to include the effects of lateral wake merging, and improved regarding its base wake calculation (which is a simple axisymmetric wake). Once that is done, wake-induced loads analyses can be performed with higher accuracy, in more detail, and in multiple wake wind plant situations, but still at a low enough computational cost to allow for large sets of cases to be simulated. In other words, there is a strong desire for a model that captures essential features

of LES-generated wakes at a small fraction of the cost. With that in mind, the objectives of this research are twofold: first, to document wake characterization metrics and their relative performance to serve as a reference for the development of this work and for future wind turbine wake research; and, second, to propose a preliminary wake modeling blueprint that moves away from the steady, axisymmetric framework into one in which wakes are characterized by deviations from axial symmetry (e.g., intermittent edges, stretching), by uneven (i.e., non-Gaussian) deficit profiles, and by unsteadiness.

3.2 Data and Methods

The methods developed here are based on results from a simulation of Offshore Windpark Egmond aan Zee, an offshore wind farm 14 km off the coast of the Netherlands with 36 Vestas V90-3MW turbines. The hub height is 70 m and the rotor diameter is 90 m. The simulation is performed using the National Renewable Energy Laboratory's (NREL) Simulator For Wind Farm Applications (SOWFA) [102], which includes a second-order-accurate, finite-volume fluid solver based on the OpenFOAM toolbox coupled to NREL's FAST tool, a structural and system dynamics model [115]. The turbines are modeled as rotating actuator lines [116] with blade, airfoil, and basic control system data provided by the manufacturer. The Lagrangian-averaged dynamic Smagorinsky model [117] is used. In the horizontal, the domain extends beyond the wind farm area by ~ 1 km on each side. The lower boundary is a flat rough wall with roughness length representative of offshore conditions and the top surface is a zero-stress impenetrable lid at $z = 1$ km above the surface. The spatial resolution of the mesh is 10 m away from the turbine and 1-2 m around the turbines and in the

wake.

A precursor LES of the atmospheric boundary layer is initially run without turbines in order to generate the necessary initial and boundary conditions for the wind plant simulation. The lateral boundary conditions are periodic, and the simulation is driven by a pressure gradient force that allows the hub height mean wind speed and direction to approach a desired value. Coriolis and buoyancy forces are also included. The resulting inflow used to drive the wind farm simulation has a hub-height turbulence intensity of $\sim 4.1\%$ and mean wind speed of $\sim 9\ ms^{-1}$, as shown in Fig. 3.1. The wind direction is $\sim 4^{\circ}$ offset from the main row direction so that in future phases of model development wake merging can also be included. We focus on the first turbine in one of the rows, subject to undisturbed flow. The turbine is yawed into the wind and the wind direction offset does not play a role in the results presented. This specific simulation was chosen as a base data set for the model development because it has already been validated against observations and compared to the DWM in previous work [112] and because multiple turbines and wakes will be needed for future work when more components are added to the stochastic wake shape (SWS) model. The current analysis is based on two-dimensional transverse vertical slices of velocity at two (2 D), four (4 D), and six (6 D) rotor diameters downstream for a period of 20 minutes, at a sampling frequency of 1 Hz.

The ultimate objective of the work is to develop a computationally inexpensive model that simulates wind turbine wakes to a level of accuracy and detail that is comparable to LES wakes and that provides more accurate estimates of fluctuating loads and power than the currently available reduced-order models. The proposed method is based on a modeled wake and it is therefore sensitive

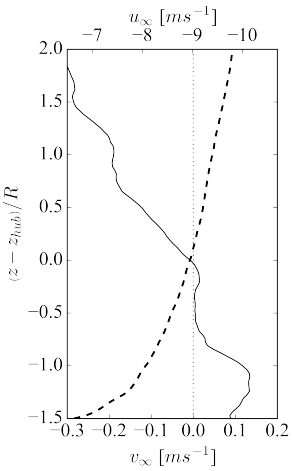

Figure 3.1: Temporal mean of LES free stream vertical wind profiles at the turbine location for streamwise u_∞ (dashed, top axis) and cross-stream v_∞ (solid, bottom axis) components. Dotted line indicates hub height wind speed components $\sim (-9, 0)\ ms^{-1}$. Vertical axis shows height z relative to the hub z_{hub} and normalized by rotor diameter R.

to wake characteristics such as shape, width, height, center, deficit profile, and magnitude of meandering. To base the analysis on robust wake metrics, the first part of this study reviews different ways of characterizing wakes and determines the methods most suitable for the present work. These results are then used to deconstruct the wake in the time and frequency domains and to develop methods that will ultimately generate a synthetic, unsteady wake flow analogous to that in the original LES results.

3.2.1 Global Wake Characteristics

The metrics described in this section are computed for each second of the 20-minute series and at each downstream station, and are used to characterize the LES wake, thus serving as a basis for the development of the SWS model.

- Velocity Deficit

The velocity deficit (vd) in the wake is defined as

$$vd = 1 - \frac{U(x, y, z, t)}{\overline{U}_\infty(z)} \tag{3.1}$$

where $U = \sqrt{u^2 + v^2}$ is the wind speed downstream of the turbine, $\overline{U}_\infty = \sqrt{\overline{u}_\infty^2 + \overline{v}_\infty^2}$ is the temporal mean of the free stream wind speed profile at the turbine location, and x, y, and z are the streamwise, cross-stream and vertical directions respectively (Fig. 3.1).

- Wake Area

  A pre-specified velocity deficit value vd_{edge} is used to distinguish wake and free stream points at each vertical slice. This value is defined to be the 95% confidence interval of the Gaussian approximation for the 20-minute mean LES wake at hub height as given by

$$vd(x, y) = vd_{max}(x) \exp\left(\frac{-y^2}{2\beta^2}\right) \tag{3.2}$$

$$\beta = \sqrt{\log_{10}(2x)} \tag{3.3}$$

  where $vd(x, y)$ are the Gaussian-fitted velocity deficit values, x and y the downstream and cross-stream distances normalized by the turbine rotor radius, $vd_{max}(x)$ the maximum velocity deficit value from the one-dimensional empirical mean wake profiles, and β the wake width parameter. The vd_{edge} values are 0.07, 0.06, and 0.05 at 2 D, 4 D, and 6 D respectively, decreasing with downstream distance as the wake expands and recovers (Fig. 3.2). Note that the double-Gaussian at 2 D can be neglected because the focus of the Gaussian fit is on the tails of the function.

  Due to the spatial inhomogeneity of the momentum distribution, this method identifies spatially isolated, high-deficit regions (low-momentum islands) as part of the wake, and low-deficit regions (high-momentum is-

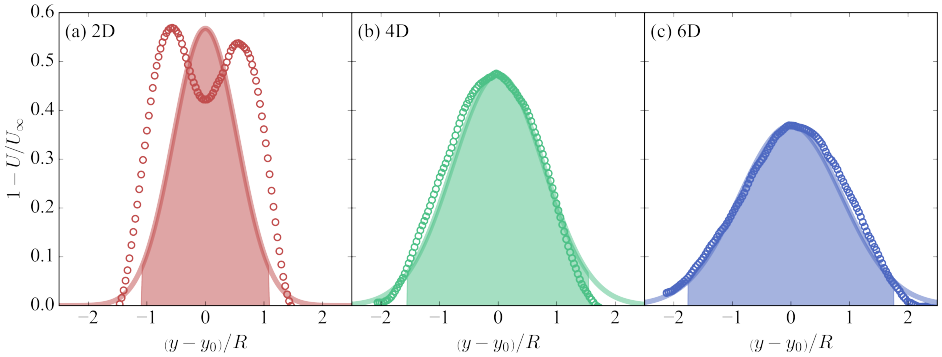

Figure 3.2: Horizontal profile of the 20-minute mean LES velocity deficit at hub height (markers) at 2 D (a), 4 D (b) and 6 D (c) downstream of the turbine, where y is the cross-stream direction, y_0 the mean wake center, and R the turbine rotor radius. The Gaussian approximation is shown by the solid lines and the 95% confidence interval by the shaded region.

lands) embedded in the wake as not being part of it. The algorithm developed aims at defining a primary wake shape in the LES without isolated elements. Therefore, the low-momentum islands are only flagged as part of the wake if they are made up of at least five grid points and if the mean deficit within the island is greater than or equal to the threshold vd_{edge}. The high-momentum islands are flagged as part of the wake if all of their grid points represent a velocity deficit ($vd > 0$). After these steps, the final wake shape is identified as the largest connected region of velocity deficit in the transverse vertical slice.

- Wake Center

  For the model development, the wake center is defined as the center of gravity of the velocity deficit field within the two-dimensional wake shape (cg_{wake}) [118], an accurate estimation method according to [114]. The relative performance of this method is quantified by comparing its estimates to those of three others: as the center of gravity of the deficit plane without defining the wake edge (cg_{plane}), by identifying the center as the point of

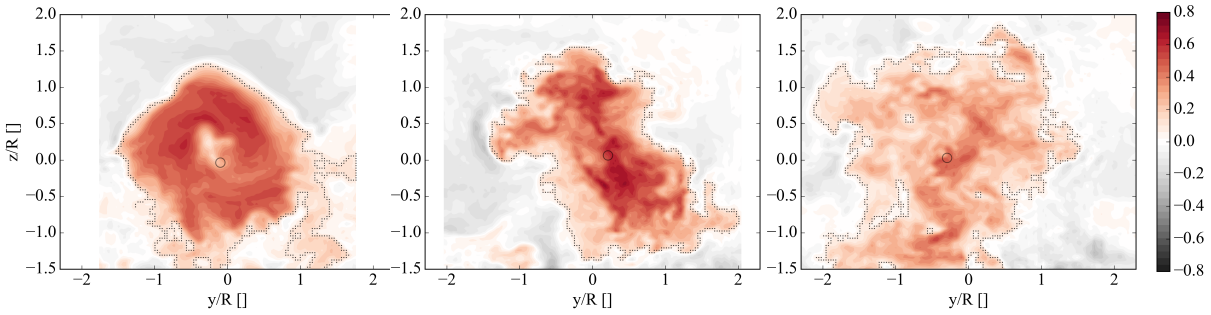

(a) x=2D (b) x=4D (c) x=6D

Figure 3.3: Example of two-dimensional vertical transverse slices of wake velocity deficit from LES as viewed from downstream looking upstream, with wake edges (dotted line) and wake center (circle) identified, for 2 D (a), 4 D (b), and 6 D (c) downstream. Axes are centered at the turbine hub and distances are normalized by the rotor radius.

maximum velocity deficit (*max*) [119], and as the point of best fit [120] between the wake deficit profile and a Gaussian approximation (*Gaussian*):

$$vd(x,\varphi) = \exp\left[-\frac{\left(\varphi-\varphi_{ref}\right)^2}{\left(\frac{R}{\sqrt{2\log 2}}\right)^2}\right] - 2^{-\frac{x}{2R}}\exp\left[-\frac{\left(\varphi-\varphi_{ref}\right)^2}{\left(\frac{0.1R}{\sqrt{2\log 2}}\right)^2}\right]. \tag{3.4}$$

Here, $vd(x,\varphi)$ [ ] is the nondimensional velocity deficit (Eq. (3.1)); x [m], y [m] and z [m] are the streamwise, cross-stream and vertical directions, respectively; φ [m] is the point for which the deficit is being calculated in one of these directions; φ_{ref} [m] is the reference point in the same direction (in this case, the wake center); and R is the rotor radius [m].

- Meandering

  The distance between the wake center and the hub location represents the spatial extent of the meandering. It is calculated in the transverse (δy) and vertical (δz) directions and normalized by the rotor radius R. The mean extent of the wake center displacement is given by $\overline{\delta y/R}$ and $\overline{\delta z/R}$ (from here on an overline represents temporal averaging). The actual magnitude

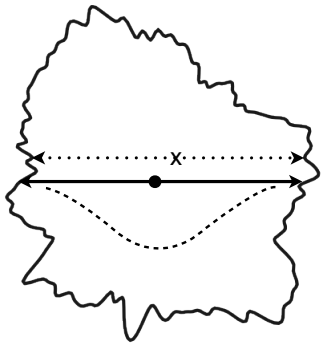

Figure 3.4: Schematic of methods used to compute wake length scales (width and height). The solid line represents the wake edge, the solid circle the wake center and, "x" the hub height. The arrows illustrate the methods: MFoR (solid), FFoR (dotted), and Gaussian (dashed).

of the meandering is quantified as the standard deviation of $\delta y/R$ and $\delta z/R$ in the horizontal (σ_y) and the vertical (σ_z) directions.

- Length Scales

  Three methods are tested for defining wake width and height (Fig. 3.4). Two of them compute the distance from edge to edge along a given direction, considering a moving (MFoR) and a fixed (FFoR) frame of reference. A third method consists of fitting a Gaussian to the deficit profile across the wake center, and using the 95% confidence interval to determine the length along a given direction [97]. These three methods presented very similar results, indicating that for low turbulence intensities it is not necessary to maintain a MFoR when determining the wake length scales, and that a simple method such as determining the largest distance from edge to edge along a given direction yields robust results. For the remainder of this paper, the length scales derived from the FFoR method are used.

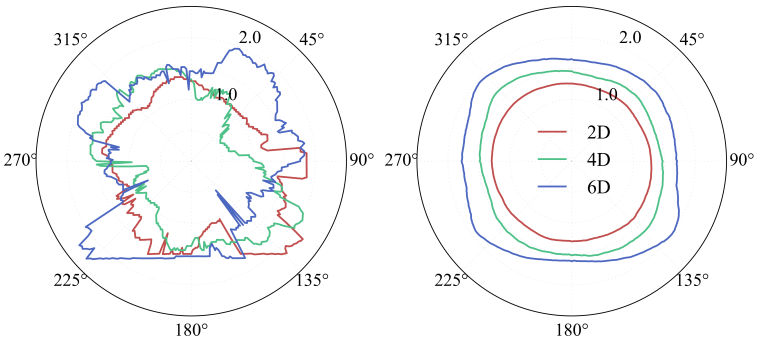

(a) Same time as Fig. 3.3. (b) 20-minute average.

Figure 3.5: Series of wake radii as a function of azimuth $r_w(\theta)$ where 0° – 180° is the vertical direction and 270° – 90° is the cross-stream direction. The view is from downstream looking upstream and centered at the wake centroid. Series are for one time at 2 D (red), 4 D (green), and 6 D (blue) downstream, for the same time as the wake shown in Fig. 3.3 in (a) and for the 20-minute average in (b). Wake radius is normalized by rotor radius.

3.2.2 Azimuthal Wake Characteristics

Once the wake area and edges are identified, it is possible to unravel the wake about its center. For each edge point, an azimuth angle from the vertical and a distance from the wake center are calculated. At each second and downstream distance, a series of wake radius versus azimuth $r_w(\theta)$ is obtained. An example is shown in Fig. 3.5a for the same time instant in which the velocity deficits in Fig. 3.3 are sampled. In the case of a turbulent edge with entrainment of high momentum into the wake (i.e., where the wake edge folds over itself), a single azimuth angle may be identified with several wake edge points. In that case, the point that is furthest from the center is kept so that the larger wake area is analyzed. For each time and downstream location, the set of azimuth values to which the radii correspond differs. To facilitate the comparisons of different times, downstream distances, and turbines, the radii are linearly interpolated to a common set of azimuth angles (ranging from 0° to 360° in 1° increments).

As previously mentioned, the present objective is to deconstruct these LES-derived wake radii series so that they can be regenerated with methods that are simpler and less expensive than running an LES code on thousands of computer cores over many days, as is done to generate this LES data set. Because these radii series are periodic (a different one at each second), a spectral approach is taken to deconstruct the signal. At each time, the azimuthal mean radius $\langle r_w \rangle$ is first removed from the series (from here on the operator $\langle\ \rangle$ represents azimuthal averaging), leaving a series of radii perturbations r'_w. Next, a fast Fourier transform (FFT) is applied to the series of perturbations, decomposing it into a combination of sine and cosine waves at different frequencies f of unit [1/°] or wave numbers k. The low frequencies (lowest is $f = 1/360°$ or $k = 1$) are responsible for large-scale variations in the wake shape such as wake skew, and the high frequencies (highest is $f = 1/2°$ because of the 1° resolution, or $k = 180$) are responsible for the small-scale turbulent fluctuations reflected in the intermittence of the wake edge. For each radii perturbation series, the power spectral density S

$$\Delta f S(j_f) = \left| \sum_{l_f=0}^{N-1} r'_w(l_f) \exp\left[\frac{-i j_f l_f 2\pi}{N} \right] \right|^2 \tag{3.5}$$

is obtained and filtered to keep the wave numbers $2 \leq k \leq 72$, which are responsible for most of the variations in the wake shape. In Eq. (3.5), $\Delta f = 1/360°$ is the bin width in the discrete Fourier transform, $S(j_f)$ is the power spectral density, j_f and l_f are indices from 0 to 359, $r'_w(l_f)$ is the perturbation azimuthal radius at a given frequency (normalized by rotor radius), and $N = 360$ is the number of frequencies. These instantaneous power densities are then averaged over time to yield a mean power spectrum at each downstream distance (Fig. 3.6). The 95% confidence intervals of the mean spectra were calculated with bootstrapping, and are given by the error bars in Fig. 3.6.

These mean spectra present two linear regimes: a low-frequency one ($f < 1/45°$), responsible for the larger-scale oscillations in the wake edge; and a high-frequency one ($f > 1/45°$), associated with the small-scale turbulent structures and presenting a steeper slope as shown in Fig. 3.6. The transition frequency can be mathematically identified as the highest frequency presenting a normalized slope change higher than the mean slope change throughout the spectrum. This happens at slightly different wave numbers at each downstream station. Rotor size, ambient turbulence, and wind speed (and therefore thrust) are expected to affect the relative importance of each wave number to determining the wake shape. Therefore we do not seek to find an absolute regime-separation frequency, but rather an approximate value that will provide a mathematical representation of the phenomenon applicable to a variety of conditions with acceptable levels of uncertainty. The slope is ~ -1.6 (~ -2.1) for the low (high) frequency regime. The uncertainty in the linear approximation of the spectra is $\sim 4.7\%$ and is quantified as

$$\frac{1}{N}\sum_{j_f=0}^{N-1}\frac{S_{j_f}-\widehat{S}_{j_f}}{S_{j_f}} \tag{3.6}$$

where S is the mean power spectral density at a given frequency, $\widehat{S}$ its linear estimate, j_f an index for the different frequencies, and N the total number of frequencies included in the spectra.

3.2.3 Wake Reconstruction from Global and Azimuthal Characteristics

The global and azimuthal metrics described were applied to the LES wake. The results presented in Section 3.3 serve as a basis to develop the SWS simulator.

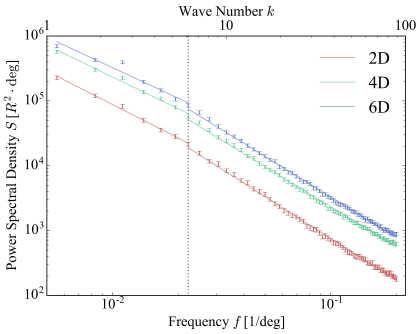

Figure 3.6: Temporal mean of power spectral density of series of azimuthal radii perturbations for 2 D (red), 4 D (green), and 6 D (blue) downstream (markers), and linear fits for the low and high frequency regimes (lines). Error bars give the 95% confidence interval for the mean (from bootstrapping). Dashed vertical line divides the two regimes at $f = 1/45°$.

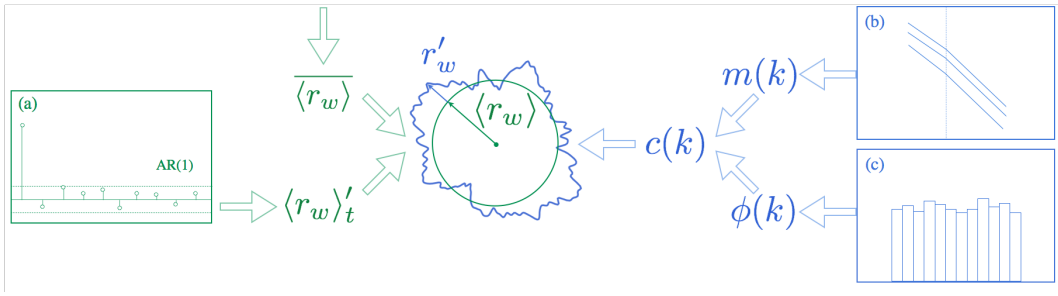

Figure 3.7: Diagram of the SWS model. Estimation of mean $\langle r_w \rangle$ (green) and perturbation r'_w (blue) azimuthal radii. Temporal mean $\overline{\langle r_w \rangle}$ is user-specified, and temporal perturbation $\langle r_w \rangle'_t$ is estimated with a first-order auto-regressive model (a). Mean spectra (b) are used to estimate moduli $m(k)$ and uniform distributions (c) to randomly sample phases $\phi(k)$. They are combined into complex coefficients $c(k)$ and an inverse FFT gives a series of r'_w.

The final results from the developed model are presented in Section 3.4. This section documents the model development in detail. The outline in Fig. 3.7 illustrates all the steps taken at each second to produce an unsteady wake at the three downstream distances considered. The wake intermittent edges are seen as an azimuthal series of wake radii $r_w = \langle r_w \rangle + r'_w$. Both $\langle r_w \rangle$ and r'_w are estimated at each iteration with stochastic (Fig. 3.7, green) and spectral (Fig. 3.7, blue) methods, respectively.

Each instantaneous $\langle r_w \rangle$ value can be further decomposed into a constant temporal mean $\overline{\langle r_w \rangle}$ and a dynamic perturbation $\langle r_w \rangle'$ about this mean. In the wake simulator, $\overline{\langle r_w \rangle}$ is provided by the user as initial condition. For the current simulation, $\overline{\langle r_w \rangle} = 1.29R$, $1.51R$, and $1.77R$ at the three distances downstream, which are the values from the LES time series. The perturbations $\langle r_w \rangle'$ are obtained at every time step through a first-order auto-regressive model (as exemplified by (a) in Fig. 3.7) AR(1) given by

$$\langle r_w \rangle'_t = \rho_1 \langle r_w \rangle'_{t-1} + \varepsilon(t) \tag{3.7}$$

where $\langle r_w \rangle'_t$ is the new value of $\langle r_w \rangle'$ at time instant t, $\rho_1 = 0.9$ is the first-order auto-correlation for the $\langle r_w \rangle'$ time series obtained from the LES data (it is approximately the same for the three distances downstream), $\langle r_w \rangle'_{t-1}$ is the previous value of $\langle r_w \rangle'$ at time instant $t-1$, and $\varepsilon(t)$ are the random innovations in the form of white noise that make up the time series variability. These innovations are randomly sampled from a normal distribution of mean $\mu = 0$ and standard deviation $\sigma = 0.05R$, which were determined based on the original LES time series of wake radii.

Once a mean azimuthal radius $\langle r_w \rangle$ is obtained, the azimuthal perturbations r'_w need to be determined. These turbulent perturbations of the wake edge are a superposition of waves at different frequencies f or wave numbers k, as described in Section 3.2.2. The low frequencies and wave numbers represent the larger-scale eddies, varying more slowly but defining the main shape of the wake. The higher values describe the small-scale random perturbations, which do not greatly affect the wake shape but which still contribute to the intermittence seen along the wake edge. To capture these physical properties, spectral methods based on FFTs are developed to produce synthetic wake shapes. The turbulent edges are generated by performing an inverse FFT on a series of syn-

thetic complex coefficients $c(k)$, which are obtained by combining moduli $m(k)$ and phases $\phi(k)$ for each wave number $2 \leq k \leq 72$. These moduli give the contribution from each wave number to the amplitude of the wake radius perturbation. The phases describe the orientation of the cosine wave in the vertical-horizontal plane from which these radii are sampled. The contributions of different wave numbers are exemplified in Fig. 3.8.

The moduli are obtained from the mean spectra in Fig. 3.6 and the phases are randomly sampled from probability density functions (PDF). These two steps are outlined in Fig. 3.7 (b) and 3.7 (c), respectively. Because the higher wave numbers are associated with random turbulent fluctuations (see Fig. 3.8c) these phases can be randomly sampled from a uniform PDF where $\phi \in [-\pi, \pi]$. The PDFs for the phases of the lower wave numbers are also approximately uniform, except for $k = 2$ and $k = 4$. The wave number $k = 2$ is responsible for the main orientation of the wake (i.e., unidirectional stretching, see Fig. 3.8a). It is most frequent in the interval $[1/3\pi, 5/6\pi]$, indicating a main stretching axis from 315° to 135°, which is in agreement with the cross-stream shear seen in the free stream profile (Fig. 3.1). The cross-stream shear acts to stretch the wake in one direction in its upper half, and in the opposite direction in its lower half, skewing the wake with downstream distance. The phase PDF for $k = 4$ is approximately uniform at 2D with the tails $\phi \in \left[|\pi|, |\frac{2}{3}\pi|\right]$ becoming more pronounced with downstream distance, indicating a tendency for the wake to stretch along the $315° - 135°$ direction as well as the $45° - 225°$ direction, and for the stretching to be more pronounced away from the turbine. For these two frequencies with non-uniform distributions, empirical histograms are used to generate weights for the random sampling of the phases. These moduli and phases form a complex array whose inverse FFT yields dynamic perturbations r'_w that can be added

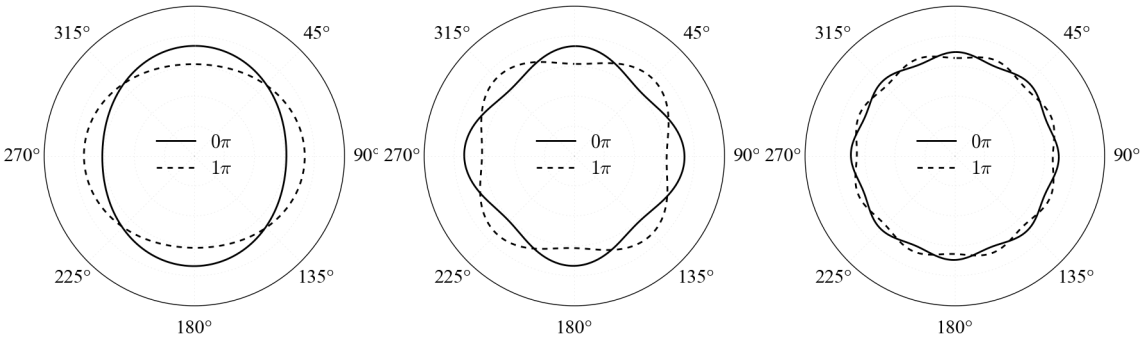

(a) $k = 2$ (b) $k = 4$ (c) $k = 8$

Figure 3.8: Cosine waves for $k = 2$ ($f = 1/180°$) (a), $k = 4$ ($f = 1/90°$) (b), and $k = 8$ ($f = 1/45°$) (c), and $\phi = 0\pi$ (solid) and $\phi = \pi$ (dashed), illustrating the contribution of different frequencies and phases to the variations in the wake shape.

to the mean $\langle r_w \rangle$ in order to obtain a realization of azimuthal radii r_w.

3.3 The LES Wake

3.3.1 Velocity Deficit

The wake area is defined as described in Section 3.2.1. At each time and downstream distance, the mean, maximum, minimum, and spatial standard deviation of the velocity deficit (*vd*) within the wake are computed. The temporal means of these quantities are given in Table 3.1. The mean *vd* decreases by $\sim$ 32% from 2 D to 4 D and by $\sim$ 19% from 4 D to 6 D, where it follows the predictions of similarity theory at infinite Reynolds numbers, which state that $vd \propto x^{-2/3}$ (Fig. 3.9), where x is the downstream distance normalized by rotor diameters [121].

As well as considering the time evolution of the deficit statistics, it is also

Table 3.1: Temporal mean of spatial statistics of wake velocity deficit (*vd*) from LES.

	2D	4D	6D
mean *vd*	0.38	0.26	0.21
max *vd*	0.73	0.66	0.58
min *vd*	0.07	0.06	0.05
std *vd*	0.18	0.15	0.12

important to analyze its spatial distribution. The markers in Fig. 3.2 show the temporal mean of the horizontal velocity deficit $vd(r)$ profile across the wake in the horizontal direction through the wind turbine hub. As expected, the velocity deficit at 2 D presents a local minimum $vd \sim 0.42$ at the hub location, peaking at $vd \sim 0.55$ on either side approximately halfway between the turbine hub and tip, at the points of maximum lift [119]. At 4 D and 6 D, the deficit peaks at $vd \sim 0.48$ and $vd \sim 0.37$, respectively.

3.3.2 Meandering

The differences between the methods used to approximate the wake center are quantified by comparing their estimates for horizontal and vertical meandering. As described in Section 3.2.1, $\delta y/R$ and $\delta z/R$ represent the spatial extent of the meandering-induced wake center displacement. Positive values indicate movement upward and to the left of the flow (i.e., to the right in Fig. 3.3 because the figures look upstream). The temporal means of $\delta y/R$ and $\delta z/R$ indicate the mean extent of the displacement in a given direction. On the other hand, the actual magnitude of the meandering is quantified by the standard deviation of $\delta y/R$ and $\delta z/R$, given by σ_y and σ_z, respectively.

The *max* method presented the least robust results, yielding the largest estimate of the wake center displacement in both directions (Section 3.3.2). This is because the location of maximum deficit is impacted by turbulent motions and moves significantly from time to time, which does not reflect the movement of the wake as a whole, driven mostly by the ambient flow. The three other methods (*Gaussian*, cg_{wake}, and cg_{plane}) present estimates that are similar at 2 D but that diverge with downstream distance. The similarity of these methods can be quantified by the Pearson correlation coefficient r between their wake center estimates. The cg_{wake} and cg_{plane} methods show high correlation values, ~ 0.75 at 2 D and ~ 0.9 at 4 D and 6 D. The same correlations between cg_{wake} and *Gaussian* are also high, ~ 0.7 in the horizontal and ~ 0.6 in the vertical direction for all distances downstream. As expected from the results shown in Section 3.3.2, the correlations between the *max* and cg_{wake} methods are rather low, ranging from 0.03 (horizontal direction at 2 D) to 0.44 (horizontal direction at 6 D). Overall, the cg_{wake} method yielded lower meandering magnitudes in all cases (as quantified by the standard deviation of the normalized displacement of the wake center from the hub location). For this low turbulence intensity scenario ($\sim 4\%$), these metrics yield fairly similar results; therefore, the following analysis utilizes the results produced by cg_{wake}, which is hypothesized to be an accurate metric [114]. For cases with higher turbulence intensities and amplified meandering, these metrics may diverge and therefore will be revisited as the SWS model is expanded to accommodate a wider range of atmospheric conditions.

As the wake length scales increase with downstream distance, so does the meandering. To quantify the magnitude of the meandering relative to the size of the wake, the offset from the hub location δy and δz can be normalized at each second by the geometric equivalent diameter D_{eq} of the ellipse with the same

Table 3.2: Wake meandering as estimated by different methods and quantified by the mean μ and standard deviation σ of wake center displacement from the hub in the horizontal (subscript y) and vertical (subscript z) directions. In the first four rows, displacement is normalized relative to rotor radius ($\delta y/R$ and $\delta z/R$). For last row, normalization is relative to the wake equivalent diameter ($\delta y/D_{eq}$ and $\delta z/D_{eq}$).

	2 D				4 D				6 D			
	μ_y	σ_y	μ_z	σ_z	μ_y	σ_y	μ_z	σ_z	μ_y	σ_y	μ_z	σ_z
max	-0.24	0.46	0.04	0.46	-0.10	0.44	0.21	0.43	-0.15	0.47	0.20	0.51
Gaussian	-0.05	0.14	0.11	0.12	-0.05	0.23	0.12	0.22	-0.10	0.28	0.08	0.27
cg_{wake}	-0.04	0.09	0.11	0.08	-0.08	0.17	0.13	0.14	-0.16	0.21	0.13	0.16
cg_{plane}	-0.07	0.16	0.13	0.13	-0.13	0.24	0.14	0.17	-0.22	0.27	0.15	0.18
$cg_{wake}(D_{eq})$	-0.02	0.05	0.06	0.05	-0.04	0.09	0.06	0.07	-0.07	0.10	0.06	0.07

covariance as the wake area instead of by the fixed value of the rotor radius R. If this is done, the magnitude of the temporal mean of the meandering is constant at $\mu_z \sim 6\%$ of this length scale in the vertical (Section 3.3.2). In the horizontal, it varies between 2% and 7%, increasing with downstream distance. The standard deviation values are also considerably reduced, suggesting that a large portion of the meandering is brought on by the size of the wake itself.

In the horizontal direction, negative (to the right of the flow) meandering occurs more frequently, which is in accordance with what one would expect from the cross-stream vertical wind profile (Fig. 3.1), which is close to zero in the bottom half of the rotor and negative in the upper half. This is most evident at 6 D, where $\sim$ 75% of the horizontal meandering is negative. In the vertical direction, upward meandering is more prevalent at all distances but unlike in the horizontal direction, this proportion is highest at 2 D ($\sim$ 89%). The fact that this

proportion decreases with downstream distance as the wake recovers points to wake-induced eddies as contributors to the upward motion of the wake center. This is in accordance with the hypothesis that the DWM model underestimates the magnitude of the meandering deep in wind farms because it does not properly account for lateral wake merging, an additional source of wake turbulence [112].

3.3.3 Length Scales

As expected from the cross-stream shear of the inflow wind (Fig. 3.1), the temporal mean of the wake shape is stretched along the $\sim 160° - 315°$ direction (Fig. 3.5b). The temporal mean of the wake width (w) at 4 D and 6 D follows the relationship predicted by similarity theory at infinite Reynolds numbers ($w \propto x^{1/3}$, [121]) as shown in Fig. 3.9. These values reflect the wake width along the cross-stream direction through the wake center, calculated at each second with the Gaussian method (see Section 3.2.1). They are lower than the values used to initialize the SWS model (see Section 3.2.3), which represent an azimuthal average of the wake length scale across the two-dimensional plane, thus including directions in which the length scales may be larger due to strong shear and wake skewing. Therefore, when seeking to determine the temporal and azimuthal mean of the wake radius to initialize the SWS simulator, it is necessary to not only rely on theoretical similarity predictions but also to consider the atmospheric conditions, particularly wind shear.

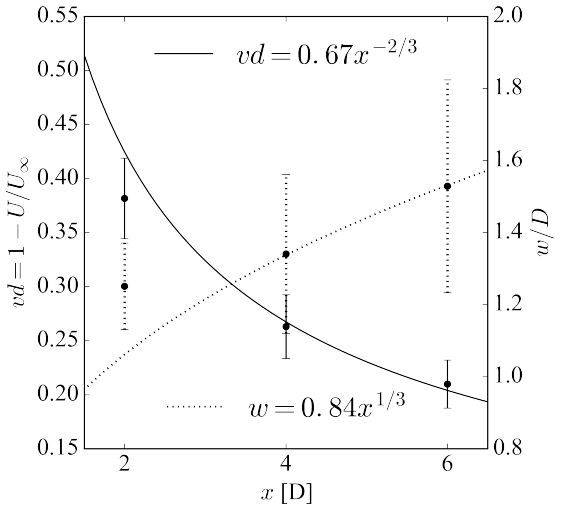

Figure 3.9: Temporal mean of velocity deficit (*vd*, solid) and wake width normalized by rotor diameter (w/D, dotted) at different distances downstream x. Vertical bars are one standard deviation. Curves represent similarity predictions at infinite Reynolds numbers. Wake width is calculated using the Gaussian method described in Section 3.2.1.

3.4 The Synthetic Wake

To simulate a turbulent wake with reduced computational resources as compared to LES, a previously generated turbulence field is normally superimposed onto an axisymmetric wake, as with the DWM model. In this scenario, there is no physical treatment of the turbulence generated by the wake itself. The stochastic model developed in this study takes into account the different length scales present in the unsteady turbulent wake and is a first step toward higher fidelity, affordable wind turbine wake simulations. This section presents the results obtained when using the proposed SWS model to generate a synthetic unsteady wake for the three downstream distances considered. Note that while the model development was based on a LES, its initialization requires only a few user-defined parameters.

An example of the SWS model output at a single time is given in Fig. 3.10a,

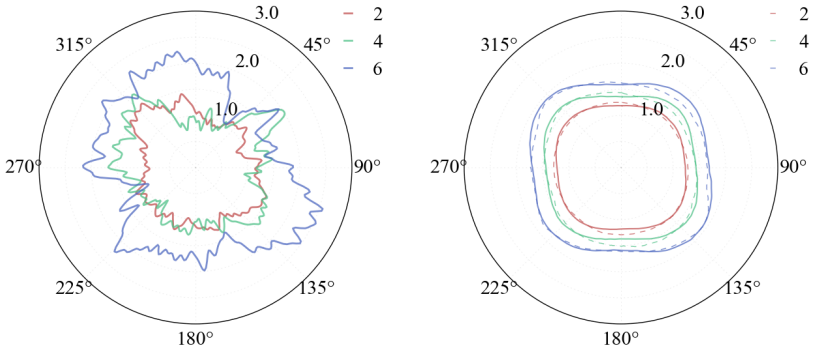

(a) One time. (b) 20-minute average.

Figure 3.10: Series of synthetic wake radii as a function of azimuth $r_w(\theta)$ where $0° - 180°$ is the vertical direction and $270° - 90°$ is the cross-stream direction, and the frame is looking upstream and centered at the wake centroid. Series are for one time at 2 D (red), 4 D (green), and 6 D (blue) downstream in (a) and for the 20-minute average in (b). Wake radii are normalized by rotor radius. In (b), the solid line represents the mean SWS wake and the dashed line represents the mean LES wake.

and the temporal average over a 20-minute period is shown in Fig. 3.10b both for the original LES data interpolated to a $1°$ resolution and for the synthetic data at the same resolution. It can be seen that the synthetic wake reproduces well the mean radii as well as the shearing of the LES wake. The mean and standard deviation of the mean azimuthal radius are very close for both LES and SWS (Table 3.3). The first-order auto-correlation ρ_1 is also reproduced, indicating that the first-order auto-regressive model AR(1) used to account for temporal correlation in the wake shape performs well. The temporal mean and standard deviation of the wake width and height are also well reproduced in the SWS wake.

The relevance of improving the detail of the simulated wake can be illustrated in several ways. For example, it is common to assume axial symmetry in the wake shape and deficit profile in order to reduce the computational cost of simulations. The symmetric wake is then perturbed by some super-imposed

Table 3.3: Comparison of LES and SWS wake for mean azimuthal radius, mean width, and mean height normalized by rotor radius. μ is the mean, σ the standard deviation, and ρ_1 the first-order auto-correlation.

		2 D		4 D		6 D	
		SWS	LES	SWS	LES	SWS	LES
Mean Azimuthal Radius	μ	1.29	1.29	1.48	1.51	1.78	1.77
	σ	0.12	0.09	0.12	0.13	0.11	0.14
	ρ_1	0.91	0.92	0.92	0.93	0.90	0.93
Width	μ	2.53	2.57	2.75	2.96	3.46	3.48
	σ	0.34	0.26	0.47	0.49	0.50	0.57
Height	μ	2.45	2.55	2.79	2.98	3.20	3.27
	σ	0.36	0.28	0.47	0.35	0.50	0.28

turbulent field, often stochastically generated (i.e., a Mann turbulence box or from NREL's TurbSim), in which case the turbulence generated by the wake itself is not included in the simulation results. The SWS model considers both ambient and wake-generated turbulence by deriving methods that are based on a high-fidelity wind farm simulation. To quantify the level of axial asymmetry in the original LES wake and the synthetic wake, an Axial Asymmetry Index (AAI) is defined as

$$AAI = \frac{A_w \ominus A_{sym}}{A_w} \tag{3.8}$$

where A_w is the area of a given wake whose asymmetry is being quantified, A_{sym} the area of an axisymmetric wake of radius equal to the mean radius of A_w, and the operator $\ominus$ is the symmetric difference of the two areas. In other words, this index is an azimuthal mean of the normalized difference between the areas of the asymmetric and the symmetric wakes. It is computed at each time step, and the quotient is proportional to the level of asymmetry (i.e., a value of 0.2 indicates that 20% of the asymmetrical wake area deviated from the idealized, symmetrical shape). Low values indicate that the asymmetrical wake is slightly smaller or larger than the symmetrical approximation, while high

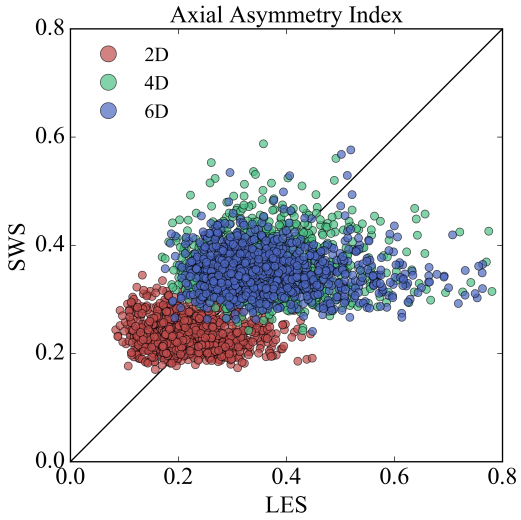

Figure 3.11: Axial Asymmetry Index (AAI) for LES (horizontal axis) and SWS (vertical axis) wake for the 20 minutes of simulation at a frequency of 1s, at 2 D (red), 4 D (green), and 6 D (blue) downstream of the turbine.

values indicate that the symmetric difference area is large in comparison to the wake area. The SWS model produces mean AAI values similar to those from the original LES wake, namely 0.23/0.22 at 2 D, 0.36/0.36 at 4 D, and 0.35/0.36 at 6 D for the SWS/LES wake. The AAI values are higher at 4 D and 6 D (Fig. 3.11) due to enhanced entrainment and wake decay. The scatter seen in Fig. 3.11 is explained by the stochastic nature of the model developed, and the AAI values are not expected to match at each iteration.

CHAPTER 4

CONTRIBUTIONS OF THE STOCHASTIC SHAPE WAKE MODEL TO PREDICTIONS OF AERODYNAMIC LOADS AND POWER UNDER SINGLE WAKE CONDITIONS

4.1 Introduction

Aerodynamic loads refer to the forces exerted by the wind on a turbine. While ultimate loads are brought on by extreme events, fatigue loads are associated with a large number of smaller amplitude stress cycles which in time also lead to structural failure. The fluctuations of these loads around a mean value are a result of atmospheric turbulence and shear, and represent the largest contribution to fatigue damage [112]. Modeling these loads is important for design standards [122] and for designing control algorithms [123].

Since the highest turbulence within a wind power plant is often found in wakes, it is crucial to accurately quantify wake-induced aerodynamic fatigue loads. This can be done by coupling an aeroelastic and a fluid dynamics model. Such models can vary widely in fidelity and computational cost. Unsteady models based on an axisymmetric wake shape [48] are computationally inexpensive tools to simulate flow behind turbines beyond the near wake region. One such model, the dynamic wake meandering (DWM) model, has been shown by [111] to accurately predict mean load statistics and fatigue damage equivalent loads (DEL) in below-rated wind speeds. However, the DWM may over-estimate the root-mean-squared (rms) moments when compared to field measurements and large-eddy simulations (LES) [112]. Improving the fidelity of wake simulations while maintaining the low computational cost is valuable

for more accurate load and power estimation, especially for wind speeds below rated [96].

We propose a stochastic wake shape (SWS) model that moves away from Gaussian axial symmetry and towards a physical description of the wake that accounts for intermittence along the wake edges. Following the initial model development presented in [35], the objective of the present work is to quantify the contribution of the proposed model to simulations of loads and power. This is done by evaluating the relative importance of distinct wake components in wind turbine wake simulations. The models used are described in Section 4.2, the results in Section 4.3 and the final discussion in Section 4.4.

4.2 Data and Methods

In this work, wind turbine wakes are simulated with three different methods which are described in Section 4.2.1. The simulations are run for a total of 10 minutes and results are saved at a temporal resolution of 1 second. The velocity fields are sampled in transverse-vertical planes six rotor diameters (D) downstream of a turbine in the free stream as shown by the schematic in Fig. 4.1. These planes are then used as input to an aeroelastic simulation that calculates the loads experienced by a wind turbine subjected to each of the three velocity fields. The coordinate system is aligned with the mean wind and x, y and z are the streamwise, cross-stream and vertical directions respectively.

The wake is defined as a function of the velocity deficit

$$vd = 1 - \frac{U}{U_\infty} \tag{4.1}$$

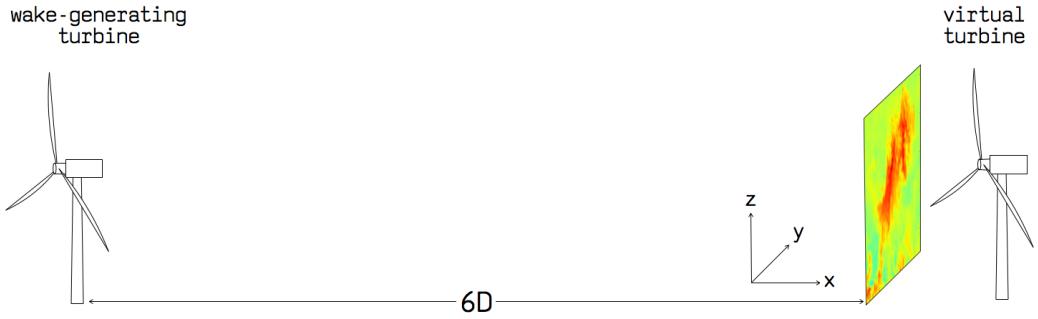

Figure 4.1: Schematic of coordinate system showing wake-generating turbine, the yz transect of wind speeds at 6D and the virtual turbine embedded in the wake.

where U is the horizontal wind speed behind the turbine and U_∞ the free stream wind speed. Vertical wind components are assumed to be negligible. This section describes the three wake models (Section 4.2.1), the methodology used for modeling meandering (Section 4.2.2), the design of the virtual turbine which will be subjected to the modeled wakes (Section 4.2.3), and details of the aeroelastic simulations (Section 4.2.4).

4.2.1 Wake Models

Axisymmetric Wake

For these simulations, the wake shape and velocity deficit (vd) distribution in the yz plane are axisymmetric (AS) around the wake center (Fig. 4.2, left). A Gaussian radial vd profile is initialized for x = 2 D as

$$vd(r) = vd_0 \exp\left[-3.56\,(r/b)^2\right] \tag{4.2}$$

where r is the radial direction from the wake center, the subscript 0 refers to r = 0, and b is the wake width. This profile is used as boundary conditions for

the steady Ainslie [124] solution which is found by integrating the thin shear layer approximation to the Reynolds-Averaged Navier Stokes and the continuity equations in the radial and streamwise directions up to x = 6 D. To allow for a comparison with the LES wake, the the initialization parameters vd_0 and b are set to values that once integrated, yield a wake profile at 6 D that best matches the one from the LES.

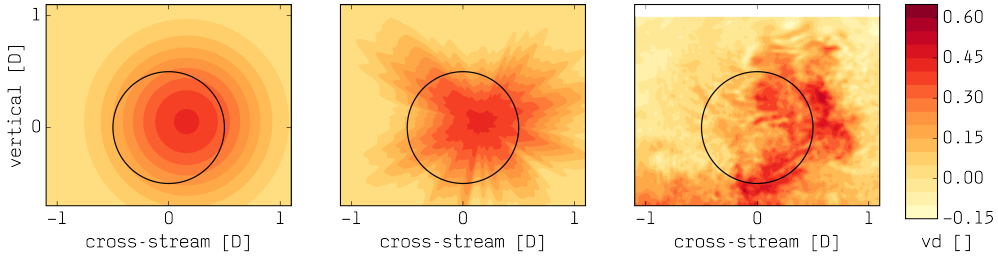

Figure 4.2: Instantaneous single wake with synchronized meandering 6 D downstream of a wind turbine, looking upstream in a fixed frame of reference. AS with Ainslie solution (left), SWS with Ainslie solution (middle), and LES (right). Scale bar gives velocity deficit (unitless). Black circles mark the turbine rotor circumference. Axes are centered at the turbine hub.

Stochastic Shape Wake

A large number of metrics are needed to accurately define both power losses and loads arising from wind turbine wakes. Assuming these can be expressed in terms of vertical slices at discrete distances downstream of the turbine, they include: wake width and height, velocity deficit distribution, wake shape asymmetry and wake meander. In [35] stochastic and spectral methods for defining wake characteristics are developed based on a LES of single wakes in an offshore wind farm. These methods constitute the base of the SWS model, which produces a wake that is unsteady and asymmetric in shape (Fig. 4.2, center).

At each second, a wake shape is simulated on a polar coordinate system at

an azimuthal resolution of 1°. Each point along the wake edge is given by an azimuthal mean radius $\langle r_w \rangle(t)$ and an azimuthal series of perturbations about this radius $r'_w(\theta, t)$ (where t is time, θ the azimuth angle, and $\langle\rangle$ represents azimuthal averaging). At each iteration, the mean radius is determined using a first-order auto-regressive model thus incorporating temporal coherence in the wake shape time series. The perturbations about this mean are obtained from the inverse Fast Fourier Transform (FFT) of a complex series. The phases of the complex coefficients are randomly sampled from probability distribution functions at each iteration. The magnitudes of these complex coefficients are constant for a fixed distance downstream. They are obtained from mean spectra which describe the relative contribution of different wave numbers to the fluctuations in the wake shape. Low wave numbers represent the contribution of large-scale features such as wake skewness due to vertical wind shear and veer. High wave numbers describe the effects of small-scale turbulence on the wake edges.

In this work, the SWS is used to simulate a wake that is subsequently used to drive the aeroelastic simulations. Each instantaneous yz plane is given by the methodology briefly described above. The *vd* distribution is still axisymmetric, and identical to the one in the AS solution. A comparison of SWS and AS therefore allows for an estimation of the contribution of an unsteady, asymmetric wake shape to simulations of loads and power.

Large-Eddy Simulation Wake

This wake is produced by using a rotating actuator-line model [116] for the wind turbine and by solving the filtered Navier-Stokes and continuity equations us-

ing the National Renewable Energy Laboratory's (NREL) Simulator for Wind Farm Applications [102]. Both the wake shape and *vd* distribution are unsteady and asymmetric (Fig. 4.2, right). This dataset has already been validated against observations [112]. It is therefore taken as the reference data set throughout the analysis, and assumed to be representative of actual conditions. We focus on the wake behind a turbine that is subject to free stream conditions, which are generated by running a precursor LES. In the free stream, the hub height streamwise and cross-stream wind components are $(u, v) \sim (9, 0)$ m s^{-1} and and the turbulence intensity is $\sim$ 4 %, with positive (negative) cross-stream shear below (above) the rotor. At 6 D, the temporal mean of the minimum wind speed in the wake is $\sim$ 3.8 m s^{-1}, and the mean wake width is $\sim$ 1.5 D.

4.2.2 Wake Meandering

The relative contribution of meandering to load and power simulations is assessed by deliberately turning it on or off. When meandering is included in the simulations, it is synchronized between the three models based on the meandering time series obtained from the LES simulation as follows: (i) a Gaussian profile is fit to the 20-minute mean LES wake; (ii) the *vd* corresponding to the 95% confidence interval of this Gaussian is used to identify the wake edge at each instantaneous yz slice (Fig. 4.3); (iii) once the wake edge is identified, the center of gravity of the *vd* distribution within the wake area is found; finally (iv) the wake center movement is tracked relative to the turbine hub location. This meandering time series is then used to move the AS and SWS wakes as passive tracers as in the example shown in Fig. 4.2.

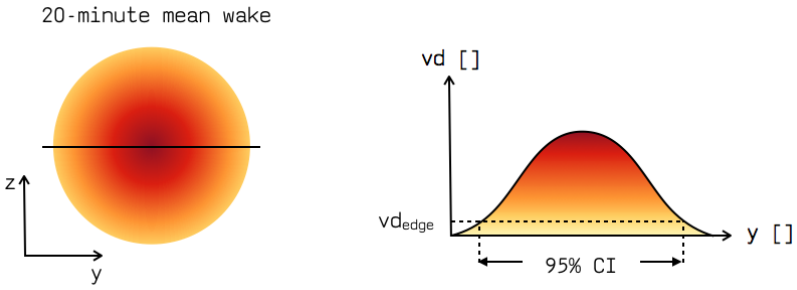

Figure 4.3: Schematic of method used to determine the wake edge at each instantaneous yz transect, based on the Gaussian fit to the velocity deficit distribution of the 20-minute mean LES wake.

Conversely, to assess the contribution of meandering in the LES slices it is necessary to remove the wake motion from the simulated fields. This is done by redefining the origin of the coordinate system at each second to follow the wake center and therefore keeping the wake on a meandering frame of reference instead of fixed at the hub. The subscripts MFoR and FFoR refer to a meandering and a fixed frame of reference respectively [125]. The MFoR follows the wake center and is therefore equivalent to a static wake, centered at the turbine hub. Conversely, the wake in a FFoR is dynamic and its center moves about the hub.

4.2.3 The Virtual Turbine

For the three simulations to be cross-compared and validated against measurements, a virtual turbine was designed to match the rotor size, hub height, and power curve of the turbine that is producing the wakes at the wind farm in the LES. The parameters for the virtual turbine were initially prescribed based on the WindPACT 3 MW turbine [126], and then modified to obtain a better fit to the desired power curve. Additionally to the cylinder at the blade root, three

NREL airfoils were used. Some of the final parameters used are given in Table 4.1. A simple variable speed torque controller was used by setting the rated generator speed, torque, and slip percentage, and the torque constant in region 2. The pitch controller is irrelevant to the analyses because the wind speeds remain below rated where the blade pitch is kept constant.

Table 4.1: Basic parameters describing the virtual turbine.

Rotor diameter	90 m	Generator rating	3 MW
Rotor inertia	1.86E7 kg m^2	Generator speed	1680 rpm
Hub height	70 m	Nominal revolutions	16.10 rpm
Coning angle	-2.5°	Tower diameter	$\in [2.3, 4.2]$ m
Blade pitch	2.6°	Tower thickness	$\in [15.0, 26.0]$ m

4.2.4 Aeroelastic Simulations

The virtual turbine was subjected to wakes from the three simulations, with and without meandering according to the wake modeling component being analyzed. Loads and power for the virtual turbine were calculated using NREL's Fatigue, Aerodynamics, Structures, and Turbulence (FAST) model version 8.12 [115]. The inflow conditions were the transverse-vertical planes of data generated with the models described in Section 4.2.1. The simulations were run for $\sim$ 10 minutes with a time step of 0.005 s, allowing for a transient time of 1 minute. The modules for structural dynamics, inflow wind, aerodynamic loads, and control dynamics were used. The analysis focuses on time series of blade root (BR) out-of-plane (OoP) and in-plane (IP) bending moments, tower base side-to-side (SS) and fore-aft (FA) bending moments, and the respective DEL.

For the blade moments, the values analyzed are an arithmetic average across the three blades.

4.3 Results

This section analyzes the loading and power of the virtual turbine under each simulation, and investigates the relative contribution of different wind turbine wake modeling components.

4.3.1 Virtual Turbine Loading

The aeroelastic simulations initialized with the AS and SWS wakes reproduced well the mean blade root (Fig. 4.4) and tower (Fig. 4.5) loading produced by the unsteady, asymmetric LES fields. The maxima and minima in the time series were not captured, and the variance was underestimated as will be further discussed in Section 4.3.4. It is evident from the time series that including wake shape asymmetry consistently increases the magnitude and variability of the bending moments considered, but a more realistic simulation requires an asymmetric representation of the velocity deficit distribution within the wake as well.

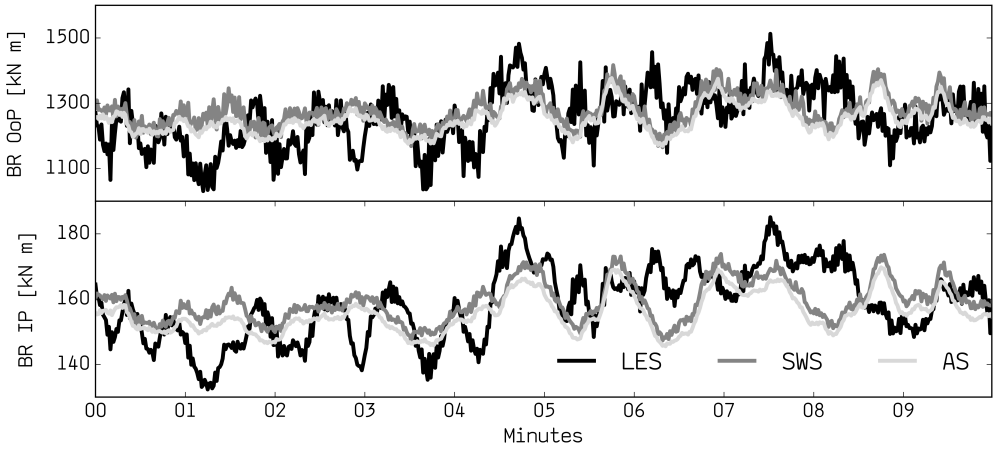

Figure 4.4: 10-minute time series of blade root out-of-plane (top) and in-plane (bottom) bending moments for the three simulations (with meandering).

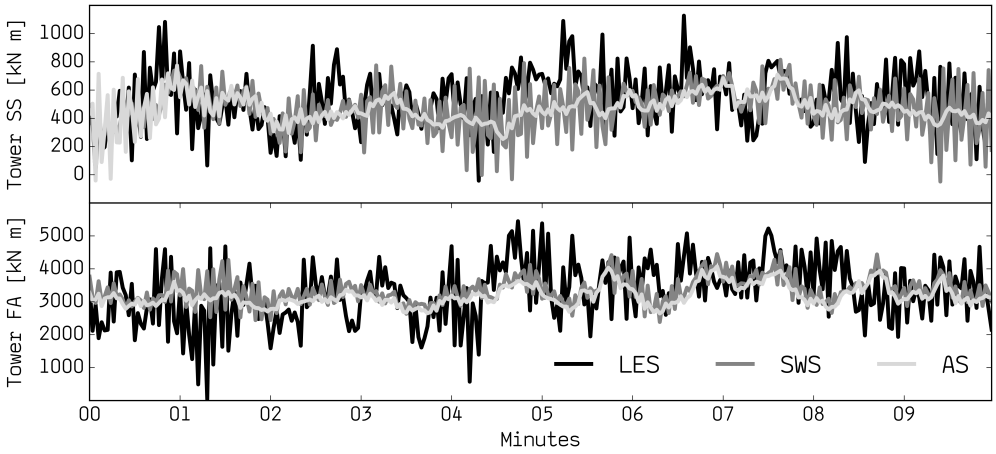

Figure 4.5: 10-minute time series of side-to-side (top) and fore-aft (bottom) tower base bending moments for the three simulations (with meandering).

4.3.2 Virtual Turbine Power

The results for generator power are similar to those seen for the turbine loading. The AS and SWS simulations reproduced the mean generator power but failed to capture the maxima and minima, and the magnitude of the fluctuations. While the asymmetric stochastic shape improved the estimate of the load

fluctuations, it did not significantly improve the simulation of power fluctuations because the deficit distribution within the yz transect remains the same for AS and SWS.

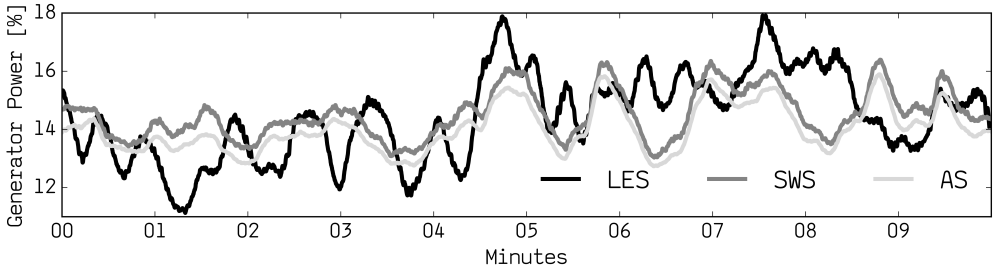

Figure 4.6: 10-minute time series of generator power (normalized relative to rated power) for the three simulations with meandering.

4.3.3 Meandering

Meandering was deliberately turned on and off in the aeroelastic simulations to assess its contribution to the loads experienced by the virtual turbine. The experiment was conducted using the three models: AS, SWS, and LES. The results are quantified by the difference in DEL, which was calculated for the 10-minute time series of bending moments output by the aeroelastic model, considering Wöhler exponents of 4 and 10 for steel and composite materials respectively. The differences are calculated as $(x_{\mathrm{MFoR}} - x_{\mathrm{FFoR}})/x_{\mathrm{FFoR}}$ where x is the load being considered.

The results are shown in Fig. 4.7a and indicate that overall, removing meandering from the models reduced the loads experienced by the turbine. For the LES, the magnitudes of the changes were lowest because the base wake is already asymmetrical in shape and deficit distribution and meandering is only one of the modeling components contributing to loading on the turbine. On

the other hand, meandering is the largest driver of loading for the AS simulation and therefore for this case, the reduction in the loads when meandering was removed is very large, especially for the BR OoP DEL. For the loads in the streamwise direction (BR OoP and Tower FA), the effect of meandering in SWS is much closer to the LES values than the more simplified AS simulation.

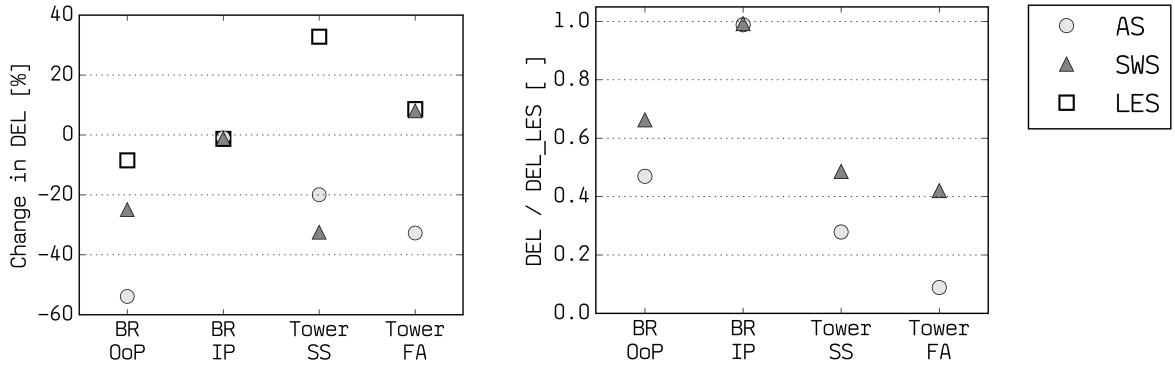

(a) Meandering.

(b) Shape asymmetry.

Figure 4.7: Sensitivity of DEL to meandering (a) and wake shape asymmetry (b).

4.3.4 Wake Shape Asymmetry

The contribution of wake shape asymmetry was assessed by comparing the loads and power produced by three simulations: AS, SWS, and LES. For more realistic estimates, synchronized meandering was including in all of them. DEL for each simulation normalized relative to the LES values are shown in Fig. 4.7b. The added asymmetry in the SWS relative to the AS model improves the load simulations, and the BR OoP DEL is ~70% of the LES value for the SWS wake, despite its axisymmetric deficit distribution.

The intermittence in the loads and power is quantified in terms of rms fluc-

tuations. The values for each simulation are given in Table 4.2. Including the intermittent edges in the simplified wake model improves the simulations of the fluctuating loads relative to LES. However, these fluctuations are still underestimated and other unsteady wake modeling components (i.e., asymmetry in the velocity deficit distribution) should be added to the proposed SWS model to improve its predictive accuracy.

Table 4.2: RMS values of fluctuating loads and power for AS, SWS and LES simulations with meandering.

	unit	AS	SWS	LES
BR OoP	[kN m]	45.4	58.7	110.7
BR IP	[kN m]	5.8	6.2	11.2
Tower Base SS	[kN m]	167.3	310.0	362.3
Tower Base FA	[kN m]	330.5	639.1	1568.3
Generator Power	[kW]	23.4	24.5	43.9

4.4 Conclusion

In this work, the role of different wind turbine wake modeling components was assessed. The main objective was to quantify the contribution of the proposed SWS model to simulations of loads and power, particularly their unsteady fluctuations. Tower base and blade root bending moments were considered and compared across three different simulations with varying levels of fidelity.

It was found that meandering is a large contributor to the loads experienced by the turbine, and that removing it from the simulations can reduce the loading by more than 50% in the case of simplified models. The asymmetry in wake

shape was also found to affect the load magnitudes, with the proposed SWS model producing DEL closer to the reference LES values. Even with an axisymmetric *vd* distribution, the SWS model produced BR OoP DEL values that are ~70% of the LES.

While the SWS model improved the simulation of the fluctuating loads and power relative to the AS model, it still largely underestimates them especially for the FA tower base values. It also fails to capture minima and maxima in the load and power time series. This is likely due to the axisymmetric velocity deficit distribution in the SWS wake. The LES wakes include atmospheric and wake-generated turbulence, and generally show steep gradients at the wake edges where the velocity deficit distribution deviates from Gaussian at the tails.

The results obtained so far testify to the potential of the SWS model proposed in [35] to simulate wind turbine wakes for high frequency load and power estimates. Ongoing work focuses on increasing the fidelity of the proposed model while maintaining its low computational cost. Asymmetry in velocity deficit fields and lateral merging of wakes will be incorporated. These phenomena directly affect the turbulence characteristics and therefore the time series of loads and power on a downstream wind turbine. Future work will additionally validate the aeroelastic simulations relative to high-frequency turbine measurements.

CHAPTER 5

WIND TURBINE WAKE CHARACTERIZATION FROM TEMPORALLY DISJUNCT 3-D MEASUREMENTS

5.1 Introduction

In order to improve the efficiency of wind farms, it is necessary to maximize their overall power production and to minimize the fatigue loads experienced by each turbine. This in turn relies on a quantitative understanding of the flow that meets each wind turbine and its interaction with the tower and rotor. Wind turbines are increasingly deployed in large-scale arrays. The upwind turbines experience undisturbed (i.e., free stream) conditions, where turbulence is determined by atmospheric stability and topographic characteristics. As they extract energy from the wind, turbines also disturb the flow that moves through them generating a wake [96]. As a result, the turbines downstream are subjected to flows with lower mean kinetic energy and higher turbulent kinetic energy. These complex flows are expensive to measure and model with sufficient accuracy. Integrating measurements and models offers the potential to advance quantitative analyses of wake characteristics and atmospheric flows to determine optimal wind farm layout and enable efficient wind turbine control strategies.

Remote sensing tools, such as LiDARs, are advantageous for wind energy applications (e.g., resource assessment and wake characterization) because of their ability to sample beyond hub heights at relatively high spatial and temporal resolution and without modifying the flow. Two major distinctions in wind LiDAR technology are between continuous wave (cw) and pulsed sys-

tems and between their scanning capabilities. While some LiDARs scan exclusively conically using the velocity azimuth display (VAD) technique, others are also capable of range height indicator (RHI, also known as elevation) and plan position indicator (PPI, also referred to as sector or azimuth) scans [127, 128], both of which have been used for wind turbine wake measurements (e.g., [127, 129, 130]). Conically scanning cw LiDARs have been used most frequently for one-dimensional wake analyses to quantify the resulting power losses and wake-induced fatigue either scanning from the ground, when they sample vertical wind profiles at a fixed spatial location [131], or nacelle-mounted, where they can be used to obtain wind profiles through the turbine axis at hub height either downstream for wake research [38, 24] and turbulent dissipation studies [132] or upstream for wind turbine control [133]. Currently, new technologies are being developed that allow for more flexible scanning geometries [134, 127], thus broadening the application range of such systems [135] and exploiting the measuring potential of multiple LiDAR arrays [136]. While cw LiDARs can sample at very short ranges, they are typically limited to distances <200 m because the effective probe volume increases to the fourth power of the focus range [137], thus increasing the uncertainty in the wind speed measurements away from the instrument [138].

Conversely, pulsed scanning LiDAR like the one used in this study are able to sample large three-dimensional (3D) volumes of the atmosphere by achieving ranges $O(10^2 - 10^4)$ m and measuring at several pre-determined azimuth and elevation angles. They can also measure wakes from the ground [129] or can be mounted on the turbine nacelle [24]. The sampling duration of one 3D scan increases linearly with the number of azimuth and elevation angles sampled because it takes time for the instrument to retrieve robust statistics of the

Doppler shift at several range gates and to mechanically reposition the transmitter before emitting the next beam. At the cost of sampling a large number of points, the time interval between two beams is ~2 s for the measurements used in the present study. The dwell time of the instrument is ~1 s (higher than some other studies, e.g., 0.2 s in [139]), and the additional time is spent in processing the return signal and relocating the scanner. This instrument time combined with the large number of beams required to sample a large volume results in measurements that represent neither a snapshot of the atmosphere nor a mean field. They are instead a set of instantaneous observations sampled at different times and locations. When such measurements are used to characterize the unsteady, inhomogeneous flows in wind turbine wakes, it is important to have a measure of the uncertainty in the retrieved data that considers the instrument limitations, the scanning geometry characteristics and the assumptions being made for data retrieval and analysis. While previous work has quantified LiDAR-derived radial velocity uncertainty and proposed means to reduce it (e.g., [140]), the present work is unique in that it focuses on wind turbine wake characterization metrics.

The notion of combining LiDAR and models to improve processing techniques and understand uncertainty propagation has been around for over a decade [141]. As LiDAR use becomes more widespread and computational resources develop, this approach is gaining popularity. Recently, studies have started to combine high-fidelity large-eddy simulation (LES) and LiDAR to investigate near wake physics [142] and quantify errors prior to conducting measurement campaigns [39]. The first part of the work presented here utilizes this approach to estimate the differences between wake measurements obtained with a scanning pulsed LiDAR, the true snapshot of the same volume and the

true temporal mean over the time it takes to complete a full 3D scan. The analysis is conducted by placing an imaginary scanning LiDAR in an LES to obtain scans that are equivalent in time and space to measurements collected during a field campaign. The differences serve as an estimate of the uncertainty when temporally-disjunct point measurements are assumed to be representative of mean conditions. The disjunct points, the instantaneous fields and the true means are then used to characterize the wake, and differences in the wake metrics are obtained to further quantify uncertainty in wake characterization from LiDAR observations. We focus on a single ground-based instrument and present wake characterization metrics that can be used when resources are limited and multiple or nacelle-mounted units are impractical.

The second part of this work seeks to identify and characterize single-wake conditions measured with a pulsed scanning LiDAR during a 22-h period with a fixed scanning geometry. The wake metrics considered include wake center, length scales, orientation and velocity deficit (vd) statistics and are defined for transverse-vertical planes at discrete distances downstream of the wake-generating turbine following the methodology proposed in [35]. A significant challenge is the time-varying wind direction and rotor yaw, which dictate the angle between the fixed scanned volume and the vertical planes. We quantify this effect by proposing scanning geometry indices that describe the measurement coverage and density on a vertical plane given an area of interest and an optimal spatial resolution between the sampled points. The field measurements and simulations are described in Section 5.2, and the results given in Section 5.3. Recommendations for defining the scanning geometry prior to measurement collection and for characterizing mean wakes from temporally disjunct point measurements are proposed along with a final discussion in Section 5.4.

5.2 Materials and Methods

5.2.1 Field Scans

The observational dataset used in this work was collected during the Prince Edward Island Wind Energy Experiment at the Wind Energy Institute of Canada [34]. We focus on single wake measurements during a 22-h period (26 May 2015 13:00 UTC–27 May 2015 11:00 UTC) downstream of a 2-MW DeWind D9.2 turbine with a hub height (z_H, the H subscript indicates turbine hub throughout the manuscript) of 80 m and a rotor diameter (D) of 93 m. The wake characterization is based on the metrics proposed by [35], which are defined for two-dimensional planes of data in the cross-stream (x) and vertical (z) directions. This framework allows for an analysis of the wake expansion and deformation with downstream distance, which are directly related to wake recovery and to the loads experienced by downstream turbines. Vertical planes are typically obtained with ground-based LiDAR using RHI scans, in which the azimuth angle (θ) is kept constant and the elevation angle (ϕ) is varied. However, in the present work, the mean flow direction (y) is perpendicular to the plane of interest (xz), precluding the use of RHI scans. Stacked sector scans must be used instead, which are obtained by varying θ at multiple ϕs.

The sector scans in this work were obtained using a Galion LiDAR, which has a wavelength of 1.5 μm and a pulse repetition frequency of 15 kHz. Throughout the manuscript, the terms "stacked (sector) scans" and "3D scan" are used interchangeably when referring to the volume probed by all of the θ and ϕ beams. The scanning geometry was constant for the entire measurement period and can be visualized in Fig. 5.1. A total of N_θ = 46 azimuth angles were

configured in the interval $\theta \in \{[351°, 360°] \bigcup [0°, 81°]\}$, and their position relative to the site and the turbine is given in Fig. 5.2, which also shows the location of a meteorological mast with a Gill sonic anemometer measuring at a frequency of 10 Hz at a height of 60 m. The azimuth angles follow the meteorological convention where $\theta = 0°$ points north. The elevation angles were $\phi \in [3°, 19°]$ for a total of $N_\phi = 8$ elevation beams, and $\phi = 0°$ is aligned with the approximately flat ground (Fig. 5.2). Each radial velocity measurement is defined by the coordinates (θ, ϕ, r) where r is the radial distance from the instrument along the laser beam, with a relatively high resolution range gate size of 30 m (as compared to >100 m in [127, 139], 72 m in [128] and 18 m in [129]). During this period, 111 3D scans were obtained. The method used to derive vertical planes of data from the 3D scan is outlined below.

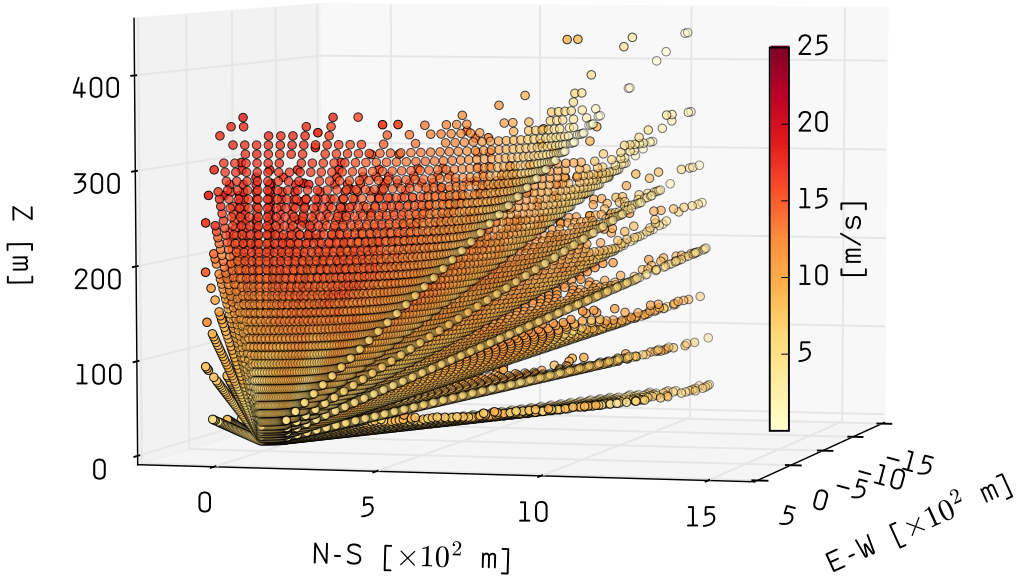

Figure 5.1: Scanning geometry used during the experiment, with example retrieved radial velocity measurements U_r (shading). The instrument location is at the origin, and the coordinates are aligned with the north-south (N-S) and east-west (E-W) directions. Note that the vertical axis is exaggerated for readability.

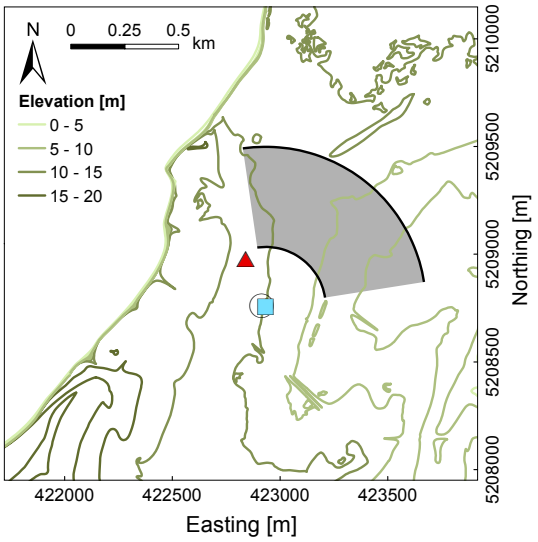

Figure 5.2: Map of the experiment site (NAD1983, UTM Zone 20 N) showing the locations of the turbine (hollow circle), LiDAR (blue square), the meteorological mast with the sonic anemometer (red triangle), elevation contours and the azimuthal span of sector scans from 3–8 D downstream of the instrument, when the wind direction is aligned with the center of the arcs.

1. Data are filtered by range gate number (G), signal-to-noise ratio (SNR) and radial velocity magnitude (U_r). The criteria are:

$$2 \leq G \leq 45$$

$$0.01\ (-20\ \text{dB}) < SNR \leq 10\ (10\ \text{dB})$$

$$U_r < 30\ \text{m s}^{-1}$$

and therefore, the total possible number of radial velocity measurements within a stack of scans is $44 \times 46 \times 8$ (number of gates $\times N_\theta \times N_\phi$). The first range gate is discarded as it is in the LiDAR blind zone. The SNR lower limit is recommended by the manufacturer, and the upper limit (also used in previous studies [139]) is enough to filter out hard targets and cloud water for our dataset. The upper limit in the radial velocities is an arbitrary value higher than any of the observed values during the measurement pe-

riod (e.g., Fig. 5.1) and serves to filter out unrealistic measurements and erroneous logging.

2. The location vector in Cartesian coordinates in a fixed frame of reference for each point is obtained as:

$$\vec{d_F} = (x_F, y_F, z_F) = (r\cos\phi\sin\theta, r\cos\phi\cos\theta, r\sin\phi)$$

where x_F (y_F) is positive in the east (north) direction. All quantities in the fixed frame are subscripted with F.

3. For each 3D scanned volume, the highest elevation sector scan ($\phi = 19°$) is selected to determine the mean wind direction $\langle\beta\rangle$ (angled brackets refer to values averaged over the entire 3D scan). Within this scan, all points sampled at least 0.25 D above the rotor are considered, which includes five range gates. An estimate of the horizontal wind components u_F and v_F is obtained for each range gate within this sector scan sub-sample by solving the linear system:

$$\begin{bmatrix} \cos 19°\sin\theta_1 & \cos 19°\cos\theta_1 \\ \vdots & \vdots \\ \cos 19°\sin\theta_{46} & \cos 19°\cos\theta_{46} \end{bmatrix} \begin{bmatrix} u_F \\ v_F \end{bmatrix} = \begin{bmatrix} U_{r_1} \\ \vdots \\ U_{r_{46}} \end{bmatrix} \tag{5.1}$$

using a least-squares approach, where (u_F, v_F) are the wind components along the directions (x_F, y_F) and U_{r_i} are the radial velocity measurements along an arc of constant G for an azimuth angle θ_i. The vertical component w_F is assumed to be negligible, consistent with previous studies (e.g., [143]). The validity of this assumption was verified with sonic anemometer data (not shown) and is based on the physical understanding that the magnitude of vertical velocities is much lower than that of horizontal velocities and that the mean magnitude of w is close to zero when averaged

over periods of ~10 min, which is approximately the time the LiDAR took to complete a full stack of sector scans. As suggested in [129], multiple LiDARs must be considered when seeking to investigate all components of the wind field within wakes.

The values of (u_F, v_F) are then averaged across the five range gates within the sub-sample to yield the mean wind direction estimate $\langle\beta\rangle$ for the scanned volume. The robustness of this method for the present experiment is reflected in the time series shown in Fig. 5.3, where the minimum and maximum $\langle\beta\rangle$ estimates for each 3D scan are compared with sonic anemometer measurements and the turbine nacelle position. The LiDAR estimates follow the sonic values more closely than the turbine data, indicating that the assumptions of low veer and negligible vertical velocity are acceptable for the atmospheric conditions observed during the experiment.

4. Assuming a constant mean wind direction $\langle\beta\rangle$ for each 3D scan, the horizontal wind speed at each point $U_F(x_F, y_F, z_F)$ is estimated from the radial velocity U_r as:

$$U_F = -\frac{U_r}{\cos\phi\cos\Delta\theta} \tag{5.2}$$

where $\Delta\theta = \langle\beta\rangle - \theta$ is the scan offset, defined as the angle between the scan wind direction and the laser beam azimuthal direction. Orthogonal scans are filtered out following the LiDAR manufacturer recommendation to remove points for which the laser beam makes an angle between 70° and 110° with the mean wind direction (~1.4% of the measurements).

5. All points in the scan are rotated so that the coordinate system is aligned with the mean wind direction. Throughout the manuscript, the quantities

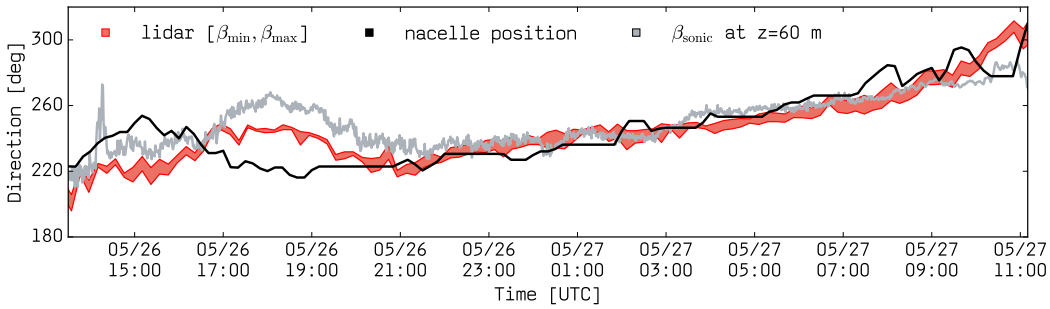

Figure 5.3: Wind direction as estimated from LiDAR measurements at least 0.25 D above the rotor (red line, lower limit = β_{min} and upper limit = β_{max}), the turbine nacelle position as measured and provided by the turbine operators (black line) and the wind direction at 60 m (gray line) measured with a sonic anemometer (β_{sonic}) and averaged over 2 min for readability.

in this streamwise frame of reference are given without the F subscript as: $\vec{U} = (u, v)$, $\vec{d} = (x, y)$ where x and y are the cross-stream and streamwise directions, respectively.

6. Vertical planes of data are obtained at a given distance downstream of the turbine by selecting all of the sampled points whose streamwise coordinate y falls within the desired distance plus or minus some specified buffer Δy, taken to be the range gate width of 30 m. In this analysis, the scanning LiDAR was deployed at the base of the turbine (Fig. 5.2), and we apply an assumption of no yaw error. Therefore, the analysis only considers 3D scans for which the LiDAR-estimated $\langle\beta\rangle$ is within 15° of the turbine nacelle position, resulting in 80 sector scan stacks. The value of 15° was chosen as a threshold because while it is small (half of the wind industry standard 30° sectors when performing azimuthal analyses), it still allows for an offset between the turbine and the nacelle, which is necessary given the uncertainties inherent in both datasets (e.g., inaccuracies in the wind direction estimate from the LiDAR and in the recorded nacelle position) and the potential presence of yaw misalignment. As indicated by the sonic time series (Fig. 5.3),

the large differences between the LiDAR and the nacelle datasets reflect not an inability of the LiDAR to estimate the wind direction, but rather the necessarily delayed response of the nacelle to wind direction changes or high uncertainty in the turbine measurements.

7. In order to quantify the potential contribution of each vertical slice to wind turbine wake characterization, it is important to consider how much of the area of interest is covered by the sampled points and how dense this coverage is. To do that, we define two indices. The first one is the scanning geometry coverage (SGC), which is calculated as:

$$SGC = \frac{A}{A_{ref}} \tag{5.3}$$

where A is the area covered by the scanned points within the total reference area A_{ref}, which extends 1 D to either side of the hub in the horizontal and vertical directions being only limited by the presence of the ground. Within the covered area A, the scanning geometry density (SGD) is defined as:

$$SGD = \frac{n}{n_{ref}(\Delta x, \Delta z)} \tag{5.4}$$

where n is the number of points in the covered area A relative to a reference value n_{ref}, which is the maximum number of points that could cover the same area A given a desired fixed spatial resolution Δx and Δz, which for the present study is set to 5 m.

The scanning geometry coverage and density vary with downstream distance and with wind direction (Fig. 5.4), which dictates the turbine yaw and, therefore, the angle of the xz-plane relative to the fixed scanned volume. The scanning geometry θ angles are fixed for the period considered

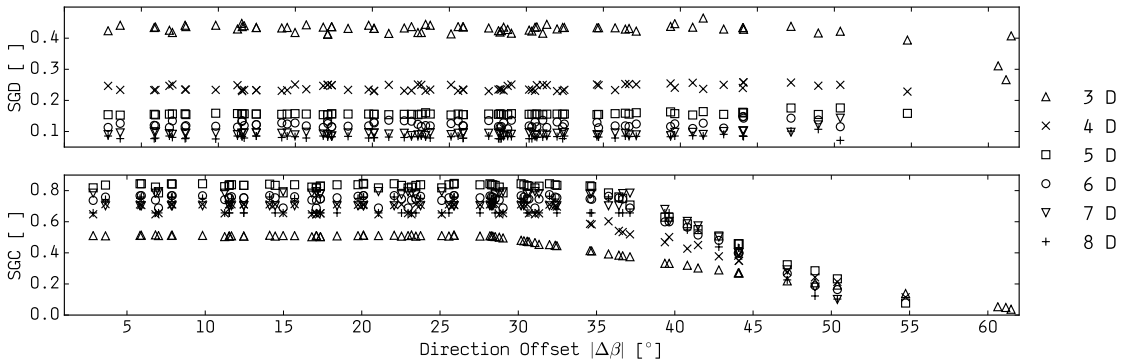

Figure 5.4: Scanning geometry density (SGD, top) and coverage (SGC, bottom) indices calculated for vertical planes at discrete downstream distances of the turbine from 3 D–8 D, as a function of the absolute value of the wind direction offset ($|\Delta\beta| = \left|\langle\beta\rangle - \beta_{opt}\right|$) for measurements with the constant scanning geometry described in the text.

and were determined at the start of the day based on the forecast wind direction. The optimal wind direction β_{opt} is defined as the wind direction that yields the best coverage of points for a given scanning geometry. For the period considered in this study, $\beta_{opt} = 216°$ and aligns with the center of the scanning arc at $\theta = 36°$, which is the symmetry point around which the sector scan stacks return ample coverage in the horizontal direction. It is convenient to define the direction offset $\Delta\beta = \langle\beta\rangle - \beta_{opt}$ as the difference between the actual wind direction during a scan and the optimal value for that given scanning geometry. For the present setup, the coverage is lowest for westerly winds when half of the xz-planes are outside of the scan (Fig. 5.2). The SGD values do not approach unity because of the high n_{ref} value used in its definition. Similarly, $SGC < 0.9$ for the present scanning geometry since the θ and ϕ angles were chosen to maximize the retrievals at several distances downstream rather than focusing on obtaining complete coverage within a narrow range in the streamwise direction.

5.2.2 Synthetic Scans

The uncertainty in the measurements and resulting wake characterization is estimated by placing an imaginary scanning LiDAR at the bottom of a wind turbine in an LES of a single wake under slightly stable conditions, which is also true of the measurements [34]. From here onwards, the term "synthetic scan" is used to refer to data that are obtained by sampling numerical simulation output according to the spatial and temporal coordinates of each point in the xz-planes obtained from the field measurements. The LES dataset is obtained with the National Renewable Energy Laboratory's (NREL) Simulator For Wind Farm Applications (SOWFA) [102] using the Lagrangian-averaged dynamic Smagorinsky model [117]. The turbines are modeled as rotating actuator lines [116]. The lower boundary is a flat rough wall with the roughness length representative of offshore conditions, and the top surface is a zero-stress impenetrable lid 1 km above the surface. The offshore simulation is assumed to be a good approximation to the field experiment site, which is narrow ($\sim 10^3$ m in width), approximately flat (Fig. 5.2) and surrounded by ocean [34].

The spatial resolution of the simulation mesh is 10 m away from the turbine and 1–2 m around the turbines and in the wake. The turbine has a 77-m rotor diameter and an 80-m hub height. A precursor LES of the atmospheric boundary layer is initially run without turbines in order to generate the necessary initial and boundary conditions for the wind turbine simulation, and the resulting inflow has a hub height turbulence intensity of ~4% and a mean wind speed of ~6.5 $\mathrm{m \cdot s^{-1}}$. The lateral boundary conditions are periodic, and the simulation is driven by a pressure gradient force that allows the hub height mean wind speed and direction to approach a desired value. The data are saved in

xz-planes at discrete distances downstream of the turbine at a frequency of 1 Hz for a 12-min period. The effect of the weighting function relative to the temporal lag across points is assumed to be small when sampling the synthetic scans, since the focus of the current study is to assess the impact of the temporal and spatial resolution of the sampled points on wake characterization metrics.

As described in Section 5.2.1, each 3D scan obtained in the field is characterized by a different mean wind direction $\langle\beta\rangle$ and therefore has a different coverage and density of points in the xz-planes being analyzed. The method employed in this work to obtain the synthetic scans from LES data accounts for this dynamic behavior of the sampled points and for the instrument dwell time. The same 12-min LES dataset is resampled for the appropriate points each time that the field LiDAR starts a new 3D scan. Therefore, the synthetically-scanned points are equivalent to the field scans spatially and temporally. The LES data are denoted with the subscript L and the temporally disjunct synthetic scans with the over-ring symbol: $(\mathring{u}_L, \mathring{v}_L)$. It takes the instrument ~2 s to sample radial velocities along one combination of θ and ϕ. For the 46 azimuth and 8 elevation angles considered, a full scan takes ~12 min, and the sampled values do not represent instantaneous nor mean fields. The difference between the sampled points and the true 12-min mean or instantaneous fields can be estimated by using the LES data. Throughout the manuscript, true instantaneous fields are denoted by (u_L, v_L) and are sampled at the first second of the scan. Temporal means over the time it takes to complete a full 3D scan are obtained from 1-Hz data and denoted by the overbar $(\overline{u}_L, \overline{v}_L)$.

5.2.3 Wake Identification

From this point onwards, the methodology applied to the field and synthetic wakes is the same except when noted. The first step towards wake characterization is to distinguish free stream from wake points. The scanned points at each vertical slice are interpolated onto a regular grid with a spatial resolution of 5 m, and the *vd* is calculated for each plane as:

$$vd(x,z) = 1 - \frac{U(x,z)}{U_\infty(z)} \tag{5.5}$$

where $U = \sqrt{u^2 + v^2}$ is the horizontal wind speed downstream of the turbine and retrieved from the scan (whether the points are temporally disjunct depends on the case being analyzed), and $U_\infty = \sqrt{u_\infty^2 + v_\infty^2}$ is the free stream wind speed. During the 22-h period considered, no free stream measurements were performed in the field. Therefore, the free stream profile must be estimated from measurements downstream of the turbine $U_\infty(z) \approx U_{\infty,down}(z)$. On each *xz*-plane, the profile that is furthest away from the turbine hub in the cross-stream direction is assumed to be representative of free stream conditions:

$$U_{\infty,down}(z) = U(x_{max}, z) \tag{5.6}$$

To avoid sampling a profile that is in the wake when data coverage is limited, we constrain the minimum acceptable distance away from the hub as half the rotor diameter plus an expansion factor based on the Jensen model [106]:

$$x_{max} > 0.5 + ky \tag{5.7}$$

where y is the downstream distance in units of D and k the wake decay coefficient, taken to be 0.05 as traditionally used for offshore conditions as the default parameter in the WAsPPark model [144]. The sensitivity of this parameter to atmospheric stability is beyond the scope of the present study, and the adopted value is consistent with recommendations from previous studies [144, 145]. For the synthetic scans exclusively, available upstream data are used as an additional measure of the free stream where $U_\infty(z) \approx U_{\infty,up}(x_H, z)$.

The points with a *vd* value above a minimum threshold are flagged as wake points. To determine this threshold, a Gaussian function is fit to the horizontal *vd* profile at hub height, as has been done in previous LiDAR wake characterization studies [125, 146]. The 95% confidence interval of the Gaussian (2σ) is then used to determine the threshold *vd* value to mark the wake edges for a particular *xz*-plane. The horizontal direction is chosen here because the scanning geometry covers a greater range in azimuth than in elevation (which misses the upper part of the wake closer to the turbine) and because the free stream wind in homogeneous terrain is expected to vary less in the horizontal than in the vertical direction.

5.2.4 Wake Characterization

For each 3D scan, the wakes are sampled at discrete distances downstream of the turbine and characterized regarding their center, height, width, orientation and *vd* statistics. A schematic of the quantities evaluated is given in Fig. 5.5 for the coordinate system adopted. The wake area identification is described in Section 5.2.3. The wake center is given as the center of gravity of the *vd* distribution

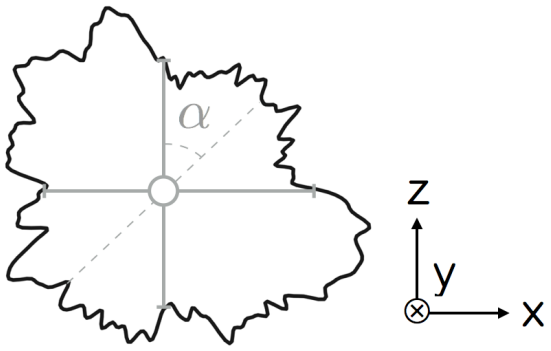

Figure 5.5: Schematic of the metrics used to characterize wakes: center (circle), width (horizontal gray solid line), height (vertical gray solid line) and orientation (clockwise angle from vertical α) for a coordinate system looking downstream in y for a wake in the xz-plane.

within the wake area [118, 35]. The height and width are the distances from edge to edge of the wake in the vertical and horizontal directions, through the wake center. The orientation is estimated by defining an ellipse with the same second-order moments as the wake shape and calculating the angle between its major axis and the vertical axis in the clockwise direction looking downstream. The yaw error is assumed to be negligible and is justified by limiting the difference between the nacelle position and the LiDAR-estimated wind direction to 15°in the field measurements (see Section 5.2.1).

5.3 Results

5.3.1 Difference between Scan, Mean and Snapshot

This subsection quantifies how the wind speed retrieved from each scanned value ($\mathring{U}_L$) compares to both the mean ($\overline{U}_L$) and instantaneous (U_L) values for the synthetic scans obtained from an LES. This serves as an estimate of the level of

uncertainty when large volumes of wind turbine wake data probed by a pulsed scanning LiDAR are assumed to be representative of mean or instantaneous conditions.

For each 12-min stack of sector scans obtained in the field, three spatially-equivalent synthetic scans are obtained from LES data by resampling the same 12-min LES time series according to the wind direction offset $\Delta\beta$ for $\mathring{U}_L$, $\overline{U}_L$ and U_L. The LES planes are stored at a 1-Hz frequency. To obtain the mean wind speed $\overline{U}_L$, each point in a xz-plane is sampled every second for the duration of the scan and then averaged over time. The instantaneous fields refer to snapshots at the first second of the scan. The comparisons here focus on the wind speed and are evaluated separately for each 3D scan. First, the mean pointwise difference in each xz-plane is quantified by the normalized root-mean-squared (rms) differences:

$$\Delta_{rms} = \left\{ \frac{1}{N} \sum \left[\frac{\left(\mathring{U}_L - U_{ref} \right)}{\mathring{U}_L} \times 100 \right]^2 \right\}^{1/2} \tag{5.8}$$

where $\mathring{U}_L$ are the temporally-disjunct points sampled by the instrument in the LES, U_{ref} either the mean or the instantaneous value at the same point (also from the LES) and N the total number of points in the xz-plane, which varies as a function of $\Delta\beta$. After obtaining one Δ_{rms} value for each downstream distance within each 3D scan, these values are averaged over time to give an overall measure of the differences. The results are given in Table 5.1 and indicate that the temporally-disjunct synthetic scan deviates from both the mean and the instantaneous values by similar magnitudes, but is closer (within 10%) to the mean. This is a reasonable result because measurements are collected along a single beam at a time, so to obtain better agreement between instantaneous and mea-

sured values, one would need to perform the analysis along the laser beam or in the downstream direction, instead of cross-stream, as is the case of interest. Overall, the differences decrease with downstream distance as the wake recovers, and the variability in the wind field decreases. These results indicate that a high density of scanned points (found exclusively closer to the turbine, as shown in Fig. 5.4) is not required to investigate mean wind turbine wake characteristics.

Table 5.1: Normalized rms differences Δ_{rms} (%) between synthetic scan wind speeds $\mathring{U}_L$, the instantaneous values at the first second of the scan U_L and the mean over the time it takes to complete the scan $\overline{U}_L$. Averages are over 80 3D scans, chosen to mimic the observations.

	3 D	**4 D**	**5 D**	**6 D**	**7 D**	**8 D**
$\mathring{U}_L$ and U_L	13.2	13.2	13.5	12.3	11.5	9.9
$\mathring{U}_L$ and $\overline{U}_L$	9.9	9.7	8.5	8.7	8.0	7.6

It is also important to assess how the spatial variation in the retrieved wind speeds compares to the one seen in the mean and instantaneous fields. This was done in two ways; first, by calculating the turbulence intensity ($TI = \sigma/\overline{U}$ where σ is the standard deviation and $\overline{U}$ the mean) for each downstream plane in each stack. The temporal mean of the TI values is close to ~20% for all distances downstream regardless of whether the scan, mean or instantaneous fields are considered, indicating that overall, the instrument scan time does not compromise the spatial variability retrieved in the wind speed measurements. This can further be examined by considering the wind speed profiles in the vertical (Fig. 5.6a) and horizontal (Fig. 5.6b) directions from the mean and instantaneous LES values and from the synthetic scans. In this case, the mean and instantaneous profiles are obtained by using the LES xz-planes without limiting the data to the points that a particular scan would sample at some $\Delta\beta$. The scan profiles

at each distance downstream are obtained by linearly interpolating between the synthetically-scanned points onto a line passing through the turbine hub in either direction and then calculating the temporal mean and standard deviation of all such profiles. Because the scanning geometry considered has a wider coverage in the azimuthal direction than in the vertical, the $\mathring{U}_L$ profiles in Fig. 5.6b are complete between $x = \pm 1$ D, while the vertical profiles in Fig. 5.6a sample the entire rotor plane (between $z = \pm 0.5$ D) from 4 D–7 D. The profiles in Fig. 5.6 are given in $\mathrm{m \cdot s^{-1}}$ to focus on the synthetic instrument ability to reconstruct the velocity field regardless of the method used to estimate the free stream and therefore derive the *vd*, which is a diagnostic variable. The analysis indicates that the reconstructed profiles follow the mean profiles closely, reproduce the double Gaussian in the near wake and capture the wake recovery. Note that our analysis isolates the effect of disjunct-in-time data. In reality, the line-of-sight averaging of the measurements constitute an additional source of error that likely smooths steep gradients in the observations, as has been found for vertical profiling LiDARs [39], but has not yet been quantified for scanning LiDARs.

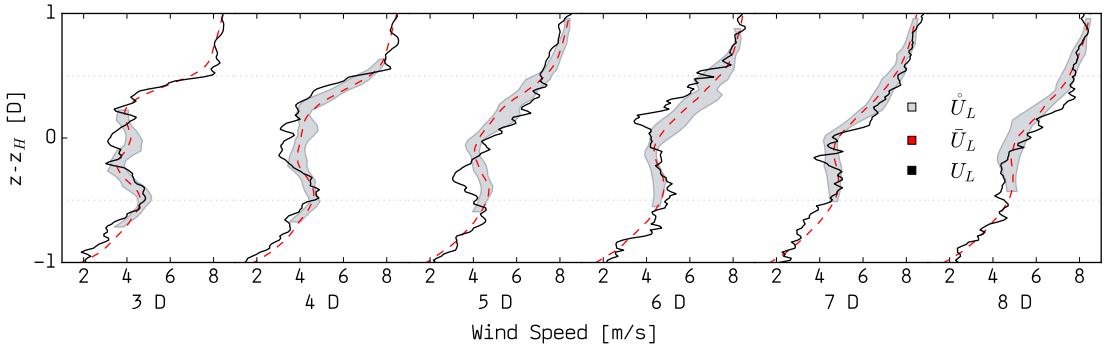

(**a**)

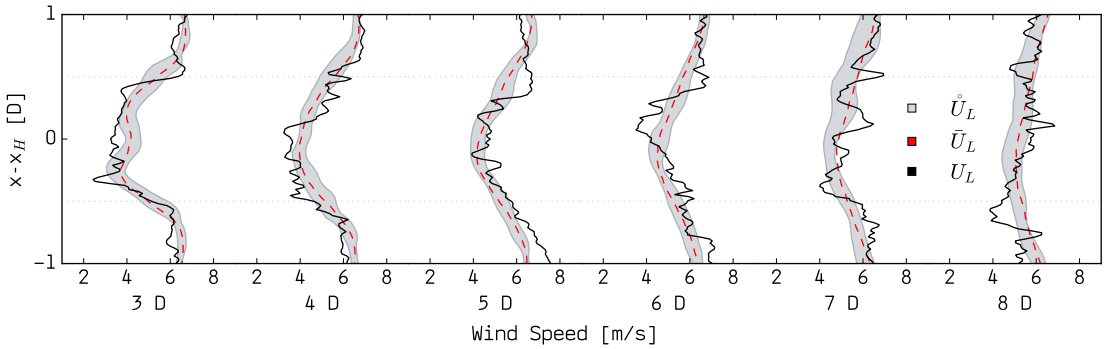

(**b**)

Figure 5.6: Mean wind speed profiles $\overline{U}_L$ (dashed red) from the large-eddy simulation (LES) over the time it takes to complete a full scan, instantaneous profiles U_L (solid black) at the first second of the scan and synthetic scan profiles given as mean ± one standard deviation (shaded gray). (**a**) Vertical profiles; (**b**) horizontal profiles.

5.3.2 Difference between Wake Characteristics from Scan, Mean and Snapshot

As previously mentioned, the ultimate objective of this work is to use the temporally-disjunct radial velocity retrievals to characterize the 12-min mean wake in the field scans. Before that is done, this section presents an estimate of the uncertainty level in wake characterization for the given scanning geometry and wake characterization metrics. The LES wakes are identified and character-

ized three times: using synthetic scans with temporally-disjunct, instantaneous and 12-min mean data points. A comparison between these three gives a valuable first indication of the uncertainty level in the synthetic scan that mimics the field data, while keeping in mind that the magnitudes may differ under different turbulence intensities and atmospheric stability conditions [97].

The 80 3D synthetic scans considered in this analysis are equivalent to those remaining in the observational dataset after quality control. They differ only in wind direction, and the same 12-min time series of LES data is resampled each time that a new scan begins, to account for the dynamic wind direction offset $\Delta\beta$. As mentioned in Section 5.2.3, it is necessary to define a free stream profile in order to characterize the wake. Planes that are not wide enough to provide such an estimate are not included in the analysis when downstream data are used to estimate free stream conditions. In total, 61 3D scans are left when $U_\infty \approx U_{\infty,down}$ and 69 when $U_\infty \approx U_{\infty,up}$.

For each stack, the wake is identified and characterized according to the sampled ($\mathring{U}_L$, U_L and $\overline{U}_L$) values following the description in Sections 5.2.3 and 5.2.4. The uncertainty in these metrics is quantified by absolute differences $|\Delta| = \left|\mathring{x} - x_{ref}\right|$, where $\mathring{x}$ are the metrics derived from the temporally-disjunct synthetically-scanned points and x_{ref} the wake metrics from the temporal mean or the instantaneous scans. For width, height and the *vd* statistics, these differences are normalized relative to the scanned value $\mathring{x}$. For the wake center, they are not normalized and are instead given as a vector sum of the differences in both the horizontal and vertical directions in units of D. For wake orientation, absolute differences are given in units of degrees.

An illustrative example of the uncertainty in wake characterization is de-

scribed here for the case shown in Fig. 5.7. In this example, the lowest SGC is ~47% at a downwind distance of 3 D and the highest ~74% at 7 D. The lowest SGD is ~9% at 8 D and the highest ~55% at 3 D. This pattern is typical for a LiDAR operated at the turbine base since a very high elevation angle would be needed to capture the near wake across the entire rotor. The mean wake center location for this 3D scan is well characterized by the $\mathring{U}_L$ values, with the smallest $|\Delta|$ (i.e., difference between the location identified using the 12-min mean LES output and that conditionally sampled to mimic the LiDAR) being ~0.05 D at 8 D. The maximum wake center $|\Delta|$ is ~0.2 D in the near wake (at 3 D) where the SGC is low and a large area of the wake is not covered. As illustrated in Fig. 5.7, these errors are within the differences between the instantaneous and mean wake center. The wake width was also reasonably estimated for the slices with higher coverage and density, with $|\Delta|$ below ~12% except at 7 and 8 D, where the wake area estimated from the LES synthetic scans greatly exceeds that from the full LES output. Because the scanning geometry is less restricted in azimuth than in elevation angles, the limitations in coverage are reflected in the vertical distribution of points and affect the estimates of wake height for which the errors ranged between 7% and 52% for the example in Fig. 5.7. Because of the approximate symmetry of the 12-min mean wake about its center, SGD is more important than SGC when attempting to estimate the statistics of the vd distribution. The differences for mean vd increased with downstream distance, but no clear conclusion can be drawn from the standard deviation of the vd. The linearly-interpolated slices also gave a good estimate of the wake orientation for this case, with $|\Delta|$ lower than 5° except at 3 D, where the wake area itself is not well approximated.

Analyzing a single case provides intuition into the magnitudes of differences

in each of the wake metrics considered. However, to obtain an overall understanding of the uncertainties, it is useful to consider the ensemble mean of the error values in the synthetic scans, which are shown in Fig. 5.8 relative to the mean and instantaneous fields using the two methods of estimating the free stream profile as described in Section 5.2.3. First, consider the difference between the metrics obtained from the temporally-disjunct points and from the mean fields (Fig. 5.8, black markers). For wake center, orientation and height, the largest errors are seen at 3 D where the area of interest (centered at the hub) is only partially covered by the scanning geometry. As for the example above, the wake center and orientation errors are small for the other downstream distances. This is similar to findings from previous work that evaluated the errors resulting from assumptions made while processing wake measurements from profiling LiDARs [39]. The wake height is poorly estimated all throughout, likely due to shortcomings in the definition of wake height and the method used to estimate it, which is very sensitive to differences in the wake orientation. As expected, errors in the *vd* mean and standard deviation are inversely proportional to the density of retrieved points, and therefore, the lowest error values are seen from 3–6 D. It is also evident from Fig. 5.8 that in some cases, the results are very sensitive to the method used to estimate the free stream, emphasizing the importance of including periodic free stream measurements in the scanning geometry when seeking to characterize wakes in field experiments. Finally, Fig. 5.8 also shows that the synthetic scan wake metrics are closer to the mean than to the instantaneous estimates, which was also seen for the pointwise analysis performed in Section 5.3.1.

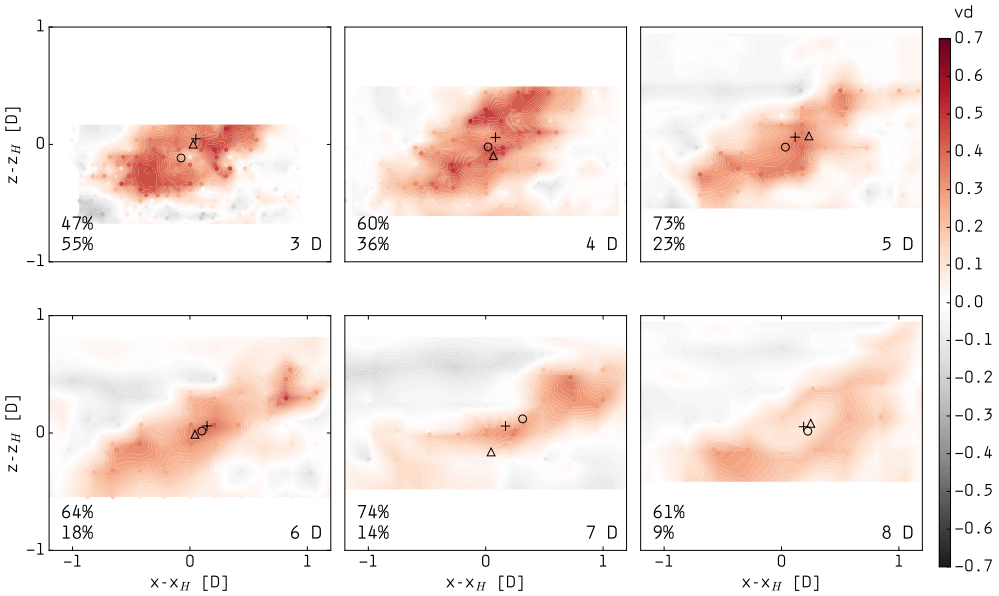

Figure 5.7: Velocity deficit for a synthetic 3D scan (shaded dots) and linear interpolation onto a regular grid (shaded contours) in the vertical (z) and cross-stream (x) directions at discrete distances downstream of the turbine from 3 D–8 D. Wake center from 12-min mean fields (+), from instantaneous fields at the first second of the scan (△) and from synthetic scan points (○). Free stream is estimated from downstream data. The wind direction offset for this scan is $\Delta\beta \sim 7°$. Percent values given in each frame are SGC (top) and SGD (bottom) in (%).

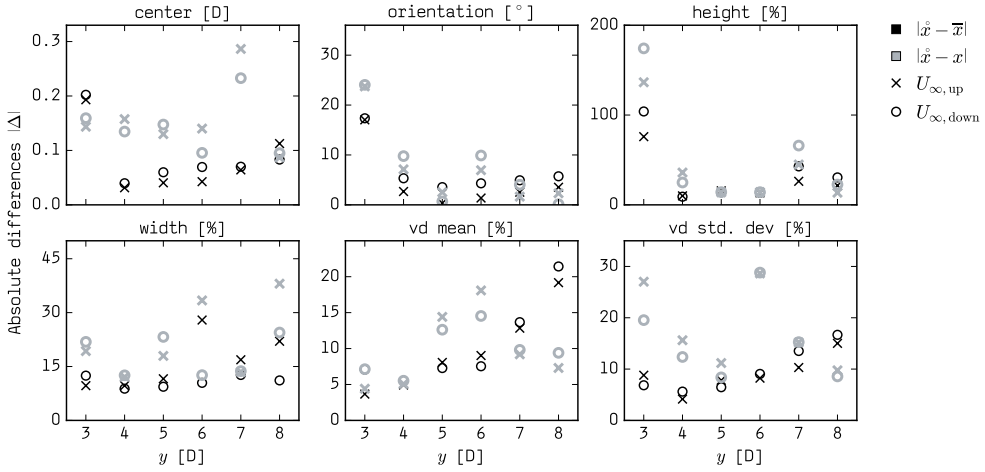

Figure 5.8: Absolute differences |Δ| in wake metrics for the LES synthetic scans (derived using the disjunct sampling equivalent to field measurements) relative to the metrics derived using the 12-min mean LES dataset (black) and the instantaneous fields from LES at the first second of the scan (gray). The different symbols refer to the free stream profile $U_\infty(z)$ used to derive *vd* and characterize the virtual scan wakes as described in the text. Variables and units of absolute difference are given for each subplot. For all subplots, the horizontal axis is the distance downstream of the turbine.

5.3.3 Field Wakes' Characterization

After testing the metrics on synthetic scans, they can be used to identify and characterize wind turbine wakes in field measurements. An example of *xz*-planes from measurements is given in Fig. 5.9, where $\Delta\beta$ is the same as in the LES wakes of Fig. 5.7. Note that despite representing the same scan, there is a small discrepancy in the coverage and density indices between the field wakes and the synthetic wakes, which arises from the limited extent in the LES data planes. It is evident and expected that the field measurements exhibit a higher level of complexity than the LES. Some of the reasons include: the effect of roughness, terrain and obstacles; the small-scale turbulent structures that result from the interaction of the flow with the rotor and tower; the intricacies of

ambient atmospheric conditions where a complex interplay of stability and surface characteristics act to modify the flow; random errors from the instrument and wind speed retrieval algorithms; and assumptions inherent in the method and described in Section 5.2.

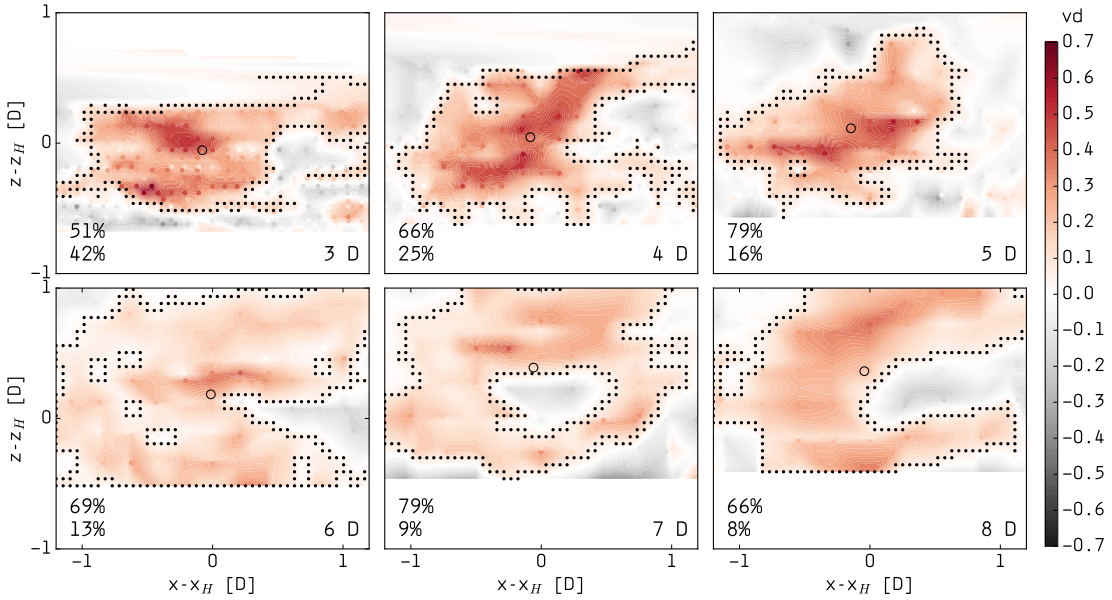

Figure 5.9: Velocity deficit for a 3D scan from field measurements (shaded dots) and linear interpolation onto a regular grid (shaded contours) in the vertical (z) and cross-stream (x) directions at discrete distances downstream of the turbine from 3 D–8 D. Wake shape (black dots) and center (circle). Wind direction offset for this scan is $\Delta\beta \sim 7°$. Percent values given in each frame are SGC (top) and SGD (bottom) in (%).

Keeping in mind the uncertainty levels estimated in Section 5.3.2 and the added complexity of the field measurements, the temporal means of wake metrics considering 59 3D scans in the 22-h period considered are given in Table 5.2. As previously determined (Section 5.3.2), it is possible to use these data to get robust estimates of the wake area and center for distances where there is reasonable wake coverage and density. For the current scanning geometry, this translates to downstream distances between 4 and 7 D. These methods can therefore be used to estimate the mean wake trajectory driven by changes in wind direc-

tion that happen over the LiDAR sampling time. Estimates of the wake center movement are shown in Fig. 5.10 for the period when enough measurements are available for this range of distances. Here, the mean wake trajectory refers to motion of the wake center in the time scale of the scanning duration (~12 min here) and is analogous to large-scale wake meandering. With the exception of a few cases, the estimates are stable across all downstream distances. The vertical trajectory is mostly positive and <0.5 D, indicating a wake centered above the turbine hub, consistent with streamline analysis of flow over the escarpment [34, 147] and with the upward wake deflection often resulting from tilt-up of the rotor shaft found in previous studies [146, 125]. Its magnitude tends to increase with downstream distance from the turbine. Conversely, the magnitudes of the wake center motion in the horizontal direction are similar throughout the distances considered (but not over time) and reach magnitudes of up to ~0.8 D. The values are predominantly negative indicating a wake center that is on average to the left of the hub when looking downstream along the streamwise (y) coordinate. This consistent wake deflection could be a systematic bias in the method resulting from neglecting veer across the rotor, which in some conditions (especially under stable stratification [148]) has been shown to be an important parameter resulting in wake steering and wake skew. The outliers in Fig. 5.10 do not represent a particularly large value of $\Delta\beta$ nor very low coverage and density. It is therefore likely related to the assumptions made to retrieve the horizontal wind speeds, which must be considered carefully in less stable situations where the vertical velocity component cannot be neglected.

Table 5.2: Mean wake characteristics obtained from the field measurements and including 59 3D scans. The wake center is given as a vector in the cross-stream ($\hat{x}$) and vertical directions ($\hat{z}$) for a coordinate system centered at the turbine hub.

	Unit	3 D	4 D	5 D	6 D	7 D	8 D
center	D$\hat{x}$, D$\hat{z}$	0.13, 0.08	0.18, 0.12	0.16, 0.16	0.15, 0.20	0.10, 0.25	0.08, 0.18
orientation	°	15	4	15	16	25	6
height	D	0.8	1.0	1.0	1.0	1.0	0.9
width	D	1.5	1.4	1.3	1.5	1.4	1.6
vd mean	-	0.22	0.19	0.15	0.13	0.12	0.11
vd SD	-	0.11	0.10	0.08	0.07	0.06	0.06

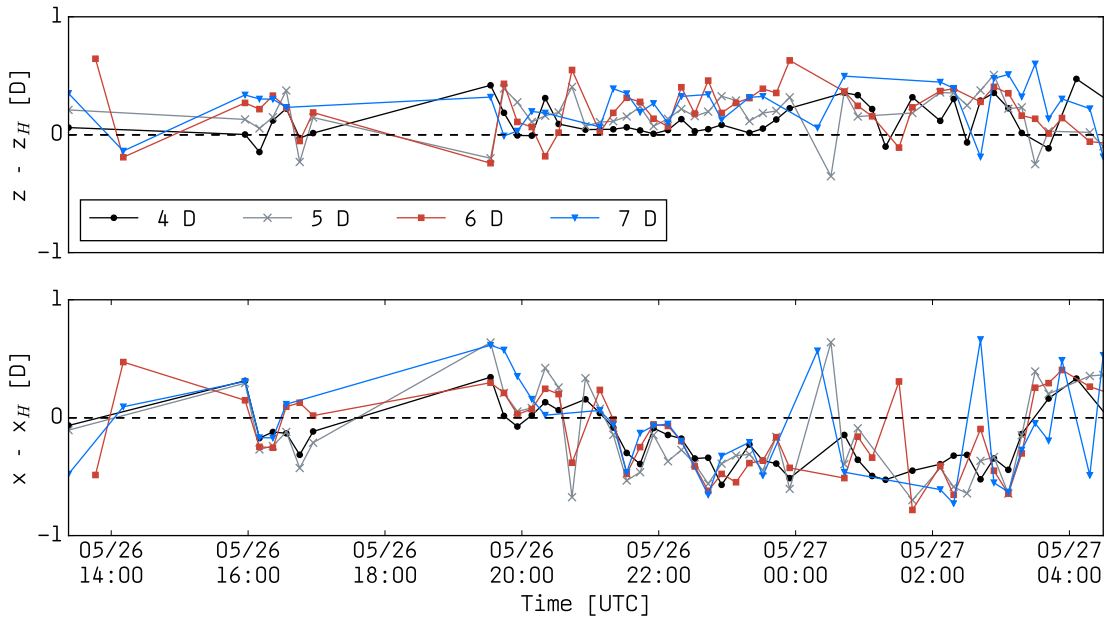

Figure 5.10: Time series of wake center position in the vertical (top) and horizontal (bottom) directions as estimated from the field measurements, for the intermediate downstream distances between 4 and 7 D. The dashed line marks the hub position (x_H,z_H) = (0,0).

As seen with the LES data, the wake width and height are more difficult to estimate, and the values obtained from field measurements do not indicate clear wake expansion with downstream distance (Table 5.2), possibly due to small expansion under stable stratification. Robust estimates of length scales

and wake orientation rely on both the coverage and density of points in the sampled transects, which is difficult to obtain for several downstream distances with a single ground-based LiDAR. If these metrics are of primary interest, these considerations must be taken into account when designing the scanning geometry for an experiment. The estimates of *vd* statistics clearly show wake recovery away from the turbine. The mean values are given in Fig. 5.11 and follow the similarity prediction at infinite Reynolds numbers where $vd \propto y^{-2/3}$ [149] despite the large variation in the 22-h period considered (as quantified by the standard deviation and shown in Fig. 5.11). The theoretical curve prefactor in Fig. 5.11 was obtained by fitting the expected power law to the data and is slightly lower than the value estimated in [146] when considering several previously-published studies of wake recovery. This difference is likely due to the short period considered, where atmospheric conditions are predominantly stable [34]. The standard deviation values, which represent the spatial variation of the *vd* in the *xz*-planes also match the expected results and decrease as the wake recovers (Table 5.2).

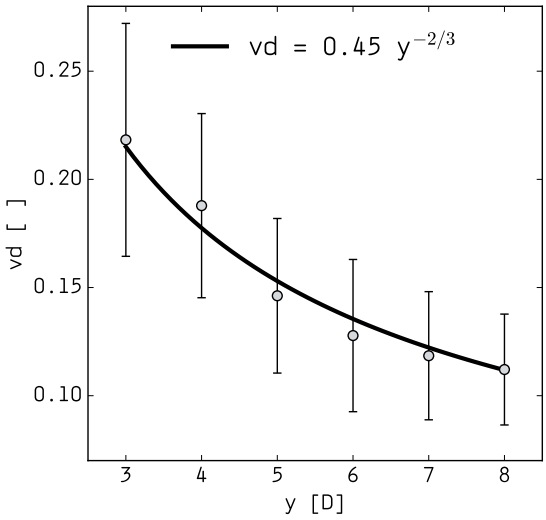

Figure 5.11: Temporal mean (markers) and standard deviation (whiskers) of the spatially-averaged velocity deficit (*vd*) estimated from field measurements. Considering 59 3D scans in the 22-h period. Similarity prediction given by the solid black line.

5.4 Conclusions

The objectives of this work are multi-fold: first, to estimate the difference between spatially- and temporally-disjunct wind speed measurements sampled by a ground-based pulsed LiDAR, an instantaneous snapshot of the flow and the temporal means over the time it takes to complete the 3D scan; second, to quantify how these differences affect wake characterization; finally, to apply wake characterization metrics [35] to LiDAR measurements. To our knowledge, this is the first work to provide a quantitative estimate of the uncertainty arising from these temporal limitations inherent in LiDAR measurements when large atmospheric volumes are probed. A simulated scanning LiDAR within an LES is used as the basis for this analysis, and we additionally provide a detailed methodology to derive cross-stream planes of wind turbine wakes at several

distances downstream from a stack of sector scans.

All of the analyses are based on transverse-vertical planes of horizontal wind at discrete distances downstream of a turbine and under single-wake conditions. Based on LES output, we determine that wind speeds sampled with the synthetic LiDAR are within ~10% of the actual mean values and that the disjunct nature of the scan does not compromise the spatial variation of wind speed within the planes. The sampled points deviate more from the instantaneous values closer to the turbine, with rms differences ~13% when averaged over 80 sector scan stacks. Based on the LES synthetic scans, we show the scanning geometry coverage is very important to characterization of the wake center, orientation and length scales. Because of the radial symmetry in the mean *vd* field, ample coverage of points is not required to obtain good estimates of the *vd* mean and standard deviation for which scanning geometry density is more important.

When the wake characterization metrics are applied to 59 3D scans obtained with a pulsed scanning LiDAR during a field experiment, the methods produce a consistent estimate of the wake center starting at 4 D, and the estimates for vertical and horizontal wake trajectory are robust between 4 and 7 D. Due to the scanning geometry limitations for this experiment, the wake length scales (i.e., width and height) are not well diagnosed and do not show a clear expansion with downstream distance. The characterization metrics can be applied to estimate the mean and standard deviation of the *vd* and, therefore, to quantify wake recovery. The consideration of the proposed indices to quantify scanning geometry density and coverage is recommended when planning a measurement campaign with a scanning LiDAR with the objective of characterizing wind tur-

bine wakes. Limiting the number of range gates and ensuring a good coverage of points in the vertical and horizontal directions is important to estimate wake length scales. Alternatively, higher density retrievals are necessary to estimate *vd* statistics. When focusing on the wake center, a compromise between coverage and density can be reached, and measurements can be made at a higher temporal frequency with a lower number of retrieved points. Finally, we recommend including periodic free stream measurements in the scanning geometry in order to minimize the uncertainty in *vd* quantification.

CHAPTER 6

ANALYSIS OF DIFFERENT GRAY ZONE TREATMENTS IN WRF-LES REAL CASE SIMULATIONS

6.1 Introduction

Recent advances in computational resources and atmospheric models have been driving the wind energy research community away from the Reynolds-Averaged Navier Stokes (RANS) approach, which does not permit a study of turbulence at the high Reynolds numbers that characterize flow within wind farms. Instead, research is increasingly based on Large-Eddy Simulations (LES) in which the horizontal grid size (Δ_{xy}) is reduced to a point where Navier Stokes can be assumed to resolve all of the turbulence scales relevant to the problem at hand [102].

Due to their relatively high computational cost compared to RANS-based codes, LES have traditionally been used to examine ideal cases where a large number of assumptions simplify the problem sufficiently for computational tractability and physical understanding (e.g., [150, 44]). Thus far, real case (i.e., non-idealized) LES focusing on atmospheric phenomena at scales $O\left(10^2 - 10^1\right)$ m have typically employed models that run un-coupled from the larger (meso and macro) scales (e.g., [151]) and for a time period on the order of hours (e.g., [152]) to days (e.g., [153]).

Recently, advances in computational resources have started to allow for coupling between meso and micro scale (i.e., LES-scale) models, and therefore for LES of the atmosphere under real-world scenarios. As a consequence, two

important questions have emerged. Firstly, how best to prescribe initial and boundary conditions to the LES and whether to allow feedback between the scales. Secondly, how best to treat the transition from meso to micro scales within numerical models [45]. The concept of "gray zone" (GZ) resolutions (i.e., $O(10^2 - 10^3)$ m) or "terra incognita" was coined to describe the spatial scales at which NS is able to resolve a significant fraction of the kinetic energy in the atmospheric boundary layer (ABL), while still needing to model the remaining part with physical parameterizations [54], which are mathematical formulations derived from empirical data or from simplifications in theoretical concepts and included in global and mesoscale numerical models to account for SGS processes [56]. In other words, the GZ lies in between two extremes: the fully parameterized meso scale and the non-parameterized micro scale.

A lot of the recent work in meso-micro scale coupling has focused on the Weather Research and Forecasting (WRF) model [154], which is a widely used framework for idealized and real case mesoscale atmospheric simulations that can be run in LES mode by scaling Δ_{xy} down to the micro scale (i.e., $O(10^2 - 10^1)$ m) and switching off several parameterizations. For example, [155] and [156] used ideal WRF-LES as benchmarks and developed scale-aware capabilities within existing ABL parameterizations (ABLP) to regulate their role at GZ resolutions. So far, these and other ABLPs expanded to accommodate GZ resolutions are limited to convective boundary layers (CBLs) and have mostly been verified against reference idealized LES (e.g., [157, 156, 158, 159]).

Very little work has been done to understand the behavior of ABLPs at GZ resolutions under real case LES. [160] applied aircraft observations to evaluate simulations of stratocumulus formation under the proposed scale-aware modi-

fications to the Met Office Unified Model, while nesting domains from 4 km to 100 m and considering a period of 2 days. They found that the performance of the scale-aware ABLP at the gray zone matched the performance of the well-established one-dimensional large-scale ABLP used for coarser grids, and that of the three-dimensional small-scale parameterization typically used for micro scale grid sizes. Another study by [155] proposed a scale-aware ABLP in WRF and verified it for real cases considering 24 hours of data focusing on the development of a convective roll at $\Delta_{xy} = 333$ m. They found that the newly proposed scheme enhanced the simulation of vertical motions under convective conditions but highlighted the need for further improvements which will cover a wider range of simulation scenarios. A more comprehensive study was performed by [150], where the effect of modifications to the GALES model was assessed by comparing one year of simulation data at $\Delta_{xy} = 100$ m to observations from a single meteorological mast. They found that the best agreement of simulations with observations occurred for ABL parameters that are explicitly resolved (i.e., instead of parameterized) thus further highlighting the need for long-term real case LES and for further research in meso-micro scale model coupling.

The research presented herein adds to this limited body of work by evaluating different approaches for treating GZ resolutions in full-physics LES of the atmosphere that are coupled to the mesoscale. While focusing on flow parameters of relevance to wind engineering, we quantify differences between three simulations in which the GZ is treated differently by being run with a well-established ABLP, its scale-aware version, and no ABLP at all (Section 6.4) and compare the simulation output to observational data collected during the Prince Edward Island Wind Energy Experiment [34] (Section 6.5). This specific loca-

tion was selected for our analysis because the terrain complexity and roughness changes warrant the use of LES. Moreover, the analysis considers a 15-day period which enables an assessment of the simulations performance under a wide range of atmospheric conditions.

6.2 Boundary Layer Treatment at the Gray Zone

Parameterized phenomena in mesoscale atmospheric models (such as WRF, when it is not run in LES mode) include radiative transfer, convection, and ABL physics. In ABLPs, a distinction is made between local vertical transport between adjacent grid levels and non-local vertical transport via strong updrafts that span the ABL depth [161]. Non-local ABL schemes such as the well-established YSU [162] include a non-local term in addition to the local transport. The SH scheme [155] is an expansion of YSU in which the amount of SGS vertical transport that needs to be parameterized is regulated based on Δ_{xy} and on the strength of the non-local transport itself.

All simulations presented herein use the YSU ABLP for domains with a grid resolution coarser than the GZ resolution, and are run in LES mode for the innermost domain in which is the grid resolution is finer than at the GZ. Hereinafter, the three simulations are referred to as YSU, SH, and LES (Table 6.1) based on how they handle the ABL physics at the GZ. In the LES simulation, the ABLP is switched off in the GZ domain and the SGS energy is modeled with a local closure in which a 1.5-order prognostic equation for turbulent kinetic energy (TKE) is used. This approach is recommended when the energy-containing eddies are significantly larger than the grid resolution [155] which is not neces-

sarily the case at the GZ. Therefore the GZ treatment in our LES simulation is physically-based, and can only be justified by the existence of a nested domain appropriately run in LES mode. The WRF source code was modified to enable meso-micro scale coupling based on the potential temperature perturbation method of [163, 164]. Previous work has shown that this modification results in an improvement to simulations of wind speed and turbulence intensity under different meteorological regimes and terrain complexities [165, 166].

Table 6.1: Treatment of atmospheric boundary layer physics at each simulation domain for the three simulations conducted in the experiment.

	Atmospheric Boundary Layer Parameterization (ABLP)		
Simulation Name	Mesoscale Domains Δ_{xy} = 9 km, 3 km, 1 km	Gray Zone Domain $\Delta_{xy} = \Delta_{GZ}$ = 333 m	Microscale Domain $\Delta_{xy} = \Delta_{\mu}$ = 111 m
YSU	YSU	YSU	None
SH	YSU	SH	None
LES	YSU	None	None

Because the differences between YSU and SH pertain to the strength of the vertical transport, we expect differences in vertical flow velocities and in vertical fluxes of heat and momentum between these two simulations. In idealized simulations, the system complexity is lower and significant differences between YSU and SH are only expected during convective conditions (i.e. strong nonlocal transport) while under neutral and stable stratification, SH should default to its underlying YSU structure. On the other hand, the higher level of complexity in a real case simulation precludes the predetermination of the exact effects that SH will have on the results. This complexity further highlights the demand for the present study in which these differences are investigated. Prior to the analysis, the only claim that can be made for the real case simulations conducted is that a distinction between YSU and SH is only expected during isolated peri-

ods throughout the simulation, when the effect of SH is modulated.

6.3 Data and Methods

6.3.1 Study Domain and Measurements

The simulations were conducted for a domain centered on the North Cape of Prince Edward Island for the period of the Prince Edward Island Wind Energy Experiment field campaign [34] at the Wind Energy Institute of Canada (May 2015). The narrow and flat island spans ~ 2 km across the measurement site (Fig. 6.1). To the west, a 10-14 m escarpment marks the transition from ocean to continent. An 80 m meteorological mast compliant with the International Electrotechnical Commission standards and equipped with 3D Gill Windmaster Pro sonic anemometers collected 10 Hz wind and temperature measurements at the heights (z) 20, 40, and 60 m above ground. The mast location is ~ 900 m (~ 400 m) from the coast in the North (West) direction.

The data from each sonic anemometer were subject to despiking, detrending and coordinate rotation when calculating variances and covariances. Data were further conditionally sampled to exclude wind directions associated with wind turbine wakes (unless otherwise noted in the analysis) and then used to compute streamwise, transverse, and vertical wind speeds, vertical fluxes of heat and momentum, and the Obukhov length. Conditions during the experimental period were dominated by onshore flow over the escarpment (SW-NW flow was observed 75% of hours) and the Obukhov length as computed from the sonic anemometers indicated unstable conditions on ~ 10% of hours, and stable

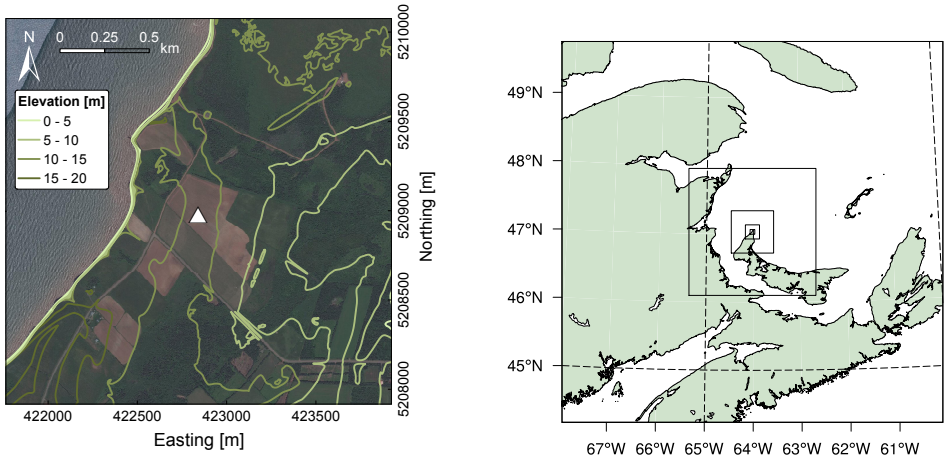

(a) Site satellite imagery and elevation.

(b) Simulation domains.

Figure 6.1: Measurement site terrain elevation and satellite imagery from Environmental Systems Research Institute (a). Simulation domains from Δ_{xy} = 9 km to Δ_{xy} = 111 m (b).

conditions on ~ 25 – 30% of hours [34].

6.3.2 Simulations

We performed three simulations using the Advanced Research WRF (ARW) core version 3.7.1 that differ only in their treatment of the GZ domain as described in Section 6.2. A total of five domains (with 70 x 70 grid points) were configured, centered at the meteorological mast location following a set of telescopic nests from 9 km to 111 m (Fig. 6.1b). Feedback between the scales is disabled so that the GZ fields can be analyzed without any influence from the turbulence that develops at the innermost domain which is run in LES mode across all simulations. Fifty vertical levels are distributed every ~ 10 m in the ABL, and stretched in the free atmosphere. Initial and boundary conditions for all domains are taken from the Climate Forecast System Reanalysis [167] at a spatial

resolution of ~ 38 km. Topography for the highest resolution domain is taken from the Shuttle Radar Topography Mission [168] at a 90 m spatial resolution, and land use from the GlobCover [169] at a ~300 m spatial resolution.

Analyses of model output focus on flow parameters in the ABL surface layer. The model was run for a 15-day period and time series were saved exclusively for the grid point closest to the meteorological mast location (Fig. 6.1a) for seven heights above ground between ~ 8 m and ~ 182 m. The model saves historic output with a temporal frequency of 4 Hz, which are immediately used to compute 10-minute averages diagnostics and subsequently deleted to release computational memory and minimize storage requirements.

6.3.3 Variables and notation

All analyses are performed for a fixed location (i.e., the meteorological mast) and consider vertical profiles of 10-minute mean quantities. Perturbations of a variable x are calculated by subtracting the 10-minute mean x from the 4 Hz instantaneous values x_i as the simulation output is produced, $x' = x_i - x$. When the 10-minute mean values are averaged over a longer time period (e.g., the 15 days of simulation) angled brackets are used, $\langle x \rangle$. We focus on flow variables of relevance to wind energy such as horizontal wind speed U, vertical wind speed w, wind direction β, vertical wind shear $\Delta U/\Delta z$, and turbulence intensity $I = \sigma_U/U$ where σ_U is the standard deviation of the horizontal wind speed U over a 10-minute period. I is only calculated for time stamps in which $U \geq 3$ m s^{-1}, to avoid exceedingly large values at wind speeds below a typical wind turbine cut-in. Additional turbulence characterization diagnostics are computed, such as

kinematic heat flux $\overline{w'\theta'}$ where θ is potential temperature, and turbulent kinetic energy $TKE = TKE_\Delta + TKE_{SGS}$. TKE_Δ represents the amount of TKE that is resolved by the model at a grid resolution Δ_{xy} including the ABLP budget, and TKE_{SGS} is the amount that is produced by the turbulence closure model when no ABLP is used and the simulation is run in LES mode. The SGS partition is output by the model directly, and the resolved partition is calculated as $TKE_\Delta = \frac{1}{2}\left(u'^2 + v'^2 + w'^2\right)$.

Differences arising from the model configurations used are discussed in Section 6.4 without reference to the measurements. Differences (δ) across the three simulations for a given variable x are denoted as $\delta_x = x_{\texttt{SIM}} - x_{\texttt{YSU}}$ where `SIM` is either SH or LES, and the reference simulation is YSU. Absolute differences are given as $|\delta_x|$. When dimensionless values are preferred, δ_x is normalized by $|x_{\texttt{YSU}}|$. Model performance relative to observations is quantified by $\varepsilon_x = x_{\texttt{SIM}} - x_{\texttt{OBS}}$ for a variable x and simulation `SIM` and is calculated for 10-minute mean values while linearly interpolating the model output to the measurement heights of 20, 40, and 60 m. Absolute errors are symbolized by $|\varepsilon_x|$ and temporal means $\langle\varepsilon_x\rangle$.

6.3.4 Spectral Analysis

We assess the ability of our simulations to correctly reproduce the spectrum of atmospheric variability using spectral methods that relate the energy content of the flow to the frequency (f) or wave number (κ) of the eddies [170]. As described in Section 6.3.3, the analysis of turbulence in terms of I and TKE considers 10-minute mean values computed from 4 Hz time series immediately after

running the simulations and before purging the large intermediate output files. The spectral analysis is instead based on the final output files and is performed for the time series of 10-minute mean horizontal wind speeds at a given height, for the fixed location being considered (i.e., the meteorological mast at the experiment site). To facilitate comparisons, the spectra are computed according to [171] for each day of observational data that is 100% complete and then averaged over all considered days.

6.4 Comparison of Model Simulations

6.4.1 Vertical and Horizontal Flow Components

Consistent with expectations (as discussed in Section 6.2), differences in the 10-minute mean vertical velocity δ_w exist intermittently between SH and YSU and have maximum magnitude of ~ 2 cm s^{-1} at the GZ scale (Fig. 6.2). Despite feedback being disabled between the domains, these differences still propagate to the innermost nest where δ_w is lower in magnitude but still non-zero at isolated periods in the time series. Vertical velocity differences between YSU and LES are larger and more consistent than between YSU and SH, and have a maximum magnitude of ~ 7 cm s^{-1} at the GZ scale. Because the differences between SH and YSU are intermittent, they are close to zero when averaged over time (Fig. 6.3). Conversely, there is a consistent difference between YSU and LES throughout the surface layer. LES produces larger wind speeds than YSU closer to the surface, and lower wind speeds above the nominal hub height of 80 m.

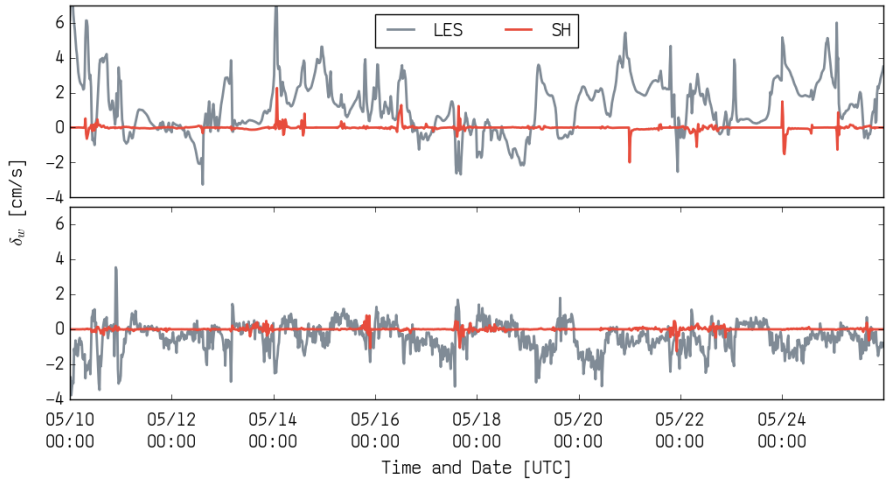

Figure 6.2: Differences between SH (red) and LES (gray) simulations of 10-minute mean vertical velocities δ_w [cm s^{-1}] relative to YSU. Values are for z = 8 m at GZ domain (top) and microscale domain (bottom). For readability, each two consecutive values are averaged and 20-minute means are given.

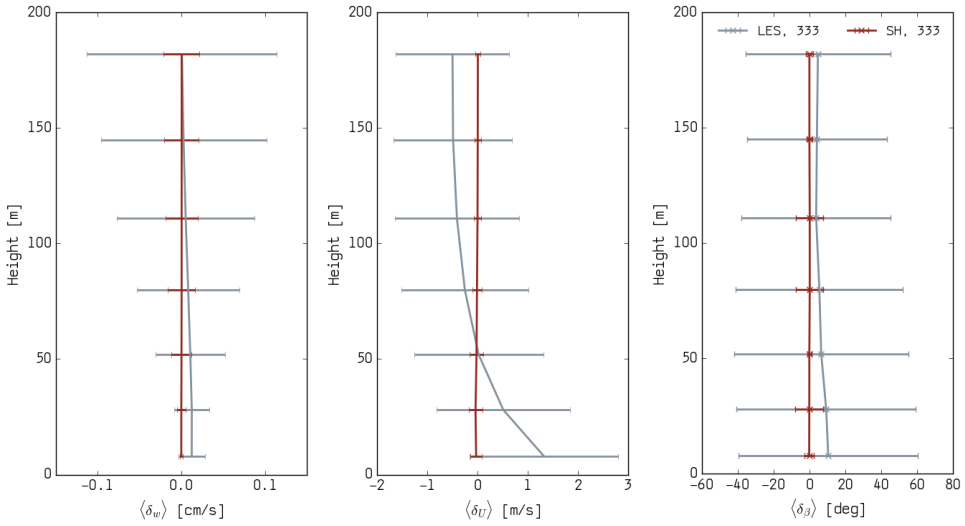

Figure 6.3: Temporal mean (± standard deviation) of differences between SH and YSU (red), and between LES and YSU (gray) simulations for vertical velocities w [cm s^{-1}] (left), horizontal wind speed U [m s^{-1}] (middle), and horizontal wind direction β [deg] (right) for the GZ domain.

6.4.2 Shear and Turbulence

The probability density function of 10-minute values of vertical wind shear ($\Delta U/\Delta z$) across a nominal turbine rotor plane (extending from 30-110 m) also differs between LES and the simulations in which the ABL is parameterized. At the GZ and microscale resolutions YSU and SH are almost indistinguishable (Fig. 6.4). However the difference between these simulations and LES is well pronounced especially at the GZ domain where the shear derived from the LES exhibits much smaller values (exclusively < 0.03 s^{-1}) than is evident in SH and YSU output.

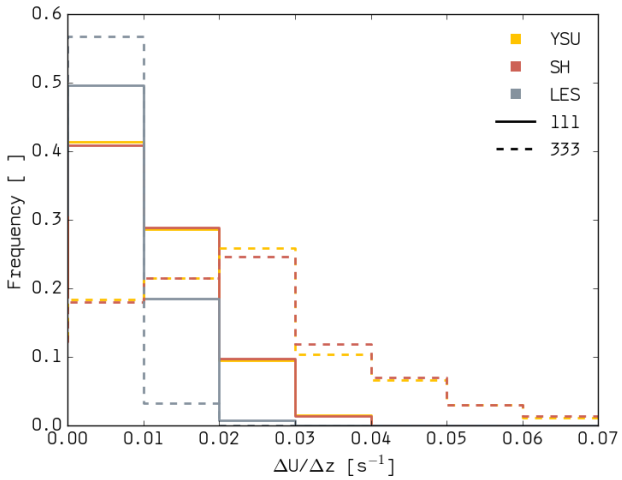

Figure 6.4: Probability density function for vertical wind shear $\Delta U/\Delta z$ [s^{-1}] between 28 and 111 m, considering the 15 days of simulation. Values shown for gray zone (dotted) and microscale (solid) domains.

Some understanding of the turbulence produced by the model can be obtained by considering TKE, which encodes information about vertical and horizontal velocity fluctuations. For the TKE analysis we focus on $z = 80$ m, a typical hub height for onshore wind turbines and the hub height of the turbine operated by WEICAN at the measurement site. We investigate how much the

treatment of the ABL physics at the GZ resolution affects the TKE budget within the innermost domain. Although the three simulations are run in LES mode at this scale, there are still clear differences between the LES simulation and the other two (Fig. 6.5). The LES simulation presents lower explicit and SGS TKE values (i.e., TKE_{Δ} and TKE_{SGS}) especially at lower wind speeds. Because lower wind speeds are often associated with larger eddies, it is reasonable to expect that the LES simulation would fail to reproduce some of that energy content. These differences are expected: at the GZ resolution, the use of a traditional parameterization is likely to lead to an over-production of turbulence since the part of the energy that the parameterization is supposed to generate is already naturally resolved at that scale. On the other hand, the gray zone resolution is still not fine enough to resolve in LES mode all scales of the energy that is relevant to wind plant aerodynamics.

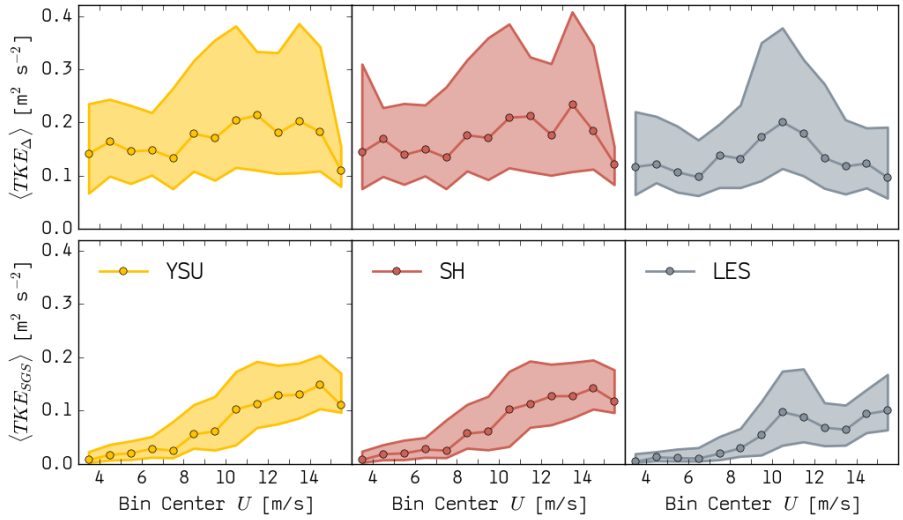

Figure 6.5: Resolved (top) and SGS (bottom) median TKE (markers) [m^2 s^{-2}] as a function of wind speed [m s^{-1}] discretized at 1 m s^{-1} in the microscale domain. Solid lines give 25th and 75th percentile values.

6.4.3 Energy Spectra

The results presented in this section are based on the spectral analysis methods described in Section 6.3.4. The spectral energy content for each simulation considering the entire 15-day time series is shown in Fig. 6.6. As expected, the energy at high frequencies decays quickly in the GZ domain for all simulations. At the innermost domain significantly more energy is seen at the spectral tails. It is also expected that in general, YSU and SH will produce more energy than LES because of the ABLP which is activated in the former two to produce energy at scales lower than the grid resolution. This is verified in Fig. 6.6, where the energy content is lower for LES at both scales, especially at the high frequency end of the spectra. The difference in energy content between LES and the other two simulations decreases at the innermost domain, where all simulations are run in LES mode. Despite this approaching of the results, the LES simulation still presents slightly lower energy than the other two simulations confirming that the GZ treatment significantly impacts the variance at the innermost domain even if feedback between the scales is disabled.

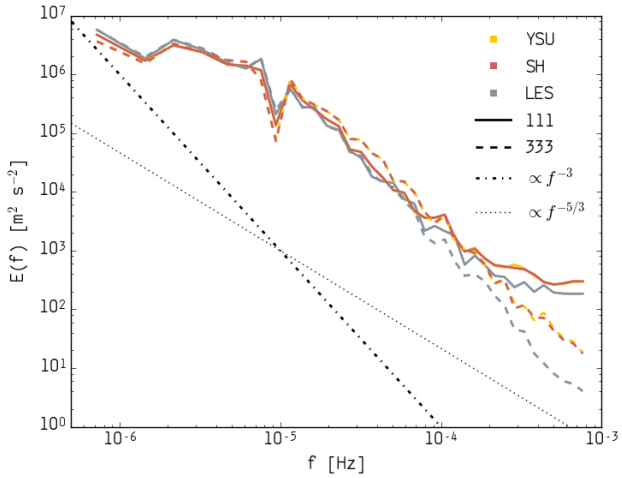

Figure 6.6: Energy spectra of the 15-day time series of 10-minute mean horizontal wind speeds at z = 80 m for the three simulations at the GZ and microscale domains. Black lines represent a decay $\propto f^{-5/3}$ and $\propto f^{-3}$.

6.5 Measurement comparisons

Thus far the simulations have been cross-compared without reference to the measurements, to illustrate the sensitivity of flow parameters to different GZ treatments in each simulation. In this section, we evaluate the output from the microscale domain relative to the observational data set described in Section 6.3.1.

6.5.1 Horizontal Wind Speed

Fig. 6.7 shows the distribution and magnitude of horizontal wind speed errors as a function of different atmospheric conditions in terms of wind speed, direction, and turbulence intensity. An obvious and important result from this analysis is that the YSU and SH error distribution is almost indistinguishable regard-

less of the atmospheric conditions considered, indicating that the differences between these two simulations discussed in Section 6.4 are lower in magnitude than the model error. The data distribution histogram shows that most of the observed wind speeds are between 2 and 14 m s^{-1}, and the averaged $\langle \varepsilon_U \rangle$ values show a general decrease with increasing wind speed. Although time stamps in which the meteorological mast was subjected to a wind turbine wake were filtered out, the model still largely over-estimated the wind speeds. There is no clear distinction between regimes in which different simulations performed better. For some bins, the median errors across simulations were the same while for others a distinction can be made between LES and the other two simulations.

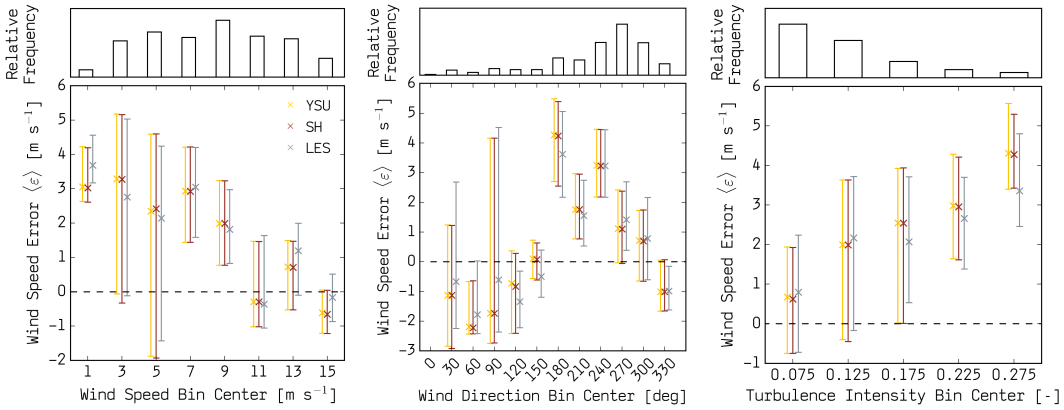

Figure 6.7: Time series of wind speed errors [m s^{-1}] at z = 60 m averaged over different measured atmospheric conditions at the same height: wind speed (left), wind direction (middle), and turbulence intensity (right). Circles represent the median error, and whiskers give 25^{th} and 75^{th} percentile values for each bin. Bars indicate how much of the total data considered fall into each bin. Dashed line marks zero error. Note the different vertical scales.

There is a systematic pattern of wind speed error distribution as a function of wind direction, across the three simulations. During the few cases of winds from the Northeastern to the Southeastern sectors ($\beta < 165°$) the model mostly underestimated the wind speed magnitude. Conversely, an over-estimation is seen for Westerly and Southwesterly winds ($165° \leq \beta < 315°$), which make up the major-

ity of the data set. In terms of differences between simulations, let us consider only the sectors with higher measurement density ($\beta > 135°$). We can see that LES performed slightly better for Southerly winds and the other two simulations for Westerly winds. This result may be related to the offshore footprint at lower measurement heights (e.g., $z = 20$ m) at this site as discussed in [34]. This would result in the development of an internal boundary layer brought on by changes in roughness and topography, and in enhanced turbulence levels as also pointed out in [34]. Both these consequences of offshore (Westerly) flow would lead to a reduced length scale in the flow structure, which would likely fail to be reproduced in a simulation where the ABL is not parameterized. This explains the higher error values for LES (when compared to YSU and SH) for Westerly flow.

In terms of turbulence intensity, a clear pattern can also be seen. Overall, the median wind speed error increases with turbulence intensity. Regarding the differences across simulations, the model errors are larger for LES at the low I bins ($I < 0.15$) and lower for LES at the high I bins ($0.15 \leq I < 0.25$). Note that the majority of the data lie within the first two I bins, leading to a temporal average of $\langle \varepsilon_U \rangle$ that is slightly higher for LES than for YSU and SH.

6.5.2 Shear and Turbulence

Fig. 6.8 shows the distribution of shear across the measurement layer ($z = 20$ m to 60 m) during the entire period for which measurements are available.The model using LES, SH, and YSU uniformly underestimates the shear, the abruptness of which will be underestimated in simulations conducted at the microscale

(Δ_{xy} = 111 m). As shown in [34] the precise description of this terrain feature had a profound impact on the flow response in the Ellipsys CFD model. The simulations SH and YSU exhibit similar probability distributions of vertical wind shear and both exhibit closer accord to the observed values than the LES output. This is due to the higher shear produced by these simulations at the GZ, as discussed in Section 6.4.2. This result indicates that the energy produced by the ABLP at the GZ is important to the simulation of vertical variations of wind speed in the surface layer, and that running a simulation in LES mode at the GZ could compromise the model results in the presence of high shear (e.g., under stable atmospheric conditions such as prevailed during the Prince Edward Island Wind Energy Experiment).

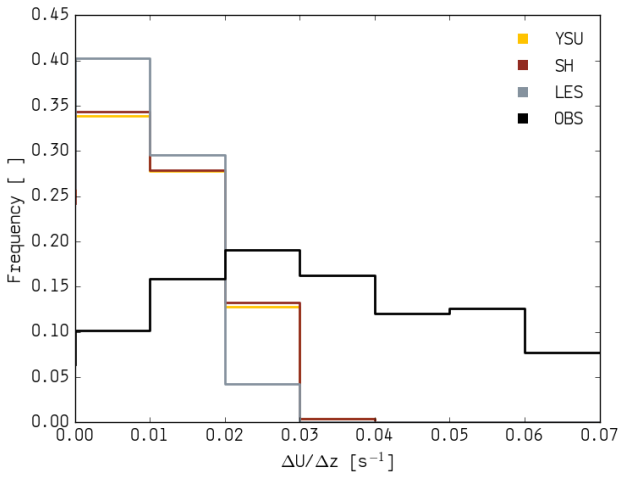

Figure 6.8: Histogram for vertical wind shear $\Delta U/\Delta z$ [s^{-1}] between 20 and 60 m, for all 10-minute periods for which coincident model output and observations are available.

As shown in Fig. 6.9 all simulations reproduced the approximate value of total TKE at low wind speeds, but fail to simulate the increase of TKE with wind speed magnitude present in the observations. The wide range of TKE values measured at $z \geq 40$ m was underestimated by all simulations. The difference be-

tween simulations is much smaller than the difference between the simulations and measurements, but overall the YSU and SH simulations produced binwise median values that are closer to the measurements than those produced by LES.

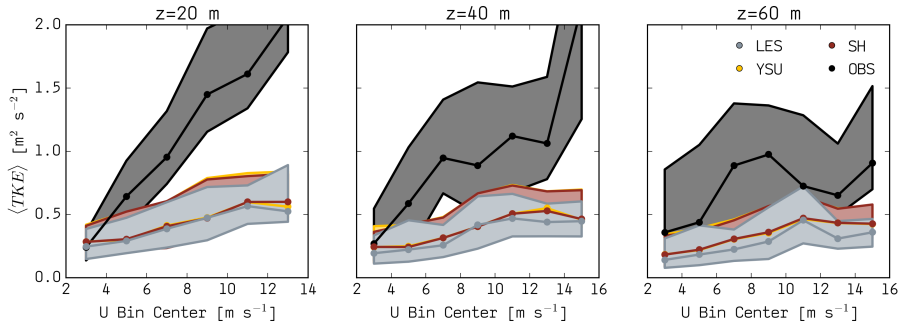

Figure 6.9: Median (markers) TKE [m^2 s^{-2}] as a function of wind speed (discretized in 2 m s^{-1} bins) for observations and simulations at z = 20 m (left), 40 m (middle), and 60 m (right). Vertical axes are identical. Solid lines and shading in between give 25th and 75th percentile values. Data included are observations (black), SH (red), LES (gray) and YSU (yellow).

Similarly to the horizontal wind speed profiles, different simulations perform best under different conditions in terms of kinematic heat flux. Regardless of the GZ treatment, the model struggles to reproduce the mean diurnal cycle of heat flux especially at z = 20 m (Fig. 6.10). The agreement improves above this height, where the measured flux is lower in magnitude and the model produces higher estimates. The diurnal cycle that seems to appear in the model data starting at z = 40 m captures the magnitude of negative and positive peaks in the observations but these peaks are shifted by $\sim$ 6 hours from the observed values. It is evident from the z = 60 m panel in Fig. 6.10 that there are discernible differences between the YSU and SH simulations both for negative and positive flux periods. Namely, in SH the magnitude of the mean flux is slightly lower than in YSU. The differences between these two simulations and LES are once again more pronounced, especially during the first half of the diurnal period at

z = 40 and 60 m.

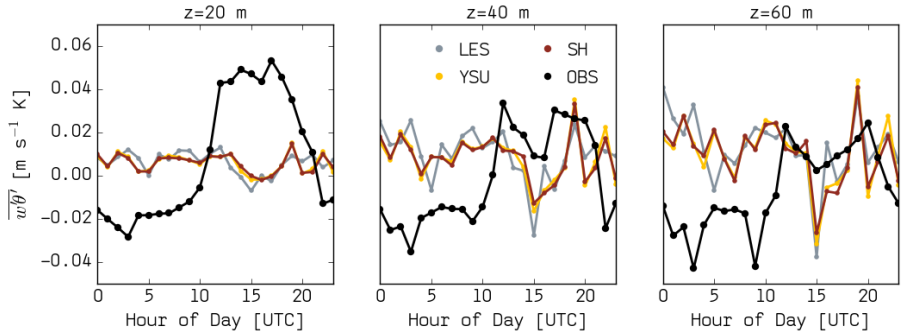

Figure 6.10: Mean diurnal cycle (local time is UTC-3 during experiment) of kinematic heat flux $\overline{w'\theta'}$ [m s^{-1} K]. The mean is computed from all 10-minute periods which simulations and measurements are available.

The kinematic heat flux error values $\varepsilon_{\overline{w'\theta'}}$ calculated for each 10-minute period from LES output is -0.5%, -5.7%, and 3.9% at z = 20, 40, and 60 m respectively, compared to -4.2%, -7.3%, and -14.5% for SH, which presents mean errors slightly larger than YSU. The difference in simulated $\overline{w'\theta'}$ between SH and YSU can be very large at specific time steps but over the entire period it is $\sim -3.4\%$ at 60 m. Note that in [44] a constant surface heat flux is used to examine the stability dependence on grid-size. Here, we reveal that in a full-physics simulation where surface forcings are unsteady, the scale-awareness of this ABLP can have the effect of decreasing the heat flux simulated by the model under a variety of atmospheric conditions.

6.5.3 Energy Spectra

Fig. 6.11 shows the spectral energy content in the 10-minute mean wind speeds at z = 60 m, obtained individually for each day in which the measurement data set was complete, and averaged across all of the complete days (a total

of 7). Once again, the difference between YSU and SH can hardly be discerned. The spectral interval characterized by the frequencies $f \in \left(6 \times 10^{-5}, 6 \times 10^{-4}\right)$ Hz (time scales between $\sim$ 5 hours and $\sim$ 30 minutes, respectively) reveals a clear and consistent underestimation of the energy content by all of the simulations, at all three heights. This portion of the spectrum likely characterizes the terra incognita described in Section 6.1. The analysis for this period and site suggest that running the GZ domain in LES mode produces better results in terms of variance of the streamwise velocity, especially at $z = 60$ m. All of the simulations captured well the decaying slope of $E \propto f^{-5/3}$ that is predicted for these frequencies.

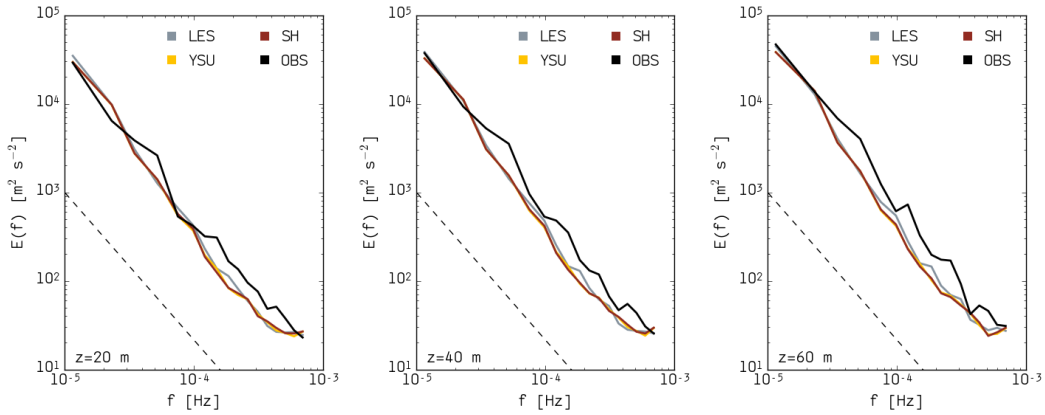

Figure 6.11: Energy spectra of horizontal wind speeds at $z = 20$ m (left), 40 m (middle) and 60 m (right) for observations (black), LES (gray), YSU (blue), and SH (red). Spectra consider all 10-minute mean time stamps in which measurements and simulations were available and an entire 24-hour period was complete. Spectra are obtained separately for each day then averaged across days. These data are not filtered for wind turbine wakes. Dashed black line represents a decay $\propto f^{-5/3}$.

6.6 Conclusions

Mesoscale-microscale coupling in atmospheric modeling is a very important topic for wind engineering research. This coupling is necessary for obtaining simulations of the ABL at higher resolutions and fidelity levels, which will in turn improve the accuracy of analyses in a variety of research areas such as resource assessment, wake characterization, and loads estimation. Coupling more than one models, or several domains within a single model is a multi-disciplinary task that faces numerical challenges, computational limitations, and shortcomings in our understanding of relevant physical processes.

Due to the ongoing advances in computational power, meso-microscale coupling for wind energy applications has recently become a topic of active research. We are currently moving away from the need to choose between (i) idealized simulations at high spatial and temporal resolutions or (ii) real case simulations limited to the mesoscale. In this study, we conduct a multi-day real case simulation of the atmosphere down to a spatial resolution of 111 m, and consider different ways of treating the GZ scales which characterize the transition from meso to micro. At this transition scale, a large portion of the kinetic energy is supposed to be naturally produced by the momentum balance equation in the model, while the remaining part still needs to be parameterized. Recent work in this field has proposed modifications to existing ABLPs producing scale-aware versions of the original. This scale awareness modulates the effect of the ABLP on the model solution depending on the grid size and the atmospheric conditions. We conducted three simulations that only differ in their treatment of the ABL in the GZ domain. One of them uses the traditional YSU parameterization, one uses its scale-aware version SH, and a final one uses

no parameterization at all and runs the GZ domain in LES mode.

The analysis focuses on 10-minute mean vertical profiles of parameters of relevance to wind engineering, such as horizontal wind speed and direction, vertical wind shear, turbulence, and energy spectra. We first compare the differences across simulations at the GZ domain in order to quantify the effect of the different GZ treatments on the simulated fields. Then we compare the simulations to observations collected with ultrasonic anemometers during the Prince Edward Island Wind Energy Experiment field campaign, and investigate which simulation presents the smallest errors.

We find that differences between YSU and SH can be negligible when multi-day temporal averages are considered, but that for shorter intervals these simulations can differ significantly not only at the GZ domain but also at the inner nest, which uses data from the GZ domain as boundary conditions. At the GZ, the LES simulation produces significantly lower shear than the other two simulations. Even though no feedback is allowed between the domains, the mean TKE values at the microscale nest are significantly different between LES and the other two simulations, with LES producing lower TKE estimates especially at low wind speeds. We find that including a microscale domain within the model chain leads to a recovery in the decaying tails of the spectral energy content at the GZ.

The comparison between simulations and observations focuses on the innermost domain, and therefore quantifies the effect of different GZ treatments on fields simulated by a finer resolution domain nested within the GZ. Most globally-averaged errors are similar across simulations, but are found to vary significantly for specific cases. In terms of U, LES performs better than YSU and

SH for southerly winds. For westerly winds the footprint of the measurements is likely offshore and the development of internal boundary layers is expected to lead to a reduction in the turbulence length scales, and therefore to an underperformance of LES relative to the other simulations. The majority of the observations reveal turbulence intensity < 0.15 during which YSU and SH present slightly lower U errors.

All simulations fail to reproduce the increase in TKE with U, and the wide range of TKE values within a wind speed bin for heights above 40 m. Very small differences are seen across simulations for TKE as a function of U. Due to the underestimation of shear in the LES simulation, YSU and SH perform slightly better in terms of the shear distribution values but all simulations still underestimate the shear magnitude across the layer from 20 to 60 m. All simulations fail to capture the diurnal cycle of turbulent heat flux, and largely underestimate the flux magnitudes close to the ground revealing a shortcoming not in the model or the ABLPs but rather in the boundary conditions prescribed. The presence of a GZ between time scales of 5 hours to 30 minutes is clearly seen in the model spectra, and the steamwise velocity variance for LES that matches the observations slightly closer.

Overall, we found that for multi-day simulations the present question is whether to run the GZ in LES mode or with a ABLP at all, and not whether to consider scale-aware parameterizations which are still in early development phases. For the period considered, very small differences were seen between YSU and its scale-aware version, SH. For shorter simulations, the differences between SH and YSU can be significant and the GZ treatment should be considered more carefully. With the current data set, we cannot yet determine

whether SH could result in a substantial improvement of the simulated fields under non-idealized simulations. We generally found that while running the GZ in LES mode may not be a physically-sound approach, it still produces a kinetic energy content and turbulent heat fluxes that more closely match the observations. Conversely, the other two simulations performed slightly better in terms of horizontal wind speed and vertical wind shear. Further work is needed to generalize the development of scale-aware parameterizations so that they may provide a solution for fully coupled, real case simulations of the ABL with realistic predictions for both shear and turbulence.

CHAPTER 7

EFFECT OF WIND TURBINE WAKES ON THE PERFORMANCE OF A REAL CASE WRF-LES SIMULATION

7.1 Introduction

Atmospheric phenomena across a wide range of spatial and temporal scales affect wind plant aerodynamics. Due to computational limitations, the majority of wind turbine wake analyses so far have relied on semi-idealized simulations where some physical processes are disregarded and a simplified version of a complex system is then simulated. For example, the widely used Dynamic Wake Meandering model (DWM, [48]) solves a steady-state approximation of the Navier-Stokes equations and then superimposes to the solution a turbulence field using stochastic methods and assuming a form for the energy spectrum [120]. On the other hand, the National Renewable Energy Laboratory Simulator for Wind Farm Applications (SOWFA, [112]) simulates unsteady velocity fields at a high resolution, but its computational requirements preclude the simultaneous inclusion of some relevant atmospheric phenomena (e.g., cloud physics) and limit the achievable simulation time to minutes instead of hours or days.

Ongoing advances in computational resources have only recently started to allow real case (i.e., non-idealized) numerical simulations of the atmosphere to be run at spatial resolutions on the order of a typical wind turbine (WT) rotor diameter. As a result, it has become imperative to consider the effect that individual WTs have on the flow and it has also become possible to use these high resolution simulations for wake analyses. Research in this field may be conducted using the Weather Research and Forecasting (WRF) model [154] which

considers the full physics of the atmosphere and can be nested down to the meso and micro scales, and even be run in Large-Eddy Simulation (LES) mode by switching off parameterizations for grid resolutions $\leq O(10^2)$ m. Parameterizations are simplified mathematical descriptions of processes based on a set of assumptions, and used to model quantities that are not resolved under a given grid resolution. Unlike SOWFA, WRF does not include an explicit WT model and the effect of WTs on the flow is instead added in the form of a drag parameterization. In other words, individual wind turbine wakes are not modeled.

The idea of a wind farm parameterization first appeared in the context of global models to investigate the large-scale effect of wind farms on the Earth's climate [173]. Later, their impact on the regional climate was also considered [174] and more recently, shorter-term simulations using WRF are also seeking to include a description of wind farm effects [175, 176]. The wind farm parameterization currently distributed with WRF was developed for horizontal grid sizes higher than five rotor diameters [177] and real case WRF-LES simulations at a higher spatial resolution cannot benefit from it. Research is needed to investigate how the effect of WTs on the flow can be best modeled when performing WRF-LES simulations.

As a first step in this direction, the current work seeks to determine how the absence of such a parameterization affects the model performance. This is done by quantifying the role of wakes in explaining the discrepancy between simulated and observed flow conditions. The analysis consists in comparing WRF simulated wind and turbulence with observations from a meteorological mast and a northern wind turbine which are sometimes influenced by the presence of a wind turbine to the south. Finally, we investigate whether the application

of an analytical wake model as a post-processing tool applied to the simulation output improves the degree of agreement between measured and simulated values. The use of this post-processing tool starts to allow for a quantification of wake error sources versus other errors sources in the model such as the level of accuracy and detail in the lower boundary conditions.

7.2 Data and Methods

7.2.1 Measurements

The measurements were collected at the Wind Energy Institute of Canada during the Prince Edward Island Wind Energy Experiment (PEIWEE) [34]. A period of 15 days is considered (May 11-25, 2015). Wind measurements used herein were made at a frequency of 10 Hz with a 3-D Gill Windmaster Pro sonic anemometer mounted to a meteorological mast (compliant with International Electrotechnical Commission standards) at 60 m above ground. Additionally, 10-minute mean wind speed, nacelle position and power production data from two 2-MW DeWind D9.2 turbines are used. The WT hub height is 80 m and the rotor diameter (D) 93 m. The location of the turbines and the mast is shown in Fig. 7.1.

7.2.2 Simulation

The simulation was performed by running the Advanced Research core of the WRF model for a dynamical downscaling consisting of two well differentiated

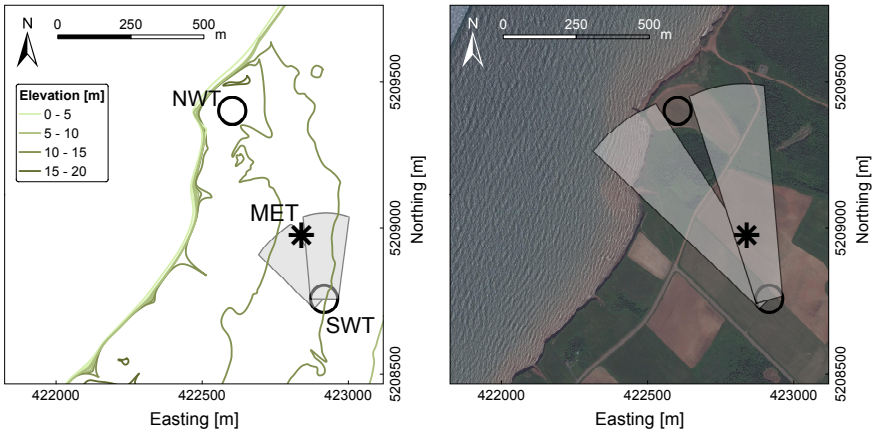

Figure 7.1: Instrument locations at the measurement site: wind turbines (circles of diameter 93 m) and meteorological mast (star). Elevation contours [m] (a) and satellite imagery from Environmental Systems Research Institute (b). Shaded areas represent wake from SWT impacting MET (a) and NWT (b).

phases: meso scale and micro scale. Five domains were defined, centered at the meteorological mast location (see Section 7.2.1) following a set of telescopic nests from 9 km to 111 m under a two-way nesting approach. The domains were configured to have 70 points in both directions and 50 vertical levels distributed every ~10 m within the atmospheric boundary layer. The model source code was modified to enable meso-micro scale coupling based on the potential temperature perturbation method described in [163, 164]. Previous work has shown that this modification results in an improvement to simulations of wind speed and turbulence intensity under different meteorological regimes and terrain complexities [165, 166]. Details of the implementation constitute proprietary information and cannot be disclosed. The innermost domain was run on LES mode, switching off the physical parameterizations. The other domains (including the terra incognita [54] domain at a 333 m grid resolution) were run with the YSU [162] boundary layer scheme.

Initial and boundary conditions are taken from the Climate Forecast System

Reanalysis [167] with a spatial resolution of ~ 38 km. The static data for the high resolution domains are taken from the Shuttle Radar Topography Mission (at a 90 m resolution) [168] for topography and from the GlobCover [169] for land use. Other fields are taken from the default data sets provided by the model. The model was run for a 15-day period and time series were saved at three points: the northern wind turbine (NWT), the meteorological mast (MET), and the southern wind turbine (SWT), whose locations are shown in Fig. 7.1. The model saves historic output with a temporal frequency of 4 Hz. These values are then used to compute 10-minute averages and standard deviation, considering seven heights between ~ 8 m and ~ 182 m.

7.2.3 Wake Periods

To quantify the effect of WT wakes on model performance, the simulated values were compared to observations in the presence and absence of wakes. Hereinafter these periods will be referred to as "waked" and "free", respectively. The only wake considered is that of SWT which is located ~ 230 m (~ 2.5 D) from MET and ~ 715 m (~ 7.7 D) from NWT.

To determine the interval of nacelle positions γ in which the SWT wake impacts the downstream locations considered, the wake width w at any downstream distance x is approximated as

$$w(x) = D + 2kx \tag{7.1}$$

following [106] where D is the rotor diameter of the wake-generating turbine and k the wake expansion coefficient taken here as 0.05 (i.e., 5% of wake expansion). This value was chosen based on previous recommendations for offshore

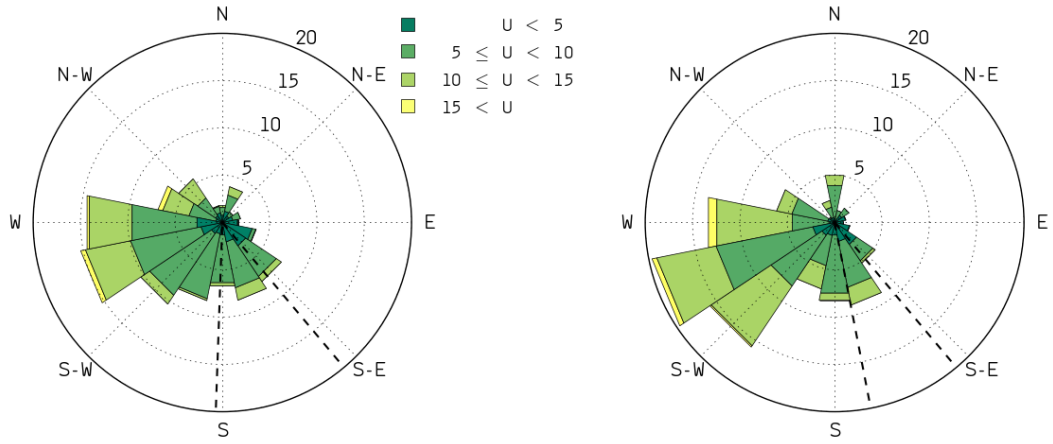

(a) Measured (b) Simulated

Figure 7.2: Wind roses at SWT during 15-day period considered (measurement height z = 80 m) using 10-minute mean measurements of wind speed and nacelle position in (a) and 10-minute mean simulated wind speed and direction at the grid cell containing SWT in (b). Color shading distinguishes between horizontal wind speed bins starting at 0 m s^{-1} in 5 m s^{-1} intervals. Radial axis gives normalized frequencies [%]. Dashed lines represent sectors in which MET (a) and NWT (b) are subjected to the SWT wake.

sites [178] because of the predominantly offshore footprint seen in the measurements collected at the island [34].

The range of waked sectors is shown for both downstream sites in Fig. 7.1. For MET (Fig. 7.1a) this interval is $\gamma_{SWT} \in (140°, 182°)$ (where γ_{SWT} is the SWT 10-minute mean nacelle position) and represents $\sim$ 16% of the entire time series. For NWT (Fig. 7.1b) it is $\gamma_{SWT} \in (140°, 169°)$ representing $\sim$ 11% of the data. The simulation reproduced well the frequency of occurrence and the magnitude of wind speeds in these directional sectors, as can be seen in Fig. 7.2. Note that the wake of NWT on the other locations is not considered because northwesterly winds were less frequent during the experiment as shown in Fig. 7.2.

7.2.4 Post-simulation wake correction

We propose and evaluate a post-simulation wake correction method which seeks to drive the model results closer to the observations after the simulations have been conducted, for sites where wind turbines are present. The method is built on the Jensen wake formulation [106], widely used in industry and the basis of the well-known Park model [105]. Following this approach, the expected velocity deficit (VD) at a point can be estimated as

$$\mathrm{VD}(t) = \frac{1 - \sqrt{1 - C_T(t)}}{\left(1 + \frac{kx}{R}\right)^2} \tag{7.2}$$

where C_T [-] is the thrust coefficient of the WT generating the wake, k [-] the wake expansion factor (also known as decay coefficient), x [m] the downstream distance between the WT generating the wake and the location of interest, and R [m] the WT rotor radius. We consider unsteady C_T values calculated from the SWT wind speed measurements and thrust curve. A constant expansion factor is assumed as recommended for the first turbines in the row of a wind farm [179]. From Eq. (7.2) and a free stream velocity U_∞, a velocity corrected for the wake can be estimated as $U = U_\infty\,(1 - \mathrm{VD})$.

7.2.5 Variables and Notation

All of the variables considered throughout the analysis are 10-minute means. We focus on quantities of relevance to wind energy such as power P, horizontal wind speed U, wind direction β, nacelle position γ, and turbulence intensity $I = \sigma_U/U$ (where σ_U is the standard deviation of U over a 10-minute period). Wind direction measurements at the turbines were not provided. We assume

negligible yaw misalignment at the two turbines so that nacelle position measurements can be treated as wind direction measurements (i.e., $\beta \sim \gamma$). The predicted power for the simulations is obtained from the simulated 10-minute mean wind speeds at hub height and the turbine power curve.

The analysis is predominantly based on calculated differences δ between the simulated and measured variables such that $\delta = x_{\mathtt{sim}} - x_{\mathtt{obs}}$, evaluated at each 10-minute mean time stamp for which observation were available. Absolute differences $|\delta|$ are used to determine the overall magnitude of the model error, and averages over a given time series are symbolized as $\overline{\delta}$ so that a mean absolute error is $\overline{|\delta|}$. The subscripts "w" and "f" (i.e., δ_w versus δ_f) differentiate between values in waked versus free directional sectors following the definition given in Section 7.2.3. Note that only coinciding time stamps are included in analyses that consider both observational and simulation data. To minimize the uncertainty, model values are not interpolated to different heights to conduct the analysis. Because there is a high density of values in the vertical (z) direction in the model, we simply consider the model level ($z_{\mathtt{sim}}$) that is closest to the observation height ($z_{\mathtt{obs}}$). At MET (NWT) the measuring height is $z_{\mathtt{obs}} = 60$ m (80 m) and the simulation height $z_{\mathtt{sim}} \sim 52$ m (~ 80 m).

7.3 Results

The results presented herein are divided into three sections. First, a general evaluation of the model performance during waked conditions (Section 7.3.1). Second, a comparison of model performance under waked versus free stream conditions (Section 7.3.2). Finally, an assessment of the post-simulation wake

correction technique is given (Section 7.3.3).

7.3.1 Model performance under "waked" conditions

When operational, WTs convert a portion of the mean kinetic energy into electricity. The momentum deficit downstream leads some of this mean energy to cascade down the spectrum increasing the turbulent kinetic energy budget [180] and the ambient turbulence intensity. It is therefore expected that a simulation which fails to account for the effect of WTs on the flow will overestimate U and underestimate I. In terms of wind speed (Fig. 7.3, left) this expectation was only confirmed at the site MET. At NWT the model mostly underestimated the wind speed with a small mean error of $\overline{\delta} \sim -0.1$ m s^{-1}. For I (Fig. 7.3, center) the expectations are confirmed at both sites, with mean underestimations of $\overline{\delta} \sim -0.06$ at NWT and $\overline{\delta} \sim -0.15$ at MET.

The wind direction errors (Fig. 7.3, right) were similar at both sites, with the largest occurrences in the bin $\beta \in (0°, 30°)$ at NWT and $\beta \in (-30°, 0°)$ at MET. It is important to note that these direction errors can be brought on not only by the presence of wind turbine wakes, but also by the presence of other roughness elements at the site, which can lead to the development of internal boundary layers over roughness changes and to a modification in the displacement height [181]. More details on the effect of roughness and topography changes on near-surface flow can be found in [182]. More details for the present site can be found in [34]. In the next section, the role of wakes in explaining this discrepancy is estimated.

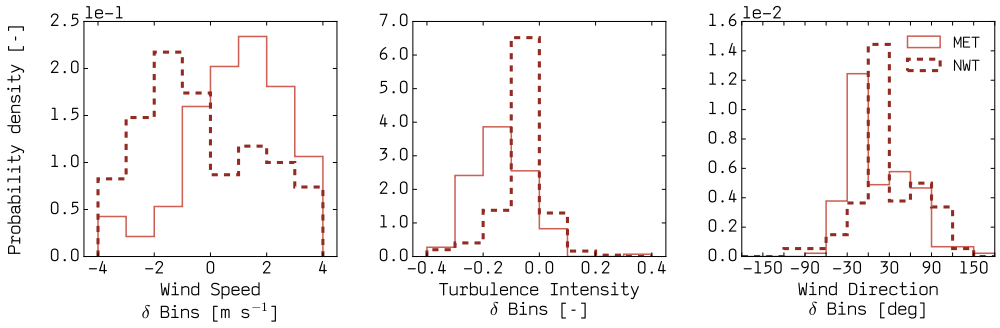

Figure 7.3: Probability density of model errors during waked conditions at MET (solid) and NWT (dashed) for time series of 10-minute means: wind speed (left), turbulence intensity (center) and wind direction (right). For wind direction, the standard 30° bin width is chosen.

Table 7.1: Temporal mean of model absolute errors at MET and NWT when considering waked ($\overline{|\delta_w|}$) and free ($\overline{|\delta_f|}$) conditions. Note that power error values are only available at the NWT site, and do not consider time stamps in which the NWT was not producing power.

		MET		NWT	
Variable	Unit	$\overline{\lvert\delta_w\rvert}$	$\overline{\lvert\delta_f\rvert}$	$\overline{\lvert\delta_w\rvert}$	$\overline{\lvert\delta_f\rvert}$
Wind Speed U	[m s^{-1}]	3.1	2.3	2.1	2.1
Wind Direction β	[deg]	35.5	34.7	40.2	18.6
Turbulence Intensity I	[-]	0.16	0.07	0.08	0.06
Power P	[kW]			495.4	385.8

7.3.2 Model performance under waked versus free conditions

To estimate how much the presence of WT wakes affects the model performance, mean absolute errors $\overline{|\delta|}$ can be computed separately over the entire free and waked periods as given in Table 7.1. Note that in these averages, only absolute values are considered and therefore the information given in Table 7.1 differs from that in Fig. 7.3 where the sign of the error values was kept.

The results show that $\overline{|\delta_w|} > \overline{|\delta_f|}$ consistently. For wind speed, the error was $\sim$ 35% higher at MET during the waked period but remained the same for both

periods at the NWT site. These results along with those shown in Fig. 7.3 indicate that the model performance at MET was more affected by the presence of a wake than at NWT. It is important to note that although the wind speed errors under both flow scenarios are indistinguishable at NWT, the same is not true for power. Relatively small differences in wind speed may result in large differences in estimated power depending on the magnitude of the wind speeds. The power estimated from the simulation data presented larger errors under waked conditions, and consider only periods in which the NWT was operating.

The turbulence intensity error differences between waked and free conditions are especially large at MET, where the model failed to simulate high turbulence periods (Fig. 7.4a). These high turbulence periods in the measurements coincide with waked periods where sometimes the variation in wind speeds over 10 minutes is very large due to the intermittence and inhomogeneity of the flow under these conditions. At NWT (Fig. 7.4b) the model better reproduced the variation of turbulence with wind speed, but still performed better during free conditions.

As mentioned in Section 7.3.1 and verified in Fig. 7.4, the model consistently underestimated the turbulence levels not only under waked but also under free conditions. The underestimation of turbulence by the model should be interpreted with caution because it can be brought on by data and model limitations that are not necessarily related to the absence of a wind turbine wake model. For example, the presence of an escarpment also contributes to enhanced turbulence at this site for the heights considered [34] and limitations in the spatial resolution of the lower boundary conditions could partly explain the I underestimation seen also during free stream periods. Moreover, a portion of this underes-

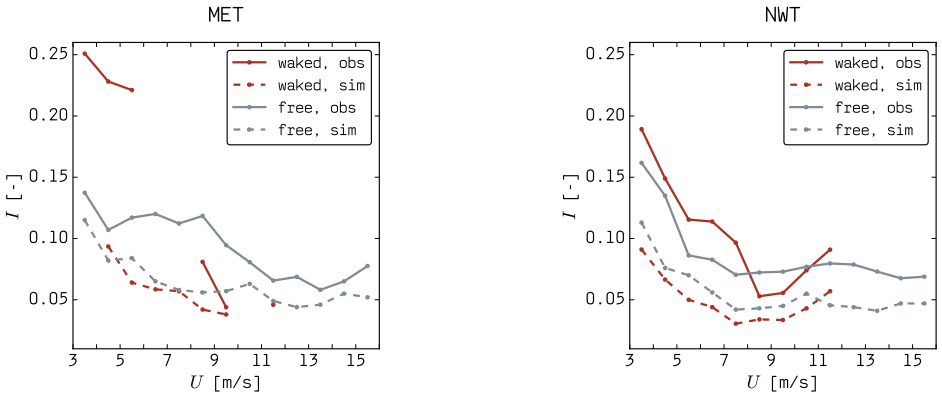

(a) (b)

Figure 7.4: Median turbulence intensity I [-] as a function of horizontal wind speed U [m s^{-1}] at MET (a) and NWT (b) when subjected to free stream flow (gray) and to the wake of SWT (red) for measurements (solid) and simulations (dashed). Each median value corresponds to a discrete horizontal wind speed bin starting at 3 m s^{-1} in 1 m s^{-1} intervals.

timation of turbulence intensity can likely be attributed to the numerical treatment of the transition from the meso to the micro scale, and the method chosen to simulate turbulence in the terra incognita [54] domain (see Section 7.2.2). Fig. 7.4 also shows that the simulated turbulence intensity was slightly higher for the free sectors which include not only an onshore but also an offshore footprint, adding to the flow complexity as it transitions over different roughness and terrain regimes. Note that error metrics given in Table 7.1 are not necessarily representative of the overall model skill, which should be evaluated with longer (e.g., one year) simulations. These investigations are beyond the scope of the present work, which seeks to differentiate the model performance under the two scenarios considered.

The wind direction differences between the SWT and NWT locations was also underestimated by the model as shown in Fig. 7.5. However, the model errors are very similar under free and waked periods, indicating that this was not an inability to simulate wake-induced meandering and rather a consequence of

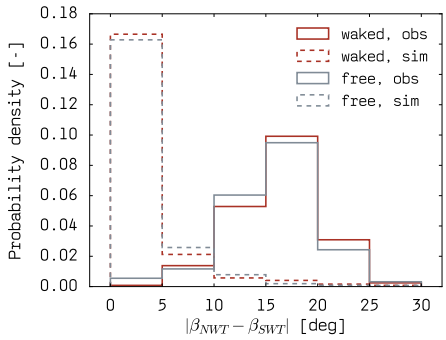

Figure 7.5: Histogram of wind direction differences between SWT and NWT during waked (red) and free (gray) periods from observations (solid) and simulation (dashed). Absolute differences are forced to the interval $[0°, 180°]$.

other model limitations likely relating to surface phenomena as such as the spatial resolution of the lower boundary conditions (i.e., roughness elements, terrain elevation, land-sea mask, sea surface temperatures) and the surface layer treatment to ensure the development of internal boundary layers both for on and offshore flow depending on the wind direction.

7.3.3 Post-simulation wake correction

In this section, the effect of the SWT wake is added to the simulated wind speed sampled at MET and NWT after the simulation has been completed. We seek to determine whether this approach can improve the results with respect to local wind speed and turbine power prediction. Such an approach is of great value to the scientific community for being easy to implement and for eliminating the need for the costly alternative of fully coupling fluid and structural dynamics solvers, but it does not affect the turbulence and wind direction estimates. The method employed is described in Section 7.2.4.

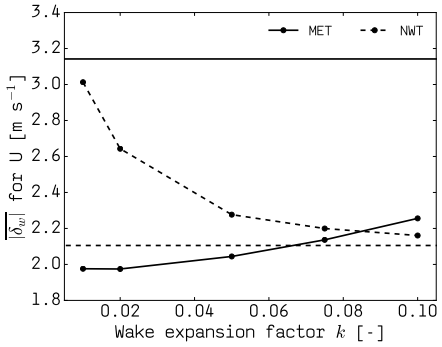

Figure 7.6: Mean absolute errors $\overline{|\delta_w|}$ for horizontal wind speed U [m s^{-1}] during waked periods without the wake correction (horizontal lines) and with the wake correction (lines with markers) at MET (solid) and NWT (dashed) sites, as a function of the expansion factor k [-] used in the Jensen wake expression (Eq. (7.2)).

We find that the wake correction method improves the error metrics by bringing the MET wind speed values closer to the observations during waked periods. Namely, the mean error goes from ~ 3.1 m s^{-1} (Table 7.1) at this site before the wake correction to ~ 2.0 m s^{-1} after the correction is applied (Fig. 7.6). The sensitivity of the results to different wake expansion factors was evaluated as shown in Fig. 7.6. All k values resulted in a reduction of the mean error at MET, but the largest improvement was seen for $k = 2\%$ where $\overline{|\delta_w|}$ was reduced by $\sim 38\%$ relative to the mean error for the non-corrected U values. This result agrees with expectations for the site during the period considered, where atmospheric conditions were mostly stable [34]. This expansion factor is close to the WAsP recommended value of $k = 5\%$ for offshore conditions [178] and is in agreement with the expectations for the measurements site (i.e., flat and narrow island with flow characteristics that often resemble those of offshore environments [34]).

At the NWT site, the post-processing wake correction had the opposite effect and increased the mean model error. This is expected following the analyses in

Sections 7.3.1 and 7.3.2 which showed that the model already underestimated U, demonstrating that errors at this location are not necessarily related to the absence of a WT wake representation, but are rather a result of a combination of factors including limitations in the data and model, and in the post-processing technique itself which assumes a constant wind direction.

7.4 Conclusion

When wind turbines and their wakes are not represented in atmospheric models, the simulation performance is compromised. In this work, we quantify this effect by comparing model and observational data separately during free stream and wake conditions. Three unique data sets are considered which include a sonic anemometer mounted onto a meteorological mast compliant with the International Electrotechnical Commission standards [13], two utility-scale wind turbines, and cutting-edge WRF-LES simulations at a spatial resolution of 111 m. We focus on flow parameters of relevance to wind energy: wind speed, wind direction, and turbulence intensity. The wake of one turbine on two downstream sites is considered, namely a meteorological mast and another turbine.

We find that the model consistently underestimates turbulence intensity at both sites, but the relationship of this result with the absence of a wake description is only evident at one of the sites, where the model wind speed error in the presence of a wake is $\sim$ 35% larger than during free stream conditions. At the other site, the wind speed is underestimated indicating that these errors are related to other model and data limitations, such as the resolution and fidelity of the lower boundary conditions. The model also consistently underestimates the

wind direction difference between the turbines regardless of whether a wake is present, evidence that this is not an inability of the model to simulate wake-induced meandering. Despite these shortcomings, it is important to keep in mind that the simulation considered is not long enough to undertake a thorough evaluation of the model skill which is beyond the scope of the work.

Finally, we find that a post-simulation wake correction reduces the error in wind speed estimates by $\sim$ 38% at the site that presented larger errors under wake conditions, but increases the errors at the other site which is in a coastal location, and in the far wake. The wake correction is done using the Jensen wake formulation and the best results are found using a wake expansion parameter of $k = 2\%$. This value is lower than has typically been found for offshore environments [183] but is consistent with the strongly stable conditions observed during the PEIWEE field campaign [34]. These preliminary results alert to the dangers of blindly applying a post-processing tool without consideration for other model error and uncertainty sources, which under certain conditions (e.g., complex terrain) may be larger in magnitude than the errors brought on by the absence of a wind turbine model. This analysis also reiterates the need for a wind turbine wake parameterization for high resolution WRF-LES which will improve simulations of wind speed, wind direction and turbulence intensity within and around wind power plants.

CHAPTER 8

SUMMARY AND FUTURE WORK

8.1 Summary

Atmospheric phenomena ranging from the macro to the micro scale impact wind plant aerodynamics. As a result, it is difficult to approach research problems within wind engineering using either observations or models as tools. Instead, an integration of both is needed to allow for more comprehensive analyses with a lower level of uncertainty. In this dissertation, both techniques are used to tackle a collection of problems in wind resource assessment (Chapter 2), wake modeling (Chapters 3, 4 and 7) and characterization (Chapter 5), and meso-micro coupling within models (Chapter 6).

The research developed takes into consideration the body of work from other research groups, and proposes methods to integrate models and measurements with the ultimate objective of reducing uncertainties in wind characterization. By developing and documenting tools, and by estimating uncertainties related to specific aspects of wind characterization methodologies, this dissertation has added knowledge to the scientific community that can facilitate research in the fields of resource assessment, wind turbine wake characterization, and meso-micro scale model coupling.

8.1.1 Wind Resource Assessment

An observation-based wind atlas was produced for the Great Lakes taking advantage of different data sources, and providing a blueprint for future observation-based offshore wind resource assessment efforts. Coastal stations provided long (3 to 11 years) and complete records that captured the diurnal, seasonal and interannual variability of the wind resource close to the coast. Buoys provided a long dataset (~11 years) and accurate representation of offshore conditions and were corrected for the lack of data during the ice season using a long record of high-resolution reanalysis. Satellite-derived winds contributed with the spatial coverage that in situ measurements cannot provide. While QuikSCAT offered a spatially and temporally consistent long record of offshore winds at a low resolution, SAR provided higher resolution including proximity to the coast, but with an inconsistent and irregular space and time coverage.

It was demonstrated that the combination of several observational data sets can yield a robust wind atlas offshore, reducing the uncertainty in the final resource estimate when compared to results using a single data set as initially postulated. Moreover, model data was found to be a useful tool to constrain and expand measurements that are otherwise incomplete and therefore fail to represent wind variability across multiple temporal scales. The final wind speed map presented a spatially averaged bias of 0.1 m s^{-1} and a spatial root-mean-squared error of 0.3 m s^{-1}. By combining the buoy observations with a bulk flux algorithm for ocean-atmosphere interaction, it was found that considering satellite-derived equivalent neutral winds instead of stability-dependent winds results in an uncertainty of $O(10^{-1})$ m s^{-1} on average for the Great Lakes. The

methodology proposed herein can be applied to other offshore regions to derive observation-based wind atlases.

8.1.2 Wind Turbine Wake Modeling

The Stochastic Shape Wake Model

Prior to developing new wake modeling approaches, the present work documented a variety of wake characterization metrics and investigated their differences. Subsequently, the initial development of a stochastic wake simulator was presented which addresses the need for computationally inexpensive models to simulate unsteady wind turbine wakes with sufficient accuracy and detail to conduct analyses of fluctuating loads and power. By driving the results obtained with this low-fidelity model towards those produced by the large-eddy simulation (LES), the uncertainty in these idealized simulations is reduced according to the definitions presented in Section 1.4.

Based on a LES simulation of an offshore wind farm, a linear relationship is found to describe the spectral energy content of each wave number describing the wake edge intermittence. Two regimes exist, where the high wave numbers follow a steeper slope. These spectra are combined with statistical tools to produce the stochastic wake shape (SWS) model, which moves away from steady solutions and assumptions of axial symmetry and seeks to account for the effects of wake-induced turbulence in the wake shape. The wake simulated with the proposed model matches very well the mean characteristics of the original LES wake. The mean shape shows the same area and stretching patterns, and the mean azimuthal radius yields very similar mean (e.g., ~1.3 D at 2 D), stan-

dard deviation (e.g., ~0.1 D at 2 D) and first-order auto-correlation values (~0.9 at all downstream distances considered).

The contribution of the proposed SWS model to simulations of loads and power, particularly their unsteady fluctuations, was quantified by assessing the role of different wake modeling components. Three aeroelastic simulations were conducted in which the same virtual turbine was subjected to different wake flow fields. It was found that meandering is a large contributor to the loads experienced by the turbine, and that removing it from the simulations can reduce the loading estimate by more than 50 % in the case an axisymmetric model. The asymmetry in wake shape was also found to affect the load magnitudes, with the proposed SWS model producing damage-equivalent loads (DEL) significantly closer to the reference LES values. Even with an axisymmetric velocity deficit (vd) distribution, the SWS model produced blade root out-of-plane DEL values that are ~70 % of the LES, which is encouraging considering that only the shape of the wake is being considered in this study and indicates that a higher level of agreement can be expected if an asymmetric description of the vd is added to the model. As discussed in Chapter 1 these results reflect a lowering of the uncertainty level in the low-fidelity model as it produces results that approach those obtained with higher fidelity, previously validated simulations.

Wake Effects on Simulation Performance

In Chapter 7, simulation results were combined with measurements to estimate how much of the discrepancy between measured and modeled flow parameters can be attributed to wake effects. The simulations were run with the Weather

Research and Forecasting (WRF) model nested down to a LES scale, and the wake of a turbine on two downstream sites was considered. One of the sites was subjected to the wake ~11 % of the time, and the other ~16 %.

While the model consistently underestimated turbulence intensity at both sites, this result is only related to the absence of a wake model at one of the sites, where the model wind speed error in the presence of a wake is ~35 % larger than during free stream conditions. A post-simulation wake correction was found to improve the model performance in terms of wind speed estimates by ~ 38 % at the site that presented larger errors under wake conditions. The best results in the wake correction were found using a wake expansion parameter of k = 0.02 (i.e., 2 % of wake expansion as it propagates downstream). However, the post-processing wake correction used herein increased the wind speed errors at the coastal site, which is in the far wake of the turbine. These results alert to the potential dangers of blindly applying a post-simulation wake correction without considering other sources of uncertainty in the simulation, and therefore without being able to determine with sufficient accuracy how much of the model error is due to the absence of a wake parameterization, and how much of it is due to other shortcomings in the data and model.

8.1.3 Wind Turbine Wake Measurements

In an effort to characterize wind turbine wakes from observations, this work analyzed scanning lidar measurements and estimated the level of uncertainty in the velocity retrievals and in the wake metrics derived from these retrievals. This was done by quantifying the difference between spatially- and temporally-

disjunct wind speed measurements sampled by a ground-based pulsed lidar, an instantaneous snapshot of the flow at the first second of the lidar scan, and the temporal means over the time the lidar takes to complete the 3D scan.

These different data sets were obtained by placing an imaginary lidar within a LES data set and recreating the scanning geometry of the field measurements. It was determined that wind speeds sampled with the synthetic lidar are closer to the mean (within ~10 %) than to the instantaneous values and that the disjunct nature of the scan does not compromise the spatial variation of wind speed within the downstream planes considered. The sampled points deviate more from the instantaneous values closer to the turbine, with rms differences ~13 % when averaged over 80 sector scan stacks. Scanning geometry coverage was found to be very important to characterize the wake center, orientation and length scales. Because of the radial symmetry in the mean vd field, ample coverage of points is not required to obtain good estimates of the vd mean and standard deviation for which scanning geometry density is more important. Based on the results, recommendations were made to the scientific community in terms of scanning geometry configurations when seeking to reduce measurement uncertainty for flow under single wake conditions.

8.1.4 Meso-Micro Model Coupling

Three multi-day, real case simulations fully coupled between the meso and micro scale were performed to investigate the consequences of different gray zone treatments to simulations of flow parameters. One of the simulations uses a well-established atmospheric boundary layer (ABL) parameterization, another

uses a version of it that has been modified for the gray zone, and a final one runs the gray zone domain without any parameterization at all. A micro scale nest is present in all simulations and run in LES mode without feedback to its parent. Since the modified parameterization was developed and tested on idealized simulations, the work presented herein is valuable to the scientific community in that it quantifies its effect on longer, full-physics, non-idealized simulations.

It was found that differences between the two simulations in which the ABL is parameterized can be large over short periods but disappear when multi-day averages are considered. The gray zone treatment was additionally found to affect simulation results at the innermost nest. The presence of this micro scale nest allowed for a recovery in the energy content at high frequencies, but the gray zone energy gap is still equally visible in all simulations. The parameterized simulations produce slightly better results in terms of horizontal wind speed and vertical wind shear, but the run without a parameterization performs best in terms of spectral energy content and kinematic heat flux. The magnitude of the simulations uncertainty due to gray zone treatment was found to be much lower than the magnitude of the model error.

8.2 Future work

This dissertation has made a series of incremental contributions to several aspects of wind engineering. Some of the work represents the initial step towards the development of a new technique whose applicability can be further expanded in future analyses. Other parts advance our knowledge in the field and can serve as guidance to further advances. The results obtained and the

methods developed are thoroughly documented and can be used to reproduce or build upon the work conducted. The following sections elaborate on possible directions for future work.

8.2.1 Wind Resource Assessment

The uncertainty in the developed offshore wind atlas can be further reduced by considering the atmospheric stability when processing satellite-derived equivalent neutral winds and extrapolating to hub heights. A recent effort in this direction was undertaken [31] but more work needs to be done so that wind resource assessment efforts can take full advantage of the available observations.

8.2.2 Wind Turbine Wake Modeling

The proposed SWS model can be expanded to serve as a mid-fidelity alternative to LES when accurate predictions of loads and power are sought. Future work should focus on generalizing the model to different atmospheric conditions and on investigating its dependence on wind turbine specific characteristics. This requires more LES to be run for a variety of atmospheric conditions and different inflow profiles. The wake shape perturbation spectra are expected to change, along with the probability distribution functions used to randomly sample the phases at low frequencies. The relative contribution of meandering to the wake edge statistics will also be explored and is expected to increase under conditions of higher turbulence intensity. It is also important to validate the aeroelastic simulations of loads and power relative to high-frequency turbine

measurements.

8.2.3 Wind Turbine Wake Measurements

To elaborate on the work presented and obtain more complete estimates of the uncertainty in velocity retrievals and wake characterization from scanning lidar measurements, future work should consider the effect of the lidar weighting function relative to the temporal lag across points. Furthermore, the analysis conducted herein can be generalized if repeated for LES under different atmospheric stability conditions.

8.2.4 Meso-Micro Model Coupling

From the work presented herein it was found that for multi-day real case simulations the present question is whether to run the gray zone in LES mode or with a parameterization at all, and not whether to even consider scale-aware parameterizations which are still in early development phases. Therefore, more work is needed to adapt traditional parameterizations and generalize them to a variety of atmospheric conditions so that realistic predictions of shear and turbulence can be obtained when non-idealized simulations are conducted.

BIBLIOGRAPHY

[1] US Energy Information Administration. International Energy Outlook. *Technical Report DOE/EIA-0484(2016)*, U.S. Energy Information Administration May 2016. URL www.eia.gov/forecasts/aeo.

[2] Nastrom GD, Gage KS, Jasperson WH. Kinetic energy spectrum of large- and mesoscale atmospheric processes. *Nature* Jul 1984; **310**(5972):36–38, doi:10.1038/310036a0. URL http://www.nature.com.proxy.library.cornell.edu/nature/journal/v310/n5972/abs/310036a0.html.

[3] Troen I, Petersen EL. *European Wind Atlas*. Commission of the European Communities, Directorate-General for Science, Research, and Development, Brussels, Belgium, 1989.

[4] US Energy Information Administration. International Energy Outlook. *Technical Report DOE/EIA-0484(2013)*, U.S. Energy Information Administration 2013. URL www.eia.gov/forecasts/aeo.

[5] US Energy Information Administration. Electric Power Monthly. *Technical Report*, U.S. Energy Information Administration, Washington, DC Oct 2016. URL https://www.eia.gov/electricity/monthly/pdf/epm.pdf.

[6] Wang H, Barthelmie RJ, Pryor SC, Kim HG. A new turbulence model for offshore wind turbine standards. *Wind Energy* Oct 2014; **17**(10):1587–1604, doi:10.1002/we.1654. WOS:000342682600009.

[7] Pryor SC, Barthelmie RJ, Schoof JT. Past and future wind climates over the contiguous USA based on the North American Regional Climate Change Assessment Program model suite. *Journal of Geophysical Research-Atmospheres* Oct 2012; **117**:D19 119, doi:10.1029/2012JD017449. WOS:000309831300002.

[8] Barthelmie RJ, Frandsen ST, Nielsen MN, Pryor SC, Rethore PE, Jørgensen HE. Modelling and measurements of power losses and turbulence intensity in wind turbine wakes at Middelgrunden offshore wind farm. *Wind Energy* Nov 2007; **10**(6):517–528, doi:10.1002/we.238. URL http://onlinelibrary.wiley.com.proxy.library.cornell.edu/doi/10.1002/we.238/abstract.

[9] Jung J, Broadwater RP. Current status and future advances for wind speed and power forecasting. *Renewable and Sustainable Energy Reviews* Mar 2014; **31**:762–777, doi:10.1016/j.rser.2013.12.054. URL http://www.sciencedirect.com/science/article/pii/S1364032114000094.

[10] Gebraad PMO, Teeuwisse FW, van Wingerden JW, Fleming PA, Ruben SD, Marden JR, Pao LY. Wind plant power optimization through yaw control using a parametric model for wake effects—a CFD simulation study. *Wind Energy* Jan 2016; **19**(1):95–114, doi:10.1002/we.1822. URL http://onlinelibrary.wiley.com/doi/10.1002/we.1822/abstract.

[11] Mehta D, van Zuijlen AH, Koren B, Holierhoek JG, Bijl H. Large Eddy Simulation of wind farm aerodynamics: A review. *Journal of Wind Engineering and Industrial Aerodynamics* Oct 2014; **133**:1–17, doi:10.1016/j.jweia.2014.07.002. URL http://www.sciencedirect.com/science/article/pii/S0167610514001391.

[12] Barthelmie RJ, Doubrawa P, Pryor SC. Best Practice for Measuring Wind Speeds and Turbulence Offshore through In-situ and Remote Sensing Technologies. *Report to Department of Energy DE- EE0005379* Jul 2016. URL http://doi.org/10.7298/X4QV3JGF.

[13] International Electrotechnical Comission. Wind Turbines - Part 12-1: Power performance measurements of electricity producing wind turbines. *Technical Report IEC 61400-12-1:2005(E)* 2005.

[14] Borraccino A, Courtney M, Wagner R. Generic Methodology for Field Calibration of Nacelle-Based Wind Lidars. *Remote Sensing* Nov 2016; **8**(11):907, doi:10.3390/rs8110907. URL http://www.mdpi.com/2072-4292/8/11/907.

[15] Stotsky A, Egardt B, Carlson O. An overview of proactive wind turbine control. *Energy Science & Engineering* Apr 2013; **1**(1):2–11, doi:10.1002/ese3.5. URL http://onlinelibrary.wiley.com/doi/10.1002/ese3.5/abstract.

[16] Doubrawa P, Barthelmie RJ, Wang H, Pryor SC, Churchfield MJ. Wind Turbine Wake Characterization from Temporally Disjunct 3-D Measurements. *Remote Sensing* Nov 2016; **8**(11):939, doi:10.3390/rs8110939. URL http://www.mdpi.com/2072-4292/8/11/939.

[17] Wang H, Barthelmie RJ, Clifton A, Pryor SC. Wind Measurements from

Arc Scans with Doppler Wind Lidar. *Journal of Atmospheric and Oceanic Technology* Nov 2015; **32**(11):2024–2040, doi:10.1175/JTECH-D-14-00059.1. WOS:000365603300003.

[18] Floors R, Vincent CL, Gryning SE, Peña A, Batchvarova E. The Wind Profile in the Coastal Boundary Layer: Wind Lidar Measurements and Numerical Modelling. *Boundary-Layer Meteorology* Jun 2013; **147**(3):469–491, doi:10.1007/s10546-012-9791-9. URL http://link.springer.com/article/10.1007/s10546-012-9791-9.

[19] Westerhellweg A, Canadillas B, Beeken A, Neumann T. One year of LiDAR measurements at FINO1-Platform: Comparison and verification to met-mast data. *Proceedings of 10th German wind energy conference DEWEK*, 2010; 1–5.

[20] Probst O, Cárdenas D. State of the Art and Trends in Wind Resource Assessment. *Energies* Jun 2010; **3**(6):1087–1141, doi:10.3390/en3061087. URL http://www.mdpi.com/1996-1073/3/6/1087.

[21] Rhodes ME, Lundquist JK. The Effect of Wind-Turbine Wakes on Summertime US Midwest Atmospheric Wind Profiles as Observed with Ground-Based Doppler Lidar. *Boundary-Layer Meteorology* Oct 2013; **149**(1):85–103, doi:10.1007/s10546-013-9834-x. URL http://link.springer.com/article/10.1007/s10546-013-9834-x.

[22] Wang H, Barthelmie RJ. Wind turbine wake detection with a single Doppler wind lidar. *Journal of Physics: Conference Series* 2015; **625**(1):012 017, doi:10.1088/1742-6596/625/1/012017. URL http://stacks.iop.org/1742-6596/625/i=1/a=012017.

[23] Schlipf D. Lidar-assisted control concepts for wind turbines. Ph.D. dissertation, University of Stuttgart 2016. URL http://elib.uni-stuttgart.de/bitstream/11682/8813/1/PhDSchlipf_LidarAssistedControlConceptsForWindTurbines.pdf, doi:10.18419/opus-8796.

[24] Aitken ML, Lundquist JK. Utility-Scale Wind Turbine Wake Characterization Using Nacelle-Based Long-Range Scanning Lidar. *Journal of Atmospheric and Oceanic Technology* Apr 2014; **31**(7):1529–1539, doi:10.1175/JTECH-D-13-00218.1. URL http://journals.ametsoc.org/doi/abs/10.1175/JTECH-D-13-00218.1.

[25] Doubrawa P, Barthelmie RJ, Pryor SC, Hasager CB, Badger M, Karagali

I. Satellite winds as a tool for offshore wind resource assessment: The Great Lakes Wind Atlas. *Remote Sensing of Environment* Oct 2015; **168**:349–359, doi:10.1016/j.rse.2015.07.008. URL http://www.sciencedirect.com/science/article/pii/S0034425715300651.

[26] Hasager CB, Mouche A, Badger M, Bingöl F, Karagali I, Driesenaar T, Stoffelen A, Peña A, Longépé N. Offshore wind climatology based on synergetic use of Envisat ASAR, ASCAT and QuikSCAT. *Remote Sensing of Environment* Jan 2015; **156**:247–263, doi:10.1016/j.rse.2014.09.030. URL http://www.sciencedirect.com/science/article/pii/S0034425714003848.

[27] Hasager CB, Vincent P, Husson R, Mouche A, Badger M, Peña A, Volker P, Badger J, Bella AD, Palomares A, *et al.*. Comparing satellite SAR and wind farm wake models. *Journal of Physics: Conference Series* 2015; **625**(1):012 035, doi:10.1088/1742-6596/625/1/012035. URL http://stacks.iop.org/1742-6596/625/i=1/a=012035.

[28] Elfouhaily T, Chapron B, Katsaros K, Vandemark D. A unified directional spectrum for long and short wind-driven waves. *Journal of Geophysical Research: Oceans* Jul 1997; **102**(C7):15 781–15 796, doi:10.1029/97JC00467. URL http://onlinelibrary.wiley.com/doi/10.1029/97JC00467/abstract.

[29] Charnock H. Wind stress on a water surface. *Quarterly Journal of the Royal Meteorological Society* 1955; **81**(350):639–640.

[30] Tang W, Liu WT. *Equivalent neutral wind*. Jet Propulsion Laboratory, National Aeronautics and Space Administration, 1996.

[31] Badger M, Peña A, Hahmann AN, Mouche AA, Hasager CB. Extrapolating Satellite Winds to Turbine Operating Heights. *Journal of Applied Meteorology and Climatology* Dec 2015; **55**(4):975–991, doi:10.1175/JAMC-D-15-0197.1. URL http://journals.ametsoc.org/doi/abs/10.1175/JAMC-D-15-0197.1.

[32] Rabin RM, Corfidi SF, Brunner JC, Hane CE. Detecting winds aloft from water vapour satellite imagery in the vicinity of storms. *Weather* Sep 2004; **59**(9):251–257, doi:10.1256/wea.182.03. URL http://onlinelibrary.wiley.com.proxy.library.cornell.edu/doi/10.1256/wea.182.03/abstract.

[33] Line WE, Schmit TJ, Lindsey DT, Goodman SJ. Use of Geostationary

Super Rapid Scan Satellite Imagery by the Storm Prediction Center *. *Weather and Forecasting; Boston* Apr 2016; **31**(2):483–494, doi:http://dx.doi.org.proxy.library.cornell.edu/10.1175/WAF-D-15-0135.1. URL http://search.proquest.com.proxy.library.cornell.edu/docview/1791670132/abstract/60800B90E1544C6CPQ/1.

[34] Barthelmie RJ, Wang H, Doubrawa P, Giroux G, Pryor SC. Effects of an escarpment on flow parameters of relevance to wind turbines. *Wind Energy* Dec 2016; **19**(12):2271–2286, doi:10.1002/we.1980. URL http://onlinelibrary.wiley.com/doi/10.1002/we.1980/abstract.

[35] Doubrawa P, Barthelmie RJ, Wang H, Churchfield MJ. A stochastic wind turbine wake model based on new metrics for wake characterization. *Wind Energy* Mar 2017; **20**(3):449–463, doi:10.1002/we.2015. URL http://onlinelibrary.wiley.com/doi/10.1002/we.2015/abstract.

[36] Iungo GV, Viola F, Ciri U, Rotea MA, Leonardi S. Data-driven RANS for simulations of large wind farms. *Journal of Physics: Conference Series* 2015; **625**(1):012 025, doi:10.1088/1742-6596/625/1/012025. URL http://stacks.iop.org/1742-6596/625/i=1/a=012025.

[37] Schlipf D, Schlipf DJ, Kühn M. Nonlinear model predictive control of wind turbines using LIDAR. *Wind Energy* Oct 2013; **16**(7):1107–1129, doi:10.1002/we.1533. URL http://onlinelibrary.wiley.com/doi/10.1002/we.1533/abstract.

[38] Bingöl F, Mann J, Larsen GC. Light detection and ranging measurements of wake dynamics part I: one-dimensional scanning. *Wind Energy* Jan 2010; **13**(1):51–61, doi:10.1002/we.352. URL http://onlinelibrary.wiley.com/doi/10.1002/we.352/abstract.

[39] Lundquist JK, Churchfield MJ, Lee S, Clifton A. Quantifying error of lidar and sodar Doppler beam swinging measurements of wind turbine wakes using computational fluid dynamics. *Atmos. Meas. Tech.* Feb 2015; **8**(2):907–920, doi:10.5194/amt-8-907-2015. URL http://www.atmos-meas-tech.net/8/907/2015/.

[40] Orlanski I. A rational subdivision of scales for atmospheric processes. *Bulletin of the American Meteorological Society* 1975; **56**:527–530.

[41] Sarlak H, Pierella F, Mikkelsen R, Sørensen JNe. Comparison of two LES

codes for wind turbine wake studies. *Journal of Physics: Conference Series*, vol. 524, IOP Publishing, 2014; 012 145.

[42] Wyngaard JC. *Turbulence in the Atmosphere*. Cambridge University Press, 2010.

[43] Krishnamurthy R, Calhoun R, Fernando H. Large-Eddy Simulation-Based Retrieval of Dissipation from Coherent Doppler Lidar Data. *Boundary-Layer Meteorology* May 2010; **136**(1):45–57, doi:10.1007/s10546-010-9495-y. URL `http://link.springer.com/article/10.1007/s10546-010-9495-y`.

[44] Shin HH, Hong SY. Analysis of Resolved and Parameterized Vertical Transports in Convective Boundary Layers at Gray-Zone Resolutions. *Journal of the Atmospheric Sciences* Jul 2013; **70**(10):3248–3261, doi:10.1175/JAS-D-12-0290.1. URL `http://journals.ametsoc.org/doi/abs/10.1175/JAS-D-12-0290.1`.

[45] Sanz Rodrigo J, Chávez Arroyo RA, Moriarty P, Churchfield M, Kosović B, Réthoré PE, Hansen KS, Hahmann A, Mirocha JD, Rife D. Mesoscale to microscale wind farm flow modeling and evaluation. *Wiley Interdisciplinary Reviews: Energy and Environment* Aug 2016; :n/a–n/adoi:10.1002/wene.214. URL `http://onlinelibrary.wiley.com.proxy.library.cornell.edu/doi/10.1002/wene.214/abstract`.

[46] Churchfield M, Lee S, Moriarty P, Martinez L, Leonardi S, Vijayakumar G, Brasseur J. A large-eddy simulation of wind-plant aerodynamics. *50th AIAA Aerospace Sciences Meeting including the New Horizons Forum and Aerospace Exposition*, 2012; 537. URL `http://arc.aiaa.org/doi/pdf/10.2514/6.2012-537`.

[47] Sanderse B, van der Pijl S, Koren B. Review of computational fluid dynamics for wind turbine wake aerodynamics. *Wind Energy* Oct 2011; **14**(7):799–819, doi:10.1002/we.458. URL `http://onlinelibrary.wiley.com.proxy.library.cornell.edu/doi/10.1002/we.458/abstract`.

[48] Larsen GC, Madsen Aagaard H, Bingöl F, Mann J, Ott S, Sørensen JN, Okulov V, Troldborg N, Nielsen NM, Thomsen K, *et al.*. Dynamic wake meandering modeling. *Technical Report*, Risø National Laboratory 2007.

[49] Ott S. Linearised CFD models for wakes. *Technical Report*, Danmarks Tekniske Universitet, Risø Nationallaboratoriet for B\a eredygtig Energi 2011.

[50] Mortensen N, Landberg L, Troen I, Lundtang Petersen E. Wind atlas analysis and application program (WAsP). *Technical Report Risø-I-666(EN)(v.1)*, Risø National Lab., Roskilde (Denmark). Meteorology and Wind Energy 1993.

[51] Hewitson B, Crane R. Climate downscaling: techniques and application. *Climate Research* 1996; **7**(2):85–95.

[52] Pryor SC, Schoof JT, Barthelmie RJ. Empirical downscaling of wind speed probability distributions. *Journal of Geophysical Research: Atmospheres* Oct 2005; **110**(D19):D19 109, doi:10.1029/2005JD005899. URL http://onlinelibrary.wiley.com/doi/10.1029/2005JD005899/abstract.

[53] de Rooy WC, Kok K. A Combined Physical–Statistical Approach for the Downscaling of Model Wind Speed. *Weather and Forecasting* Jun 2004; **19**(3):485–495, doi:10.1175/1520-0434(2004)019<0485:ACPAFT>2.0.CO;2. URL http://journals.ametsoc.org/doi/abs/10.1175/1520-0434(2004)019%3C0485%3AACPAFT%3E2.0.CO%3B2.

[54] Wyngaard JC. Toward Numerical Modeling in the "Terra Incognita". *Journal of the Atmospheric Sciences* Jul 2004; **61**(14):1816–1826, doi:10.1175/1520-0469(2004)061<1816:TNMITT>2.0.CO;2. URL http://journals.ametsoc.org/doi/abs/10.1175/1520-0469(2004)061%3C1816:TNMITT%3E2.0.CO;2.

[55] Doubrawa P, Barthelmie RJ, Wang H, Churchfield MJ. Contributions of the Stochastic Shape Wake Model to Predictions of Aerodynamic Loads and Power under Single Wake Conditions. *Journal of Physics: Conference Series* 2016; **753**(8):082 006, doi:10.1088/1742-6596/753/8/082006. URL http://stacks.iop.org/1742-6596/753/i=8/a=082006.

[56] Pielke Sr RA. *Mesoscale meteorological modeling*, vol. 98. Academic press, 2013.

[57] Tangler JL, Selig MS. An evaluation of an empirical model for stall delay due to rotation for HAWTs. *Technical Report*, National Renewable Energy Lab., Golden, CO (United States) 1997.

[58] Weekes SM, Tomlin AS. Evaluation of a semi-empirical model for predicting the wind energy resource relevant to small-scale wind turbines. *Renewable Energy* Feb 2013; **50**:280–288, doi:10.1016/j.renene.2012.06.053.

URL http://www.sciencedirect.com/science/article/pii/S0960148112004041.

[59] Lo JCF, Yang ZL, Pielke RA. Assessment of three dynamical climate downscaling methods using the Weather Research and Forecasting (WRF) model. *Journal of Geophysical Research: Atmospheres* May 2008; **113**(D9):D09 112, doi:10.1029/2007JD009216. URL http://onlinelibrary.wiley.com/doi/10.1029/2007JD009216/abstract.

[60] Bailey BH, Kunkel J. The financial implications of resource assessment uncertainty. *North American Wind Power*, vol. NAW1504, 2015.

[61] Environmental Protection Agency. *Great Lakes Basic Information*. 2012. URL www.epa.gov/greatlakes/basicinfo.html, accessed on 10/2014.

[62] Botts L, Krushelnicki B. *The Great Lakes. An Environmental Atlas and Resource Book.* United States Environmental Protection Agency & Environment Canada, 1987.

[63] Justus CG, Hargraves WR. Wind energy statistics for large arrays of wind turbines, Great Lakes and Pacific Coast regions. *Technical Report E-16-681* May 1977. Annual Progress Report, 1 May 1976 - 30 Apr. 1977, Georgia Inst. of Tech., Atlanta. School of Aerospace Engineering.

[64] Wang J, Bai X, Hu H, Clites A, Colton M, Lofgren B. Temporal and Spatial Variability of Great Lakes Ice Cover, 1973–2010*. *Journal of Climate* Sep 2011; **25**(4):1318–1329, doi:10.1175/2011JCLI4066.1. URL http://journals.ametsoc.org/doi/abs/10.1175/2011JCLI4066.1.

[65] Barthelmie RJ, Pryor SC. Can Satellite Sampling of Offshore Wind Speeds Realistically Represent Wind Speed Distributions? *Journal of Applied Meteorology* Jan 2003; **42**(1):83–94, doi:10.1175/1520-0450(2003)042<0083:CSSOOW>2.0.CO;2. URL http://journals.ametsoc.org/doi/full/10.1175/1520-0450(2003)042%3C0083:CSSOOW%3E2.0.CO%3B2.

[66] Paton DL, Bass A, Smith DG, Elliot DL, Barchet WR, George RL. Wind Energy Resource Atlas: Volume 3-The Great Lakes Region. *Technical Report PNL-3195, WERA-3*, Pacific Northwest Laboratory, Richland, Washington 1981.

[67] Saulesleja A. *Great Lakes climatological atlas*. Environment Canada, Atmospheric Environment Service: Ottawa, Canada, 1986.

[68] Environment Canada. *Canadian Wind Energy Atlas*. 2003. URL http://www.windatlas.ca/en/nav.php?field=EU&height=80&season=ANU&no=25.

[69] Li X, Zhong S, Bian X, Heilman WE. Climate and climate variability of the wind power resources in the Great Lakes region of the United States. *Journal of Geophysical Research: Atmospheres* 2010; **115**(D18):D18 107, doi:10.1029/2009JD013415. URL http://onlinelibrary.wiley.com/doi/10.1029/2009JD013415/abstract.

[70] Schwartz MN, Heimiller D, Haymes S, Musial W. Assessment of offshore wind energy resources for the United States. *Technical Report NREL/ TP - 500 - 45889*, National Renewable Energy Laboratory, Golden, Colorado 2010.

[71] Badger M, Badger J, Nielsen M, Hasager CB, Peña A. Wind Class Sampling of Satellite SAR Imagery for Offshore Wind Resource Mapping. *Journal of Applied Meteorology and Climatology* Aug 2010; **49**(12):2474–2491, doi:10.1175/2010JAMC2523.1. URL http://journals.ametsoc.org/doi/abs/10.1175/2010JAMC2523.1.

[72] Furevik BR, Sempreviva AM, Cavaleri L, Lefèvre JM, Transerici C. Eight years of wind measurements from scatterometer for wind resource mapping in the Mediterranean Sea. *Wind Energy* 2011; **14**(3):355–372, doi:10.1002/we.425. URL http://onlinelibrary.wiley.com/doi/10.1002/we.425/abstract.

[73] Karagali I, Badger M, Hahmann AN, Peña A, B Hasager C, Sempreviva AM. Spatial and temporal variability of winds in the Northern European Seas. *Renewable Energy* Sep 2013; **57**:200–210, doi:10.1016/j.renene.2013.01.017. URL http://www.sciencedirect.com/science/article/pii/S0960148113000426.

[74] Yang X, Li X, Pichel W, Li Z. Comparison of Ocean Surface Winds From ENVISAT ASAR, MetOp ASCAT Scatterometer, Buoy Measurements, and NOGAPS Model. *IEEE Transactions on Geoscience and Remote Sensing* Dec 2011; **49**(12):4743–4750, doi:10.1109/TGRS.2011.2159802.

[75] Pickett MH, Tang W, Rosenfeld LK, Wash CH. QuikSCAT Satellite Comparisons with Nearshore Buoy Wind Data off the U.S. West Coast. *Jour-*

nal of Atmospheric and Oceanic Technology Dec 2003; **20**(12):1869–1879, doi:10.1175/1520-0426(2003)020<1869:QSCWNB>2.0.CO;2. URL http://journals.ametsoc.org/doi/abs/10.1175/1520-0426(2003)020%3C1869:QSCWNB%3E2.0.CO%3B2.

[76] Zahumenský I. Guidelines on quality control procedures for data from automatic weather stations. World Meteorological Organization: Geneva, Switzerland, 2004. URL http://www.wmo.int/pages/prog/www/OSY/Meetings/ET-AWS3/Doc4%281%29.pdf.

[77] Nghiem S, Leshkevich G, Kwok R. Great Lakes Ice Cover Classification and Mapping Using Satellite Synthetic Aperture Radar (SAR) Data. San Diego, California, 1998. URL http://trs-new.jpl.nasa.gov/dspace/bitstream/2014/20334/1/98-1255.pdf, fifth International Conference on Remote Sensing for Marine and Coastal Environments.

[78] Pryor SC, Barthelmie RJ. 3.04 - Renewable Energy Resources – Ocean Energy: Wind–Wave–Tidal–Sea Currents. *Climate Vulnerability*, Pielke RA (ed.). Academic Press: Oxford, 2013; 65–81. URL http://www.sciencedirect.com/science/article/pii/B9780123847034003117.

[79] Mesinger F, DiMego G, Kalnay E, Mitchell K, Shafran PC, Ebisuzaki W, Jovic D, Woollen J, Rogers E, Berbery EH, *et al.*. North American Regional Reanalysis. *Bulletin of the American Meteorological Society* 2006; **87**(3):343–360.

[80] Carta JA, Velázquez S, Cabrera P. A review of measure-correlate-predict (MCP) methods used to estimate long-term wind characteristics at a target site. *Renewable and Sustainable Energy Reviews* Nov 2013; **27**:362–400, doi:10.1016/j.rser.2013.07.004. URL http://www.sciencedirect.com/science/article/pii/S1364032113004498.

[81] Oliver MA, Webster R. Kriging: a method of interpolation for geographical information systems. *International journal of geographical information systems* Jul 1990; **4**(3):313–332, doi:10.1080/02693799008941549. URL http://dx.doi.org/10.1080/02693799008941549.

[82] Hasager CB, Dellwik E, Nielsen M, Furevik BR. Validation of ERS-2 SAR offshore wind-speed maps in the North Sea. *International Journal of Remote Sensing* Oct 2004; **25**(19):3817–3841, doi:10.1080/01431160410001688286. URL http://dx.doi.org/10.1080/01431160410001688286.

[83] Pryor SC, Nielsen M, Barthelmie RJ, Mann J. Can satellite sampling of offshore wind speeds realistically represent wind speed distributions? Part II: Quantifying uncertainties associated with distribution fitting methods. *Journal of Applied Meteorology* May 2004; **43**(5):739–750, doi:10.1175/2096.1. WOS:000221825200008.

[84] Johannessen O, Bjorgo E. Wind energy mapping of coastal zones by synthetic aperture radar (SAR) for siting potential windmill locations 2000; **21**(9):1781–1786, doi:10.1080/014311600209733.

[85] Dagestad KF, Horstmann J, Mouche A, Perrie W, Shen H, Zhang B, Li X, Monaldo F, Pichel W, Lehner S, *et al.*. Wind retrieval from synthetic aperture radar - an overview. *Proceedings of SEASAR 2012*. ESA SP, European Space Agency, ESA, 2013.

[86] Hersbach H. Comparison of C-Band Scatterometer CMOD5.N Equivalent Neutral Winds with ECMWF. *Journal of Atmospheric and Oceanic Technology* Apr 2010; **27**(4):721–736, doi:10.1175/2009JTECHO698.1. URL `http://journals.ametsoc.org/doi/abs/10.1175/2009JTECHO698.1`.

[87] National Ice Center. *IMS Daily Northern Hemisphere Snow and Ice Analysis at 4 km and 24 km Resolution*. 2008. Boulder, Colorado USA: National Snow and Ice Data Center. http://dx.doi.org/10.7265/N52R3PMC.

[88] Beljaars ACM. The parametrization of surface fluxes in large-scale models under free convection. *Quarterly Journal of the Royal Meteorological Society* 1995; **121**(522):255–270, doi:10.1002/qj.49712152203. URL `http://onlinelibrary.wiley.com/doi/10.1002/qj.49712152203/abstract`.

[89] Ricciardulli L, Wentz F. Reprocessed QuikSCAT (V04) Wind Vectors with Ku-2011 Geophysical Model Function. *Technical Report 043011*, Remote Sensing Systems, Santa Rosa, California 2011. URL `http://images.remss.com/qscat/qscat_Ku2011_tech_report.pdf`.

[90] Tang W, Liu W, Stiles B. Evaluation of high-resolution ocean surface vector winds measured by QuikSCAT scatterometer in coastal regions. *IEEE Transactions on Geoscience and Remote Sensing* Aug 2004; **42**(8):1762–1769, doi:10.1109/TGRS.2004.831685.

[91] Nghiem SV, Leshkevich GA, Stiles BW. Wind Fields over the Great Lakes Measured by the SeaWinds Scatterometer on the QuikSCAT Satellite.

Journal of Great Lakes Research 2004; **30**(1):148–165, doi:10.1016/S0380-1330(04)70337-8. URL http://www.sciencedirect.com/science/article/pii/S0380133004703378.

[92] Karagali I, Peña A, Badger M, Hasager CB. Wind characteristics in the North and Baltic Seas from the QuikSCAT satellite. *Wind Energy* Jan 2014; **17**(1):123–140, doi:10.1002/we.1565. URL http://onlinelibrary.wiley.com/doi/10.1002/we.1565/abstract.

[93] Yang X, Li X, Zheng Q, Gu X, Pichel W, Li Z. Comparison of Ocean-Surface Winds Retrieved From QuikSCAT Scatterometer and Radarsat-1 SAR in Offshore Waters of the U.S. West Coast. *IEEE Geoscience and Remote Sensing Letters* Jan 2011; **8**(1):163–167, doi:10.1109/LGRS.2010.2053345.

[94] Monaldo F, Thompson D, Pichel W, Clemente-Colon P. A systematic comparison of QuikSCAT and SAR ocean surface wind speeds. *IEEE Transactions on Geoscience and Remote Sensing* Feb 2004; **42**(2):283–291, doi:10.1109/TGRS.2003.817213.

[95] Schoof JT, Pryor SC. Assessing the fidelity of AOGCM-simulated relationships between large-scale modes of climate variability and wind speeds. *Journal of Geophysical Research: Atmospheres* Aug 2014; **119**(16):2014JD021601, doi:10.1002/2014JD021601. URL http://onlinelibrary.wiley.com/doi/10.1002/2014JD021601/abstract.

[96] Barthelmie RJ, Hansen KS, Pryor SC. Meteorological Controls on Wind Turbine Wakes. *Proceedings of the IEEE* Apr 2013; **101**(4):1010–1019, doi:10.1109/JPROC.2012.2204029.

[97] Hansen KS, Barthelmie RJ, Jensen LE, Sommer A. The impact of turbulence intensity and atmospheric stability on power deficits due to wind turbine wakes at Horns Rev wind farm. *Wind Energy* Jan 2012; **15**(1):183–196, doi:10.1002/we.512. URL http://onlinelibrary.wiley.com.proxy.library.cornell.edu/doi/10.1002/we.512/abstract.

[98] Vanderwende BJ, Lundquist JK. The modification of wind turbine performance by statistically distinct atmospheric regimes. *Environmental Research Letters* 2012; **7**(3):034035, doi:10.1088/1748-9326/7/3/034035. URL http://stacks.iop.org/1748-9326/7/i=3/a=034035.

[99] Knudsen T, Bak T, Svenstrup M. Survey of wind farm control—power and fatigue optimization. *Wind Energy* Aug 2015; **18**(8):1333–1351, doi:10.

1002/we.1760. URL http://onlinelibrary.wiley.com/doi/10.1002/we.1760/abstract.

[100] Serrano González J, Burgos Payán M, Santos JMR, González-Longatt F. A review and recent developments in the optimal wind-turbine micro-siting problem. *Renewable and Sustainable Energy Reviews* Feb 2014; **30**:133–144, doi:10.1016/j.rser.2013.09.027. URL http://www.sciencedirect.com/science/article/pii/S1364032113006989.

[101] Chamorro LP, Porté-Agel F. Effects of Thermal Stability and Incoming Boundary-Layer Flow Characteristics on Wind-Turbine Wakes: A Wind-Tunnel Study. *Boundary-Layer Meteorology* Jun 2010; **136**(3):515–533, doi:10.1007/s10546-010-9512-1. URL http://link.springer.com/article/10.1007/s10546-010-9512-1.

[102] Churchfield MJ, Lee S, Michalakes J, Moriarty PJ. A numerical study of the effects of atmospheric and wake turbulence on wind turbine dynamics. *Journal of Turbulence* Jan 2012; **13**:N14, doi:10.1080/14685248.2012.668191. URL http://dx.doi.org/10.1080/14685248.2012.668191.

[103] Creech A, Früh WG, Maguire AE. Simulations of an Offshore Wind Farm Using Large-Eddy Simulation and a Torque-Controlled Actuator Disc Model. *Surveys in Geophysics* Feb 2015; **36**(3):427–481, doi:10.1007/s10712-015-9313-7. URL http://link.springer.com/article/10.1007/s10712-015-9313-7.

[104] Mo JO, Choudhry A, Arjomandi M, Lee YH. Large eddy simulation of the wind turbine wake characteristics in the numerical wind tunnel model. *Journal of Wind Engineering and Industrial Aerodynamics* Jan 2013; **112**:11–24, doi:10.1016/j.jweia.2012.09.002. URL http://www.sciencedirect.com/science/article/pii/S0167610512002462.

[105] Katic I, Højstrup J, Jensen N. A Simple Model for Cluster Efficiency. *EWEC'86. Proceedings*, vol. 1, Sesto E (ed.), Rome, Italy, 1987; 407–410.

[106] Jensen NO. A note on wind generator interaction. *Technical Report 2411*, Risø National Laboratory 1983.

[107] Ainslie J. Development of an eddy viscosity model for wind turbine wakes. *Proceedings of the BWEA Conference*, Oxford, England, 1985; 61–66.

[108] Larsen GC, Madsen HA, Thomsen K, Larsen TJ. Wake meandering: a pragmatic approach. *Wind Energy* Jul 2008; **11**(4):377–395, doi:10.1002/

we.267. URL http://onlinelibrary.wiley.com/doi/10.1002/we.267/full.

[109] Martinez L, Leonardi S, Churchfield M, Moriarty P. A Comparison of Actuator Disk and Actuator Line Wind Turbine Models and Best Practices for Their Use. *50th AIAA Aerospace Sciences Meeting including the New Horizons Forum and Aerospace Exposition*, American Institute of Aeronautics and Astronautics: Nashville, Tennessee, 2012; 1–13. URL http://arc.aiaa.org/doi/abs/10.2514/6.2012-900.

[110] Sarlak H, Meneveau C, Sørensen JN, Mikkelsen R. Quantifying the Impact of Subgrid Scale Models in Actuator-Line Based LES of Wind Turbine Wakes in Laminar and Turbulent Inflow. *Direct and Large-Eddy Simulation IX*, Fröhlich J, Kuerten H, Geurts BJ, Armenio V (eds.). No. 20 in ERCOFTAC Series, Springer International Publishing, 2015; 169–175.

[111] Larsen TJ, Madsen HA, Larsen GC, Hansen KS. Validation of the dynamic wake meander model for loads and power production in the Egmond aan Zee wind farm. *Wind Energy* May 2013; **16**(4):605–624, doi:10.1002/we.1563. URL http://onlinelibrary.wiley.com/doi/10.1002/we.1563/full.

[112] Churchfield MJ, Lee S, Moriarty PJ, Hao Y, Lackner MA, Barthelmie R, Lundquist JK, Oxley G. A Comparison of the Dynamic Wake Meandering Model, Large-Eddy Simulation, and Field Data at the Egmond aan Zee Offshore Wind Plant. *33rd Wind Energy Symposium*. AIAA: Kissimmee, Florida, 2014. URL http://arc.aiaa.org/doi/abs/10.2514/6.2015-0724.

[113] Iungo GV, Santoni-Ortiz C, Abkar M, Porté-Agel F, Rotea MA, Leonardi S. Data-driven Reduced Order Model for prediction of wind turbine wakes. *Journal of Physics: Conference Series* 2015; **625**(1):012 009:1–10, doi:10.1088/1742-6596/625/1/012009. URL http://stacks.iop.org/1742-6596/625/i=1/a=012009.

[114] Keck RE, de Maré M, Churchfield MJ, Lee S, Larsen G, Madsen HA. Two improvements to the dynamic wake meandering model: including the effects of atmospheric shear on wake turbulence and incorporating turbulence build-up in a row of wind turbines. *Wind Energy* Jan 2015; **18**(1):111–132, doi:10.1002/we.1686. URL http://onlinelibrary.wiley.com/doi/10.1002/we.1686/full.

[115] Jonkman JM, Buhl Jr ML. FAST User's Guide. *Technical Report NREL/EL-*

500-38230, National Renewable Energy Laboratory, Golden, Colorado Aug 2005. URL https://nwtc.nrel.gov/system/files/FAST.pdf.

[116] Sørensen JN, Shen WZ. Numerical Modeling of Wind Turbine Wakes. *Journal of Fluids Engineering* May 2002; **124**(2):393–399, doi:10.1115/1.1471361. URL http://dx.doi.org/10.1115/1.1471361.

[117] Meneveau C, Lund TS, Cabot WH. A Lagrangian dynamic subgrid-scale model of turbulence. *Journal of Fluid Mechanics* Jul 1996; **319**:353–385, doi:10.1017/S0022112096007379.

[118] Andersen SJ, Sørensen JN, Mikkelsen R. Simulation of the inherent turbulence and wake interaction inside an infinitely long row of wind turbines. *Journal of Turbulence* Apr 2013; **14**(4):1–24, doi:10.1080/14685248.2013.796085. URL http://dx.doi.org/10.1080/14685248.2013.796085.

[119] Aitken ML, Kosović B, Mirocha JD, Lundquist JK. Large eddy simulation of wind turbine wake dynamics in the stable boundary layer using the Weather Research and Forecasting Model. *Journal of Renewable and Sustainable Energy* May 2014; **6**(3):033 137:1–13, doi:10.1063/1.4885111. URL http://scitation.aip.org/content/aip/journal/jrse/6/3/10.1063/1.4885111.

[120] Keck RE, de Maré M, Churchfield MJ, Lee S, Larsen G, Aagaard Madsen H. On atmospheric stability in the dynamic wake meandering model. *Wind Energy* Nov 2014; **17**(11):1689–1710, doi:10.1002/we.1662. URL http://onlinelibrary.wiley.com/doi/10.1002/we.1662/abstract.

[121] Johansson PBV, George WK, Gourlay MJ. Equilibrium similarity, effects of initial conditions and local Reynolds number on the axisymmetric wake. *Physics of Fluids (1994-present)* Mar 2003; **15**(3):603–617, doi:10.1063/1.1536976. URL http://scitation.aip.org/content/aip/journal/pof2/15/3/10.1063/1.1536976.

[122] International Electrotechnical Comission. Wind Turbines - Part 1: Design Requirements. *Technical Report IEC 61400-1:2005(E)* 2005.

[123] Bossanyi EA. Wind Turbine Control for Load Reduction. *Wind Energy* Jul 2003; **6**(3):229–244, doi:10.1002/we.95.

[124] Ainslie JF. Calculating the flowfield in the wake of wind turbines. *Journal of Wind Engineering and Industrial Aerodynamics* Jan 1988; **27**(1–3):213–224, doi:10.1016/0167-6105(88)90037-2. URL http://www.sciencedirect.com/science/article/pii/0167610588900372.

[125] Trujillo JJ, Bingöl F, Larsen GC, Mann J, Kühn M. Light detection and ranging measurements of wake dynamics. Part II: two-dimensional scanning. *Wind Energy* Jan 2011; **14**(1):61–75, doi:10.1002/we.402. URL http://onlinelibrary.wiley.com/doi/10.1002/we.402/abstract.

[126] Fingersh LJ, Hand MM, Laxson AS. Wind turbine design cost and scaling model. *Technical Report*, National Renewable Energy Laboratory 2006.

[127] Käsler Y, Rahm S, Simmet R, Kühn M. Wake Measurements of a Multi-MW Wind Turbine with Coherent Long-Range Pulsed Doppler Wind Lidar. *Journal of Atmospheric and Oceanic Technology* Jun 2010; **27**(9):1529–1532, doi:10.1175/2010JTECHA1483.1. URL http://journals.ametsoc.org/doi/abs/10.1175/2010JTECHA1483.1.

[128] Frehlich R, Meillier Y, Jensen ML, Balsley B, Sharman R. Measurements of Boundary Layer Profiles in an Urban Environment. *Journal of Applied Meteorology and Climatology* Jun 2006; **45**(6):821–837, doi:10.1175/JAM2368.1. URL http://journals.ametsoc.org/doi/abs/10.1175/JAM2368.1.

[129] Iungo GV, Wu YT, Porté-Agel F. Field Measurements of Wind Turbine Wakes with Lidars. *Journal of Atmospheric and Oceanic Technology* Sep 2012; **30**(2):274–287, doi:10.1175/JTECH-D-12-00051.1. URL http://journals.ametsoc.org/doi/full/10.1175/JTECH-D-12-00051.1.

[130] Kumer VM, Reuder J, Svardal B, Sætre C, Eecen P. Characterisation of Single Wind Turbine Wakes with Static and Scanning WINTWEX-W LiDAR Data. *Energy Procedia* Jan 2015; **80**:245–254, doi:10.1016/j.egypro.2015.11.428. URL http://www.sciencedirect.com/science/article/pii/S1876610215021608.

[131] Barthelmie RJ, Crippa P, Wang H, Smith CM, Krishnamurthy R, Choukulkar A, Calhoun R, Valyou D, Marzocca P, Matthiesen D, *et al.*. 3d Wind and Turbulence Characteristics of the Atmospheric Boundary Layer. *Bulletin of the American Meteorological Society* Sep 2013; **95**(5):743–

756, doi:10.1175/BAMS-D-12-00111.1. URL http://journals.ametsoc.org/doi/full/10.1175/BAMS-D-12-00111.1.

[132] Smalikho IN, Banakh VA, Pichugina YL, Brewer WA, Banta RM, Lundquist JK, Kelley ND. Lidar Investigation of Atmosphere Effect on a Wind Turbine Wake. *Journal of Atmospheric and Oceanic Technology* Feb 2013; **30**(11):2554–2570, doi:10.1175/JTECH-D-12-00108.1. URL http://journals.ametsoc.org/doi/abs/10.1175/JTECH-D-12-00108.1.

[133] Haizmann F, Schlipf D, Raach S, Scholbrock A, Wright A, Slinger C, Medley J, Harris M, Bossanyi E, Cheng PW. Optimization of a feed-forward controller using a CW-lidar system on the CART3. *2015 American Control Conference (ACC)*, IEEE, 2015; 3715–3720.

[134] Mikkelsen T. Lidar-based Research and Innovation at DTU Wind Energy – a Review. *Journal of Physics: Conference Series* 2014; **524**(1):012 007, doi:10.1088/1742-6596/524/1/012007. URL http://stacks.iop.org/1742-6596/524/i=1/a=012007.

[135] Lange J, Mann J, Angelou N, Berg J, Sjöholm M, Mikkelsen T. Variations of the Wake Height over the Bolund Escarpment Measured by a Scanning Lidar. *Boundary-Layer Meteorology* Nov 2015; **159**(1):147–159, doi:10.1007/s10546-015-0107-8. URL http://link.springer.com/article/10.1007/s10546-015-0107-8.

[136] Hasager CB, Stein D, Courtney M, Peña A, Mikkelsen T, Stickland M, Oldroyd A. Hub Height Ocean Winds over the North Sea Observed by the NORSEWInD Lidar Array: Measuring Techniques, Quality Control and Data Management. *Remote Sensing* Sep 2013; **5**(9):4280–4303, doi:10.3390/rs5094280. URL http://www.mdpi.com/2072-4292/5/9/4280.

[137] Harris M, Pearson GN, Ridley KD, Karlsson CJ, Olsson FAA, Letalick D. Single-particle laser Doppler anemometry at 155 μm. *Applied Optics* Feb 2001; **40**(6):969, doi:10.1364/AO.40.000969. URL https://www.osapublishing.org/abstract.cfm?URI=ao-40-6-969.

[138] Harris M, Constant G, Ward C. Continuous-wave bistatic laser Doppler wind sensor. *Applied Optics* Mar 2001; **40**(9):1501, doi:10.1364/AO.40.001501. URL https://www.osapublishing.org/abstract.cfm?URI=ao-40-9-1501.

[139] Krishnamurthy R, Choukulkar A, Calhoun R, Fine J, Oliver A, Barr

K. Coherent Doppler lidar for wind farm characterization. *Wind Energy* Mar 2013; **16**(2):189–206, doi:10.1002/we.539. URL http://onlinelibrary.wiley.com/doi/10.1002/we.539/abstract.

[140] Wang H, Barthelmie RJ, Pryor SC, Brown G. Lidar arc scan uncertainty reduction through scanning geometry optimization. *Atmos. Meas. Tech.* Apr 2016; **9**(4):1653–1669, doi:10.5194/amt-9-1653-2016. URL http://www.atmos-meas-tech.net/9/1653/2016/.

[141] Frehlich R. Simulation of Coherent Doppler Lidar Performance in the Weak-Signal Regime. *Journal of Atmospheric and Oceanic Technology* Jun 1996; **13**(3):646–658, doi:10.1175/1520-0426(1996)013<0646:SOCDLP>2.0.CO;2. URL http://journals.ametsoc.org/doi/abs/10.1175/1520-0426(1996)013%3C0646:SOCDLP%3E2.0.CO;2.

[142] Mirocha JD, Rajewski DA, Marjanovic N, Lundquist JK, Kosović B, Draxl C, Churchfield MJ. Investigating wind turbine impacts on near-wake flow using profiling lidar data and large-eddy simulations with an actuator disk model. *Journal of Renewable and Sustainable Energy* Jul 2015; **7**(4):043 143, doi:10.1063/1.4928873. URL http://scitation.aip.org/content/aip/journal/jrse/7/4/10.1063/1.4928873.

[143] Smalikho I. Techniques of Wind Vector Estimation from Data Measured with a Scanning Coherent Doppler Lidar. *Journal of Atmospheric and Oceanic Technology* Feb 2003; **20**(2):276–291, doi:10.1175/1520-0426(2003)020<0276:TOWVEF>2.0.CO;2. URL http://journals.ametsoc.org/doi/abs/10.1175/1520-0426%282003%29020%3C0276%3ATOWVEF%3E2.0.CO%3B2.

[144] Peña A, Réthoré PE, Hasager CB, Hansen KS. Results of wake simulations at the Horns Rev I and Lillgrund wind farms using the modified Park model. *Technical Report*, DTU Wind Energy 2013.

[145] Peña A, Réthoré PE, van der Laan MP. On the application of the Jensen wake model using a turbulence-dependent wake decay coefficient: the Sexbierum case. *Wind Energy* Mar 2015; :n/a–n/adoi:10.1002/we.1863. URL http://onlinelibrary.wiley.com.proxy.library.cornell.edu/doi/10.1002/we.1863/abstract.

[146] Aitken ML, Banta RM, Pichugina YL, Lundquist JK. Quantifying Wind Turbine Wake Characteristics from Scanning Remote Sensor Data. *Journal of Atmospheric and Oceanic Technology* Jan 2014; **31**(4):765–787, doi:10.1175/

JTECH-D-13-00104.1. URL http://journals.ametsoc.org/doi/abs/10.1175/JTECH-D-13-00104.1.

[147] Barthelmie RJ, Doubrawa P, Wang H, Pryor SC. Defining wake characteristics from scanning and vertical full- scale lidar measurements. *The Science of Making Torque from Wind*, Munich, Germany, 2016.

[148] Lee S, Churchfield M, Sirnivas S, Moriarty P, Nielsen F, Skaare B, Byklum E. Coalescing Wind Turbine Wakes. *Journal of Physics: Conference Series*, vol. 625, IOP Publishing, 2015; 012 023.

[149] Pope SB. *Turbulent Flows*. Cambridge University Press, 2000.

[150] Schalkwijk J, Jonker HJJ, Siebesma AP, Bosveld FC. A Year-Long Large-Eddy Simulation of the Weather over Cabauw: An Overview. *Monthly Weather Review* Mar 2015; **143**(3):828–844. URL http://search.proquest.com.proxy.library.cornell.edu/docview/1661322380?pq-origsite=360link.

[151] Kunz R, Khatib IA, Moussiopoulos N. Coupling of mesoscale and microscale models - An approach to simulate scale interaction. *ResearchGate* Sep 2000; **15**(6-7):597–602, doi:10.1016/S1364-8152(00)00055-4. URL https://www.researchgate.net/publication/220274339_Coupling_of_mesoscale_and_microscale_models_-_An_approach_to_simulate_scale_interaction.

[152] Liu YS, Miao SG, Zhang CL, Cui GX, Zhang ZS. Study on microatmospheric environment by coupling large eddy simulation with mesoscale model. *Journal of Wind Engineering and Industrial Aerodynamics* Aug 2012; **107–108**:106–117, doi:10.1016/j.jweia.2012.03.033. URL http://www.sciencedirect.com/science/article/pii/S0167610512000906.

[153] Rodrigues CV, Palma JMLM. Estimation of turbulence intensity and shear factor for diurnal and nocturnal periods with an URANS flow solver coupled with WRF. *Journal of Physics: Conference Series* 2014; **524**(1):012 115, doi:10.1088/1742-6596/524/1/012115. URL http://stacks.iop.org/1742-6596/524/i=1/a=012115.

[154] Skamarock WC, Klemp JB, Dudhia J, Gill DO, Barker DM, Duda MG, Huang XY, Wang W, Powers JG. A Description of the Advanced Research WRF Version 3. *Technical Note TN-475+STR*, National Center for Atmospheric Research Jun 2008.

[155] Shin HH, Hong SY. Representation of the Subgrid-Scale Turbulent Transport in Convective Boundary Layers at Gray-Zone Resolutions. *Monthly Weather Review* Jan 2015; **143**(1):250–271, doi:10.1175/MWR-D-14-00116.1. URL http://journals.ametsoc.org/doi/abs/10.1175/MWR-D-14-00116.1.

[156] Ito J, Niino H, Nakanishi M, Moeng CH. An Extension of the Mellor–Yamada Model to the Terra Incognita Zone for Dry Convective Mixed Layers in the Free Convection Regime. *Boundary-Layer Meteorology* Jun 2015; **157**(1):23–43, doi:10.1007/s10546-015-0045-5. URL http://link.springer.com/article/10.1007/s10546-015-0045-5.

[157] Shin HH, Dudhia J. Evaluation of PBL Parameterizations in WRF at Sub-Kilometer Grid Spacings: Turbulence Statistics in the Dry Convective Boundary Layer. *Monthly Weather Review* 2016; doi:10.1175/MWR-D-15-0208.1. URL http://journals.ametsoc.org/doi/abs/10.1175/MWR-D-15-0208.1.

[158] Kitamura Y. Estimating Dependence of the Turbulent Length Scales on Model Resolution Based on A Priori Analysis. *Journal of the Atmospheric Sciences* Feb 2015; **72**(2):750–762. URL http://search.proquest.com.proxy.library.cornell.edu/docview/1652468742/abstract/68A63A47F9CF4677PQ/1.

[159] Honnert R, Masson V, Couvreux F. A Diagnostic for Evaluating the Representation of Turbulence in Atmospheric Models at the Kilometric Scale. *Journal of the Atmospheric Sciences* Jun 2011; **68**(12):3112–3131, doi:10.1175/JAS-D-11-061.1. URL http://journals.ametsoc.org/doi/full/10.1175/JAS-D-11-061.1.

[160] Boutle IA, Eyre JEJ, Lock AP. Seamless Stratocumulus Simulation across the Turbulent Gray Zone. *Monthly Weather Review* Apr 2014; **142**(4):1655–1668. URL http://search.proquest.com.proxy.library.cornell.edu/docview/1518520877.

[161] Frech M, Mahrt L. A two-scale mixing formulation for the atmospheric boundary layer. *Boundary-Layer Meteorology* Feb 1995; **73**(1-2):91–104, doi:10.1007/BF00708931. URL http://link.springer.com/article/10.1007/BF00708931.

[162] Hong SY, Noh Y, Dudhia J. A New Vertical Diffusion Package with an Explicit Treatment of Entrainment Processes. *Monthly Weather Re-*

view Sep 2006; **134**(9):2318–2341, doi:10.1175/MWR3199.1. URL http://journals.ametsoc.org/doi/abs/10.1175/MWR3199.1.

[163] Muñoz-Esparza D, Kosović B, García-Sánchez C, van Beeck J. Nesting turbulence in an offshore convective boundary layer using large-eddy simulations. *Boundary-layer meteorology* 2014; **151**(3):453–478.

[164] Muñoz-Esparza D, Kosović B, van Beeck J, Mirocha J. A stochastic perturbation method to generate inflow turbulence in large-eddy simulation models: Application to neutrally stratified atmospheric boundary layers. *Physics of Fluids* 2015; **27**(3):035 102.

[165] Montornès A, Casso P, Kosovic B, Lizcano G. Is WRF-LES a Suitable Tool for Realistic Turbulence Analyses in Wind Resource Assessment Applications? *22nd Symposium on Boundary Layers and Turbulence (AMS)*, 2016. URL https://ams.confex.com/ams/32AgF22BLT3BG/webprogram/Paper295742.html.

[166] Montornès A, Casso P, Kosovic B, Lizcano G. WRF-LES in the real world: Towards a seamless modeling chain for wind industry applications. *17th Annual WRF Users' Workshop*, 2016. URL http://www2.mmm.ucar.edu/wrf/users/workshops/WS2016/oral_presentations/3.3.pdf.

[167] Saha S, Moorthi S, Pan HL, Wu X, Wang J, Nadiga S, Tripp P, Kistler R, Woollen J, Behringer D, *et al.*. The NCEP climate forecast system reanalysis. *Bulletin of the American Meteorological Society* 2010; **91**(8):1015–1057.

[168] Jarvis A, Reuter HI, Nelson A, Guevara E, others. Hole-filled SRTM for the globe Version 4. *available from the CGIAR-CSI SRTM 90m Database (http://srtm. csi. cgiar. org)* 2008; .

[169] Bontemps S, Defourny P, Bogaert EV, Arino O, Kalogirou V, Perez JR. GLOBCOVER 2009-Products description and validation report 2011; .

[170] Cebeci T. *Analysis of turbulent boundary layers*, vol. 15. Elsevier, 2012.

[171] Sørensen LL, Larsen SE. Atmosphere–Surface Fluxes of CO2 using Spectral Techniques. *Boundary-Layer Meteorology* Jul 2010; **136**(1):59–81, doi:10.1007/s10546-010-9499-7. URL https://link.springer.com/article/10.1007/s10546-010-9499-7.

[172] Han Y, Stoellinger M, Naughton J. Large eddy simulation for atmospheric boundary layer flow over flat and complex terrains. *Journal of Physics: Conference Series* 2016; **753**(3):032 044, doi:10.1088/1742-6596/753/3/032044. URL http://stacks.iop.org/1742-6596/753/i=3/a=032044.

[173] Keith DW, DeCarolis JF, Denkenberger DC, Lenschow DH, Malyshev SL, Pacala S, Rasch PJ. The influence of large-scale wind power on global climate. *Proceedings of the National Academy of Sciences of the United States of America* Nov 2004; **101**(46):16 115–16 120, doi:10.1073/pnas.0406930101. URL http://www.pnas.org/content/101/46/16115.

[174] Chatterjee F, Allaerts D, Blahak U, Meyers J, van Lipzig N. Evaluation of a wind-farm parametrization in a regional climate model using large eddy simulations. *Quarterly Journal of the Royal Meteorological Society* Oct 2016; **142**(701):3152–3161, doi:10.1002/qj.2896. URL http://onlinelibrary.wiley.com.proxy.library.cornell.edu/doi/10.1002/qj.2896/abstract.

[175] Fitch AC, Olson JB, Lundquist JK, Dudhia J, Gupta AK, Michalakes J, Barstad I. Local and Mesoscale Impacts of Wind Farms as Parameterized in a Mesoscale NWP Model. *Monthly Weather Review* Mar 2012; **140**(9):3017–3038, doi:10.1175/MWR-D-11-00352.1. URL http://journals.ametsoc.org/doi/abs/10.1175/MWR-D-11-00352.1.

[176] Volker PJH, Badger J, Hahmann AN, Ott S. The Explicit Wake Parametrisation V1.0: a wind farm parametrisation in the mesoscale model WRF. *Geosci. Model Dev.* Nov 2015; **8**(11):3715–3731, doi:10.5194/gmd-8-3715-2015. URL http://www.geosci-model-dev.net/8/3715/2015/.

[177] Fitch AC. Notes on using the mesoscale wind farm parameterization of Fitch et al. (2012) in WRF. *Wind Energy* Sep 2016; **19**(9):1757–1758, doi:10.1002/we.1945. URL http://onlinelibrary.wiley.com/doi/10.1002/we.1945/abstract.

[178] Barthelmie RJ, Larsen GC, Frandsen ST, Folkerts L, Rados K, Pryor SC, Lange B, Schepers G. Comparison of Wake Model Simulations with Offshore Wind Turbine Wake Profiles Measured by Sodar. *Journal of Atmospheric and Oceanic Technology* Jul 2006; **23**(7):888–901, doi:10.1175/JTECH1886.1. URL http://journals.ametsoc.org/doi/abs/10.1175/JTECH1886.1.

[179] Peña A, Réthoré PE, Rathmann O. Modeling large offshore wind farms

under different atmospheric stability regimes with the Park wake model. *Renewable Energy* Oct 2014; **70**:164–171, doi:10.1016/j.renene.2014.02.019. URL http://www.sciencedirect.com/science/article/pii/S0960148114001001.

[180] Nathan J, Bautista M, Masson C, Dufresne L. Study of the near wake of a wind turbine in ABL flow using the actuator line method. *Journal of Physics: Conference Series*, vol. 524, IOP Publishing, 2014; 012 141.

[181] Benson J. Boundary-layer response to a change in surface roughness. PhD Thesis, The University of Reading 2005.

[182] Hedegaard K, Larsen SE. *Wind Speed and Direction Changes Due to Terrain Effects Revealed by Climatological Data from Two Sites in Jutland*, vol. 434. Risø, 1983.

[183] Barthelmie RJ, Jensen LE. Evaluation of wind farm efficiency and wind turbine wakes at the Nysted offshore wind farm. *Wind Energy* Sep 2010; **13**(6):573–586, doi:10.1002/we.408. URL http://onlinelibrary.wiley.com/doi/10.1002/we.408/abstract.